ALL-DIAMOND NEURAL PROBES FOR ELECTRICAL RECORDING AND ELECTROCHEMICAL DETECTION

By

Michael William Varney

A DISSERTATION

Submitted to
Michigan State University
in partial fulfillment of the requirements
for the degree of

Electrical Engineering – Doctor of Philosophy

2014

ABSTRACT

ALL-DIAMOND NEURAL PROBES FOR ELECTRICAL RECORDING AND ELECTROCHEMICAL DETECTION

By

Michael William Varney

Scientists have long been trying to understand the workings of the brain by measuring electrical neural activity. The invention of the micro-electrode array (MEA), or neural probe, was a great step improving neuroscientists' capabilities of recording neural activity. Neural probes allow for repeatable and customizable sizing and spacing of electrodes that is out of reach of wire electrodes. This, combined with improvements in recording hardware, on-probe electronics, and action potential detection algorithms, has brought great advancements in the fields of neuroscience and brain-machine interfaces.

The original neural probes were fabricated using silicon, due to the technology available at the inception of neural probes. However, many researchers have fabricated neural probes out of various combinations of materials. The most popular materials seem to be silicon-based materials and polymers such as polyimide, SU-8, and Parylene C. One material of particular interest, due to its combination of advantageous chemical and mechanical properties, is polycrystalline diamond. Diamond is a good material for neural probes because it has a high Young's modulus (~10^{11} Pa), it has good biocompatibility, it is resistant to fouling, and it is chemically inert. The main obstacle to developing diamond-based neural probes is that diamond's beneficial properties also make it difficult to micromachine, making it difficult to develop processes for probe fabrication.

One major problem with diamond probe fabrication is that diamond is incompatible with many materials, due to the high temperatures involved in depositing diamond. However, because diamond has a large band gap (~5.5 eV), it is a good candidate for single material MEMS (SMM). SMM devices use only one material for their structural material, insulators, semiconductors, and conductors. This is accomplished by selectively doping the material (diamond) to create different electrical properties for different parts of the structure. By using the SMM process to fabricate neural probes, many of the problems with incompatible materials are resolved. However, SMM fabrication has its own set of issues associated with it.

The goal of this work is to develop a process to fabricate single-material diamond neural probes, fabricate the neural probes, and test the neural probes. A process for fabrication of single-material diamond has been presented and details on the fabrication of the probes has been provided. Furthermore, these single-material diamond neural probes have been used for *in-vivo* electrical neural recordings and *in-vitro* electrochemical detection. The electrical recordings were also analyzed using a continuous wavelet transform method in order to improve action potential detection. A comparison is also made between silicon-based neural probes, diamond-based neural probes, and single-material-diamond neural probes.

This work marks the first time that SMM neural probes have been fabricated and tested, the first time that a functional SMM device was tested, and the first time that a SMM device was used *in vivo*.

ACKNOWLEDGMENTS

I would like to thank my entire family for their patience, understanding, and support during this research. Additional thanks to all of my friends for their years of support.

I would like to thank my advisor, Dr. Dean M. Aslam, for his guidance, encouragement, and support through this research. I would also like to thank my guidance committee Dr. Tim Hogan, Dr. Wen Li, and Dr. Donna H. Wang for their advice and support. Thank you to Dr. Norbert Mueller for his financial support through some of this research. Additional thanks to all of the staff in the ECE department – I could not have done this research without you.

I would like to thank the members of my research group, especially Dr. Hoyin Chan, Dr. Zongliang Cao, Dr. Abed Janoudi, and Sean Hatch, for their assistance and productive discussions.

This work was supported in part by the Engineering Research Centers Program of the National Science Foundation under Award Number EEC-9986866.

TABLE OF CONTENTS

LIST OF TABLES

LIST OF FIGURES

CHAPTER 1:

Research Motivation and Goals

1.1 Introduction

Neural probes have been of great interest over the past decade due to their overwhelming potential for use in neuroprosthesis [1,2], the treatment of neurological disorders [3], or further unraveling the mysteries of the brain. Over the past half-century, neural probes have evolved from individual insulated wires to precision-micromachined, three-dimensional arrays of electrodes (for a review of early neural micro-electrode arrays [MEAs], see Kovacs et al. [4]). Modern neural probes are fabricated from a variety of materials, the most popular being silicon and polymers such as polyimide, SU-8**,** and Parylene C.

Many research groups are developing unique processes for creating neural probes [4-16]. However, silicon can be an undesirable probe material as, without modification, it has been found to have poor flexibility, solubility in water, and can induce undesirable glial responses [17]. Many groups have solved this problem through coating silicon with biocompatible materials. As an alternative to coating silicon, undoped diamond has been explored as a substrate material due to its structural properties and high biocompatibility [18].

Probes often have different materials serving as electrodes. All neural probes use an inert, metallic (or metalized) substance as their electrodes. Common electrode materials for electrical sensing applications include gold, platinum and iridium. Iridium-oxide electrodes and boron-doped poly-C electrodes have both been shown to be useful for the detection of neurotransmitters [19,20]. However, iridium-oxide electrodes are used as quasi-reference electrodes, whereas boron-doped-diamond electrodes are used as working electrodes. Boron-doped poly-C electrodes could potentially be used for both electrochemical detection and for recording electrical signals. Chan et al. [21,22] developed a process for fabricating neural probes using undoped poly-C as the structural material and boron-doped poly-C as the electrode material. Non-diamond materials are used for interconnects and electrical-insulation layers. This probe has been used to measure electrical neural activity, as well as to electrochemically detect neurotransmitters in vitro.

This work is focused on the development of a neural probe process using a single material MEMS (SMM) concept [23-25]. SMM is a subset of MEMS technologies where MEMS devices are fabricated from a sole semiconductor with selective doping to achieve the electrical behavior desired. A microsystem merely has to contain single-material subsystems or devices to be considered an SMM device. Advantages associated with SMM design include simplified mechanical design, reduced mask count, and reduced equipment requirements.

Through SMM, the fabrication cost can be reduced by using as few masks and materials as possible. Poly-C is good candidate for SMM because of its unique combination of physical properties and the feasibility of selectively growing poly-C to be a semiconductor or insulator.

The SMM concept can be applied to neural probe fabrication. Neural probes can be fabricated using as few as three or four masks and one material. In SMM diamond neural probe, undoped diamond (10^7 ohm-cm) serves not only as a structural layer, but also as the insulating layer. Highly boron-doped diamond (10^{-3} ohm-cm) is utilized for interconnects and electrodes.

1.2 Objectives of this Work

In this work, there are 3 main objectives which all represent seminal work. These objectives can be further broken down into 11 tasks, as seen in Fig. 1-1. The objectives of the work are as follows:

1. Development and fabrication of SMM diamond neural probes – Developing a process and relevant techniques in order to produce SMM neural probes. Furthermore, fabricating SMM neural probes which are the first of their kind, and the first SMM BioMEMS device. This objective can be divided into 3 tasks:
    a. Fundamentals of diamond micromachining
    b. Diamond probe fabrication
    c. SMM diamond probe fabrication – seminal
2. Demonstration of functional SMM diamond neural probes – Using SMM diamond probes for both *in-vitro* electrochemical detection and *in-vivo* neural recording applications. This is the first time that SMM diamond probes have been tested and the first SMM device to ever be used *in vivo*. This is divided into 2 tasks:
    a. In-vitro electrochemical detection experiment using SMM diamond neural probes – seminal
    b. In-vivo neural recording experiments using SMM diamond neural probes – seminal
3. Determining viability of SMM diamond neural probes – Determining whether the SMM diamond probes can be used in neural recording experiments. Comparing the performance of the SMM diamond probes to other probe types. This objective can be broken down into 5 tasks:

a. Analysis of neural recordings using basic thresholding technique (window discriminator) for silicon, diamond, and SMM diamond neural probes - seminal

b. Study of action potential detection methods for low SNR applications

c. Analysis of neural recordings using the continuous wavelet transform method for silicon, diamond, and SMM diamond neural probes – seminal

d. Comparison between results using basic thresholding technique and advanced continuous wavelet transform technique for silicon, diamond and SMM diamond neural probes – seminal

e. Performance comparison between silicon probes, diamond probes, and SMM diamond probes – seminal

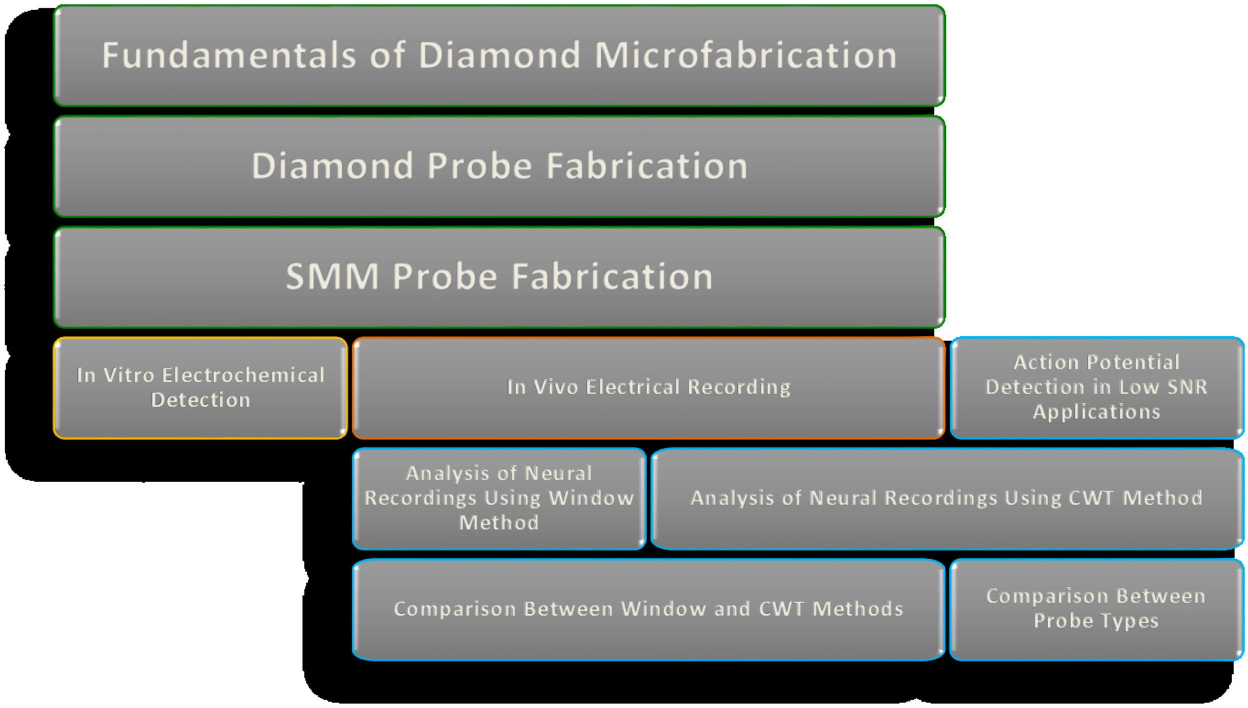

Figure 1-1: List of tasks completed in this work.

1.3 Dissertation Outline

This dissertation is divided into 9 Chapters. This first chapter serves to introduce the work presented, enumerate the objectives of the work, and outline the remainder of the dissertation. The second chapter details the fundamentals of diamond microfabrication including diamond deposition, creating highly insulating undoped diamond, and patterning of diamond films. The third chapter explains and chronicles the development and fabrication of diamond-based neural probes and SMM diamond neural probes. The fourth chapter describes electrochemical testing performed using the SMM diamond neural probe. Chapter 5 describes neural recording experiments performed using the SMM diamond neural probes and their preliminary results using a basic thresholding technique. Chapter 6 explores advanced action potential techniques using the discrete wavelet transform (DWT), the continuous wavelet transform (CWT), and the Teager energy operator (TEO). The performance of each of these methods is compared for low SNR applications. The seventh chapter applies the CWT method to the results from Chapter 5. The results are then used to compare the CWT method to the basic thresholding method in Chapter 5 and to compare the performance between probe types. Chapter 8 summarizes the contributions of this work and proposes future research areas. The final chapter discusses K-12 outreach work that was performed in tandem with the rest of the work described in this dissertation.

REFERENCES

REFERENCES

[1] X. Navarro, T.B. Krueger, N. Lago, S. Micera, T. Stieglitz and P. Dario, “A critical review of interfaces with the peripheral nervous system for the control of neuroprostheses and hybrid bionic systems,” *Journal of the Peripheral Nervous System*, vol. *10*, pp. 229-258, 2005.

[2] M.A. Lebedev and M.A.L. Nicolelis, “Brain-machine interfaces: past, present and future,” *Trends in Neurosciences* 2006, *29*, 536-546.

[3] E. Moro and E.A. Lang, “Criteria for deep-brain stimulation in Parkinson's disease: review and analysis,” *Expert Review of Neurotherapeutics*, vol. *6*, pp. 1695-1705, 2006.

[4] D.T. Kewley, M.D. Hills, D.A. Borkholder, I.E. Opris, N.I. Maluf, C.W. Storment and G.T.A. Kovacs, “Plasma-etched neural probes,” *Sens. Actuators A*, vol. *58*, pp. 27-35, 1997.

[5] S. Takeuchi, T. Suzuki, K. Mabuchi and H. Fujita, “3D flexible multichannel neural probe array,” *J. of Micromech. and Microeng*., vol. *14*, pp. 104-107, 2004.

[6] D.R. Kipke, “Implantable neural probe systems for cortical neuroprosthesis,” *Proceedings of the Int. Conf. of the IEEE Eng. in Med. and Bio. Soc*., pp. 5344-5347, 2004.

[7] Q. Bai and K.D. Wise, “Single-unit neural recording with active microelectrode arrays,” *IEEE Trans. Biomed. Eng*., vol. *48*, pp. 911-920, 2001.

[8] P. Norlin, M. Kindlundh, A. Mouroux, K. Yoshida and U.G. Hofmann, “A 32-site neural recording probe fabricated by DRIE of SOI substrates,” *J. of Micromech. and Microeng*., vol. *12*, pp. 414-419, 2002.

[9] P.K. Campbell, K.E. Jones, R.J. Huber, K.W. Horch and R.A. Normann, “A silicon-based three-dimensional neural interface: manufacturing process for an intracortical electrode array,” *IEEE Trans. Biomed. Eng.*, vol. *38*, pp. 758-768, 1991.

[10] M.K. Kindlundh, P. Norlin and U.G. Hofmann, “A neural probe process enabling variable electrode configurations,” *Sensors and Actuators B: Chemical*, vol. *12*, pp. 51-58, 2004.

[11] T.H. Yoon, E.J. Hwang, D.Y. Shin, S.J. Parl, S.J. Oh, S.C. Jung, H.C. Shin and S.J. Kim, "A micro-machined silicon depth probe for multichannel neural recording," *IEEE Trans. Biomed. Eng.*, vol. *47*, pp. 1082-1087, 2000.

[12] W.L.C. Rutten, H.J. VanWier and J.H.M. Put, "Sensitivity and selectivity of intraneural stimulation using a silicon electrode array," *IEEE Trans. Biomed. Eng*., vol. *38*, pp. 192-198, 1991.

[13] K. Chueng, L. Gun, K. Djupsund, D. Yang and L.P. Lee, "A new neural probe using SOI wafers with topological interlocking mechanism," *Proceedings of IEEE Int. Conf. on Microtechnologies in Medicine and Biology*, pp. 507-511, 2000.

[14] P.S. Motta and J.W. Judy, "Multielectrode microprobes for deep-brain stimulation fabricated with a customizable 3-D electroplating process," *IEEE Trans. on Biomed. Eng*., vol. *52*, pp. 923-933, 2005.

[15] J. Wu, L. Yan, W.C. Tang and F.G. Zeng, "Micromachined electrode arrays with form-fitting profile for auditory nerve prostheses," *Proc. of IEEE Eng. in Medicine and Biology*, vol. *5*, pp. 5260-5263, 2005.

[16] K.D. Wise, A.M. Sodagar, Y. Yao, M.N. Gulari, G.E. Perlin and K. Najafi, "Microelectrode, micro-electronics, and implantable neural Microsystems," *Proc. of the IEEE*, vol. *96*, pp. 1184-1202, 2008.

[17] D.H. Szarowski, M.D. Andersen, S. Retterer, A.J. Spence, M. Isaacson, H.G. Craighead, J.N. Turner and W. Shain, "Brain responses to micromachined silicon devices," *Brain Research*, vol. *983*, pp. 23-35, 2003.

[18] L. Tang, C. Tsai, W.W. Gerberich, L. Kruckebeu and D.R. Kania, "Biocompatibility of chemical-vapour-deposited diamond," *Biomaterials*, vol. *16*, pp. 483-488, 1995.

[19] R.K. Franklin, M.D. Johnson, K.A. Scott, J.H. Shim, H. Nam, D.R. Kipke and R.B. Brown, "Iridium oxide reference electrodes for neurochemical sensing with MEMS microelectrode arrays," *IEEE Sensors*, pp. 1400-1403, 2005.

[20] G.M. Swain and R. Ramesham, "The electrochemical activity of boron-doped polycrystalline diamond thin film electrode," *Anal. Chem*., vol. *65*, pp. 345-351, 1993.

[21] H.-Y. Chan, M. Varney, D.M. Aslam K.D. and Wise, "Fabrication and characterization of all-diamond microprobes for electrochemical analysis," *Proceedings of IEEE Int. Conf. on Nano/Micro Engineered and Molecular Syst.*, pp. 532-535, 2008.

[22] H.-Y. Chan, D.M. Aslam, S.H. Wang, G.M. Swain and K.D. Wise, “Fabrication and testing of a novel all-diamond neural probe for chemical detection and electrical sensing applications,” In *Proceedings of IEEE Int. Conf. on Micro Electro Mechanical Systems*, pp. 244-247, 2008.

[23] Z. Cao and D.M. Aslam, “MEMS structures using polycrystalline diamond single-material micro technologies,” *Presented at the IEEE Nano Electro Mechanical Systems*, Xiamen, China, 2010.

[24] Z. Cao, M.W. Varney and D.M. Aslam, “Single-material MEMS using polycrystalline diamond,” *Tech. Digest MEMS*, pp. 51-54, 2010.

[25] M.W. Varney, Z. Cao and D.M. Aslam, “Fabrication and testing of a novel all-diamond neural probe for chemical detection and electrical sensing applications,” *Presented at the IEEE Nano Electro Mechanical Systems*, Xiamen, China, 2010.

CHAPTER 2:

Diamond Microfabrication Technologies

2.1 Introduction

In order to create useful MEMS devices using polycrystalline diamond (poly-C), fundamental techniques of preparing, growing, and etching poly-C must be learned or developed. The same can be said of any materials to be processed, however diamond has some peculiarities that make these fundamentals more critical than some other materials. For example, diamond growth typically takes place in a high temperature environment, making many materials and processes incompatible. Also diamond is nearly impossible to etch chemically requiring aggressive patterning techniques for even simple patterning. Once the diamond microfabrication fundamentals are understood, neural probe fabrication (as well as other diamond MEMS device fabrication) becomes possible. This Chapter will cover the growth of diamond films, resolving aberrant conductivity of undoped diamond films, and the patterning of diamond films.

2.2 Diamond Deposition

Deposition of diamond on non-diamond surfaces requires a seeding step before diamond growth. This step spreads small diamond particles over the surface to give the diamond film places to begin to grow from. Typical seeding methods are spraying or spinning diamond-loaded fluids [1,2] or diamond-loaded water [3], spinning of diamond-loaded photoresist [4], surface abrasion [5-7] followed by sonication of diamond-loaded solution [8], or bias-enhanced nucleation [9-11]. In this study, diamond probes are fabricated on top of SiO_2, so nucleation with diamond-loaded water is ideal as it is selective to hydrophilic surfaces. The diamond-loaded water used was purchased from Advanced Abrasives Corporation with an average particle size of 1 μm. The solution was diluted so that the diamond content was 5% of the volume. Before seeding, the Si/SiO_2 substrate is exposed to an oxygen plasma in a plasma asher at a power of 250 W and a pressure of 500 mTorr to remove any organic residue. (Alternatively a brief etch in 9:1 H_20:HF has also been used.) The diamond solution was also prepared using an ultrasonic bath to agitate the solution for 30 minutes to ensure an even distribution of diamond particles. Once the solution and substrate are prepared, diamond solution was pipetted onto the substrate until about 70% of the substrate was covered. At this point, the wafer was spun at 4000 RPM for 45 seconds to evenly distribute diamond particles over the substrate. The resulting seeding density was approximately 10^{11} nuclei/cm^2.

Diamond growth was achieved using microwave plasma-assisted chemical vapor deposition (MPCVD). The system used was a Wavemat MPDR 313EHP with a 2.45 GHz, 5 kW Sairem GMP60KSM microwave power supply. The system chamber measured 9” in diameter with a quartz bell jar of 5” in diameter. Growth was done in a hydrogen-rich plasma with methane used as a carbon source. Before the growth process, the MPCVD chamber was pumped to a vacuum of less than 20 mTorr absolute pressure. Once the chamber had been evacuated, gas flow was initiated and the pressure in the chamber was maintained at 40 Torr absolute. The main constituent of the growth plasma was H_2, as such H_2 had the highest flow rate of 100 sccm. Once the pressure had stabilized, the MPCVD was started and the output power was slowly increased to 2.3 kW as the temperature increased to about 700 °C. The source of carbon for diamond growth is CH_4 which is next added at a rate of 1.5 sccm. The peak substrate temperature reached during growth was ~750 °C. A summary of growth conditions can be seen in Table 2-1.

Table 2-1: Growth parameters for boron-doped-diamond films.

Parameters	Values	
Microwave Power	2.3 kW, 2.45 GHz	
Deposition Pressure	40 Torr	
Target Substrate Temperature	750 °C	
Gases Used for Growth	Hydrogen [H_2]	100 sccm
	Methane [CH_4]	1.5 sccm
	TMB [0.098% $B(CH_3)_3$:H_2]	10 sccm
Growth Rate	0.10 – 0.15 μm/h	

Typical diamond growth was performed using H_2 and CH_4 at a flow rate of 100 sccm and 1.5 sccm, respectively. Trimethylboron (TMB) [$B(CH_3)_3$] can also be included in the growth environment in order to dope the diamond. The range of sheet resistivity of diamond is between 10^{-3} to 10^{2} Ω-cm depending on the amount of TMB present during growth. Fig. 2-1 shows an example SEM of diamond grown using this method. The quality of the diamond was verified using Raman spectroscopy. Fig. 2-2 shows an example Raman spectrograph of samples of diamond grown.

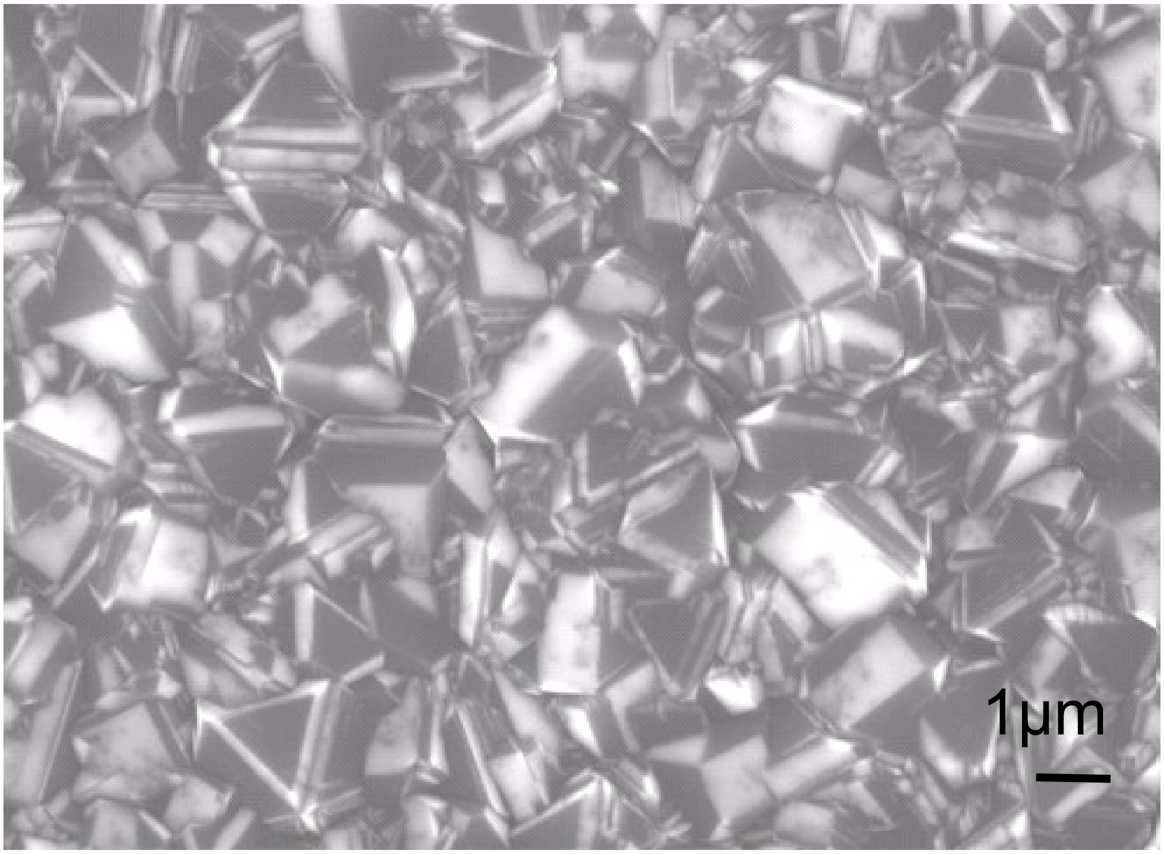

Figure 2-1: SEM of diamond grown by MPCVD.

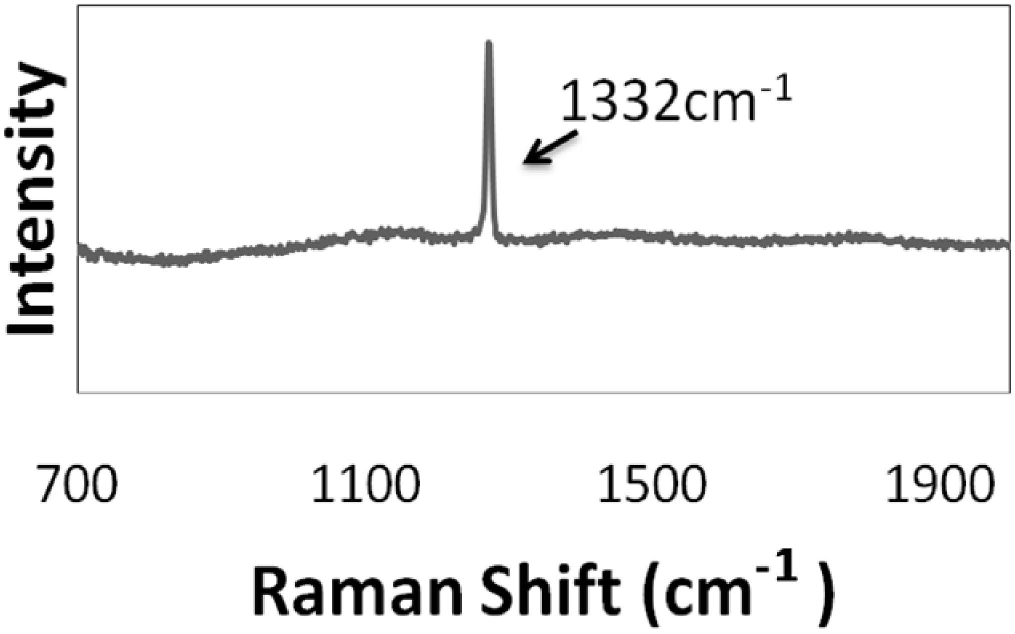

Figure 2-2: Raman spectrograph of diamond grown by MPCVD.

2.3 Conductivity of Undoped Diamond

In order to use diamond for single-material MEMS, it is important to be able to produce diamond films with high electrical resistivity. In theory, undoped diamond should have a band gap of ~5.5 eV and the resistivity of natural diamond has been shown to be $\sim 10^{14} - 10^{16}$ Ω-cm [12-14]. However, undoped diamond films grown in a 100:1.5 H_2:CH_4 environment, as described in section 2.2, were found to have a resistivity on the order of 10^{3} - 10^{5} Ω-cm. The mechanism causing conduction in as-grown diamond films has been frequently investigated [15-28]. Probable conduction mechanisms suggested include conduction along the grain boundaries [20,21,25], conduction due to impurities (B, N, or Si) [19,26], and conduction due to hydrogen traps [28]. Additionally, the surface of as-grown diamond films is typically conductive due to the presence of non-diamond carbon. However, this surface layer conductivity is easily mitigated by briefly etching the diamond film or through annealing. There is no consensus on what the primary mechanism of bulk conduction is in as-grown diamond films. However, the main contributor in the undoped diamond films in this study is likely unintended boron doping, as the same growth system is used for highly-doped, lightly-doped, and undoped diamond films.

In order to prevent boron incorporation in undoped diamond films, O_2 was experimentally added to the growth environment. It is known that O_2 in the growth environment can increase the resistivity of as-grown diamond films. However, O_2 in the growth environment is also a very effective etchant of diamond. In order to determine what amounts of O_2 were appropriate so that the growth rate of diamond films would not be significantly impacted by the addition of diamond, a study was conducted where the amount of O_2 in the growth environment was varied and the growth rate of diamond films was measured. In this study, diamond films were grown with growth gases of H_2:CH_4 with flow rates of 100:2 sccm. The growth rates for various flowrates of O_2 can be seen in Fig. 2-3. It can be seen in Fig. 2-3 that there is a significant decrease in diamond growth rate if more than 0.5 sccm of O_2 is added to the growth gases. For the remainder of this work, a ratio of 4:1 CH_4:O_2 was used in the growth of undoped diamond. Typical growth conditions for undoped diamond films can be seen in Table 2-2. The addition of O_2 to the growth environment increased the resistivity of undoped diamond films by approximately 6 orders of magnitude, from ~10^3 Ω-cm to >10^9 Ω-cm. Presumably the oxygen accounts for this increase in resistivity because the oxygen prevents unwanted boron from depositing in the diamond lattice. Oxygen may also reduce the number of sp^2 carbon bonds present in the finished diamond.

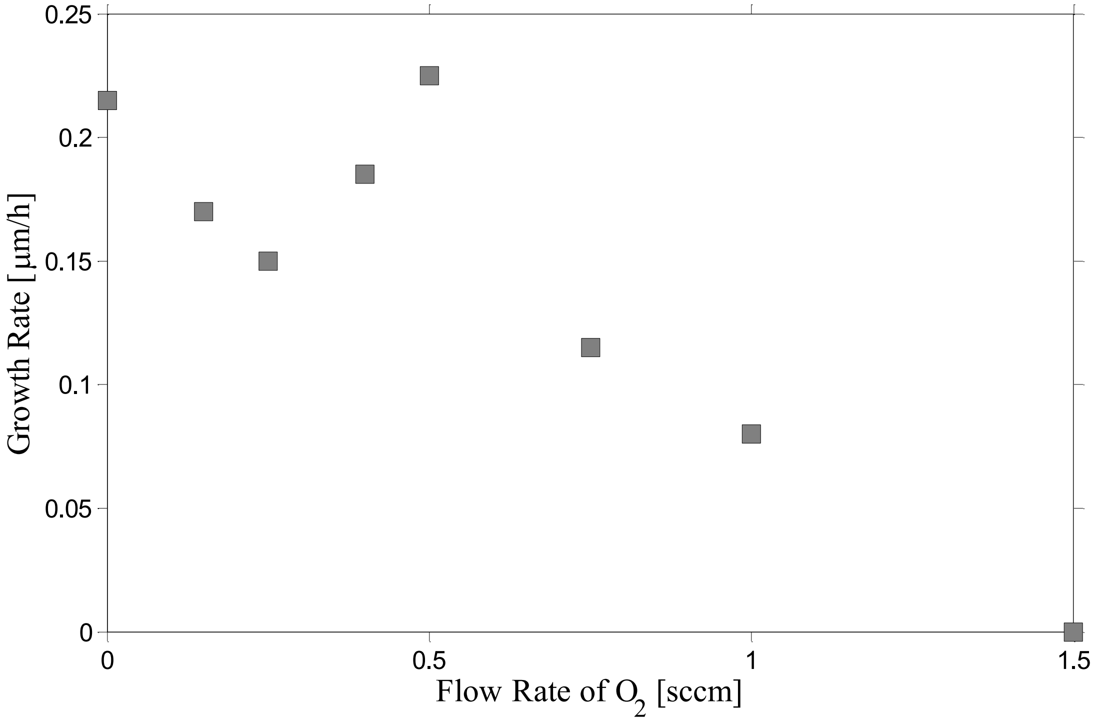

Figure 2-3: Graph of diamond film growth rate versus additional O_2 flow in diamond growth environment.

Table 2-2: Growth parameters for undoped-diamond films.

Parameters	**Values**	
Microwave Power	2.3 kW, 2.45 GHz	
Deposition Pressure	40 Torr	
Target Substrate Temperature	750 °C	
Gases Used for Growth	Hydrogen [H_2]	100 sccm
	Methane [CH_4]	1.5 sccm
	Oxygen [O_2]	0.38 sccm
Growth Rate	~0.10 μm/h	

2.4 Patterning Diamond Films

Conventional diamond patterning is done using dry etching tools, as wet etching of diamond is impractical. One of the common methods of etching is reactive ion etching (RIE) [29-53]. RIE has been thoroughly investigated for patterning diamond films. Typical gases used to etch are O_2 and CF_4. Pure O_2 etching can be problematic due to columnar structures being formed [34-36, 45, 47-53]. These structures have been attributed to differences in chemical composition of diamond grains and grain boundaries, intrinsic crystal defects, and unintentionally sputtered micro-masks. Adding CF_4 to the O_2 etch recipe will increase the etch rate and avoid the formation of the diamond columns [30] [40]. However, the presence of fluorine in the plasma can damage the underlying layers once the diamond is partially or entirely etched. In some processes, when the underlying layers must be preserved, a multi-step etching process can be adopted [50-53]. In a multi-step process, the increased etch rate of CF_4 can be taken advantage of at the beginning of the etch process. When the etching approaches the underlying layers, less-destructive plasma can be used to finish the etching, such as O_2 or H_2 plasma.

For the purpose of this study, the layers beneath the diamond films (SiO_2 and Si) are sacrificial and need not be preserved. So the etch recipe used in this work used CF_4 plasma. Since this work deals requires thicker diamond films to be etched, the RIE process requires a metal masking material. The metal that was used was Al as it has a lower etch rate in the specific etch recipe used for etching diamond. Al was patterned using liftoff; PR 9260 was used for the liftoff process because its higher thickness allows for thick layers of Al to be patterned. After developing the photoresist, the photoresist residue was removed using O_2 plasma in a March Asher with a power of 100 W for 3 minutes. Next the Al was deposited with a thickness of 1 μm using an Enerjet evaporator. Liftoff was performed in PRS 2000 which was agitated by ultrasound. Once the Al masking layer was prepared, the doped diamond was etched in a Plasmatherm 790 RIE system. The etch process was done at a pressure of 50 mTorr absolute, with 5 sccm CF_4 and 20 sccm Ar. The RF etch power was 300 W. The etch rate varies across the sample but is typically in the range of 0.9-1.5 μm/h. Typical etch parameters used in this work can be seen in Fig. 2-3. Fig. 2-4 shows an etched diamond film. It can be seen that the remaining SiO_2 layer beneath the diamond film is no longer smooth due to the etching with CF_4 plasma.

Table 2-3: Etch parameters for diamond films.

Parameters	**Values**	
Microwave Power	300 W	
Pressure	50 Torr	
Gases Used for Etching	Tetrafluoromethane [CF_4]	5 sccm
	Argon [Ar]	20 sccm
Etch Rate	0.9 – 1.5 μm/h	

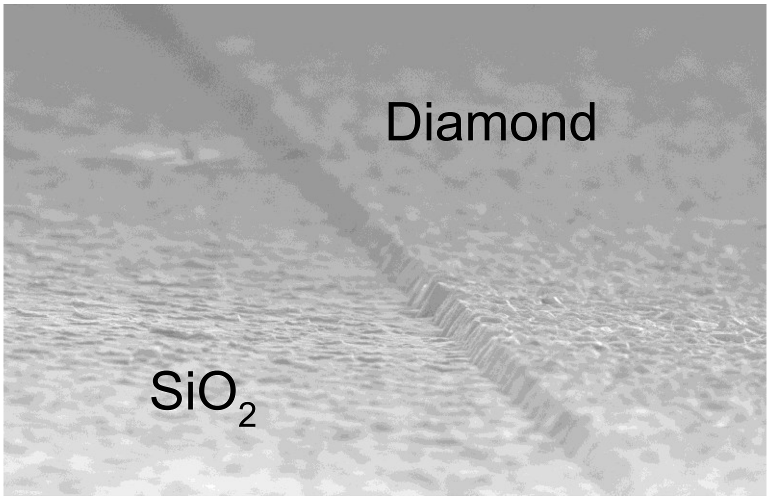

Figure 2-4: SEM of diamond patterned using RIE.

2.5 Conclusion

In this chapter, surface micromachining techniques for fabricating single-material diamond neural probes were discussed. Diamond growth via MPCVD was described and the pre-growth nucleation process was discussed. A resolution of the issue of unintentional conductivity of undoped diamond was presented where oxygen was added to the diamond growth environment. Typical growth recipes for undoped and doped diamond films were given. Finally, the patterning process of diamond was described and a typical etch recipe was presented.

REFERENCES

REFERENCES

[1] G. S. Yang, M. Aslam, K. P. Kuo, D. K. Reinhard and J. Asmussen, "Effect of ultrahigh nucleation density on diamond growth at different growth-rates and temperatures," *J. of Vacuum Science & Technology B*, vol. 13, pp. 1030-1036, 1995.

[2] A. P. Malshe, R. A. Beera, A. A. Khanolkar, W. D. Brown and H. A. Naseem, "Initial results of a novel pre-deposition seeding technique for achieving an ultrahigh nucleation density for CVD diamond growth," *Diam. and Rel. Mat* vol. 6, pp. 430-434, 1997.

[3] Y. X. Tang and D. M. Aslam, "Polycrystalline Diamond Technology and Piezoresistive Sensor Application for Cochlear Prosthesis," Ph.D. dissertation, Dept. Elect. Eng., Mich. State Univ., East Lansing, MI, 2006.

[4] A. Masood, M. Aslam, M. A. Tamor and T. J. Potter, "Techniques for patterning of CVD diamond films on non-diamond substrates," *J. of the Electrochemical Society*, vol. 138, pp. L67-L68, 1991.

[5] A. A. Morrish and P. E. Pehrsson, "Effects of surface pretreatments on nucleation and growth of diamond films on a variety of substrates," *Appl. Phy. Lett.*, vol. 59, pp. 417-419, 1991.

[6] L. Demuynck, J. C. Arnault, C. Speisser, R. Polini and F. LeNormand, "Mechanisms of CVD diamond nucleation and growth on mechanically scratched and virgin Si(100) surfaces," *Diamond and Related Materials*, vol. 6, pp. 235-239, 1997.

[7] P. A. Dennig, H. Shiomi, D. A. Stevenson and N. M. Johnson, "Influence of substrate treatments on diamond thin-film nucleation," *Thin Solid Films*, vol. 212, pp. 63-67, 1992.

[8] E. J. Bienk and S. S. Eskildsen, "The effect of surface preparation on the nucleation of diamond on silicon," *Diam. and Rel. Mat.*, vol. 2, pp. 432-437, 1993.

[9] F. S. Lauten, Y. Shigesato and B. W. Sheldon, "Diamond nucleation on unscratched SiO_2 substrates," *Appl. Phy. Lett.,* vol. 65, pp. 210-212, 1994.

[10] M. J. Chiang and M. H. Hon, "Positive dc bias-enhanced diamond nucleation with high CH_4 concentration," *Diam. and Rel. Mat*, vol. 10, pp. 1470-1476, 2001.

[11] M. D. Irwin, C. G. Pantano, P. Gluche and E. Kohn, "Bias-enhanced nucleation of diamond on silicon dioxide," *Appl. Phy. Lett.,*, vol. 71, pp. 716-718, 1997.

[12] Halliday, Resnick, Walker, Fifth Edition of Fundamentals of Physics Extended, Wiley, New York, 1997.

[13] H.O. Pierson, Handbook of Carbon, Graphite, *Diamond and Fullerenes – Properties, Processing and Applications*, William Andrew Publishing/Noyes, 2004.

[14] C. Beck and M. Ahmed, *Diamond – Chemically Vapour Deposited Diamond*, Azom, 2004.

[15] Y. Muto, T. Sugino and J. Shirafuji, "Electrical conduction in undoped diamond films prepared by chemical vapor deposition," *Applied Physics Letters*, vol. 59, pp. 843-845, 1991.

[16] B. Huang, D.K. Reinhard, "Electric field – dependent conductivity of polycrystalline diamond thin films," *Applied Physics Letters*, vol. 59, pp. 1494-1496, 1991.

[17] M. Werner, O. Dorsch, A. Hinze, E. Obermeier, R.E. Haper, C. Johnston, P.R. Chalker and I.M. Buckley-Golder, "Space-charge-limited current flow and trap density in undoped diamond films," *Diamond and Related Materials*, vol. 13, pp. 825-828, 1993.

[18] T. Sugino, Y. Muto, J. Shirafuji and K. Kobashi, "Electrical conduction mechanisms in polycrystalline chemically vapour-deposited diamond films," *Diamond and Related Materials*, vol. 2, pp. 797-802, 1993.

[19] S. Jin and T.D. Moustakas, "Electrical conductivity studies of diamond films prepared by electron cyclotron resonance microwave plasma," *Applied Physics Letters*, pp. 2354-2356, 1993.

[20] A.K. Kulkarni, A. Shrotriya, P. Cheng, H. Rodrigo, R. Bashyam and D.J. Keeble, "Electrical properties of diamond thin films grown by chemical vapor deposition technique," *Thin Solid Films*, vol. 253, pp. 141-145, 1994.

[21] A.K. Kulkarni, K. Tey and H. Rodrigo, "Electrical characterization of CVD diamond thin films grown on silicon substrates," *Thin Solid Films*, vol. 270, pp. 189-193, 1995.

[22] G. De Cesare, S. Salvatori, R. Vincenzoni, P. Ascarelli, E. Cappelli, F. Pinzari and F. Galluzzi, "On the electrical properties of polycrystalline diamond films on silicon," *Diamond and Related Materials*, vol. 4, pp. 628-631, 1995.

[23] A.K. Sikder, A.P. Jacob, T. Sharda, D.S. Misra, M. Pandey, D. Kabiraj and D.K. Avasthi, "DC electrical conductivity of chemical vapour deposited diamond sheets: a correlation with hydrogen content and paramagnetic defects," *Thin Solid Films*, vol. 332, pp. 98-102, 1998.

[24] L. Wang, Y. Xia, J. Ju and W. Zhang, "Electrical properties of chemical vapor deposition diamond films and electrical response to X-ray," *Diamond and Related Mateirals*, vol. 9, pp. 1617-1620, 2000.

[25] B.J. Lee, B.T. Ahn, J.K. Lee and Y.J. Baik, "A study on the conduction path in undoped polycrystalline diamond films," *Diamond and Related Materials*, vol. 10, pp. 2174-2177, 2001.

[26] Q. Su, J. Lu, L. Wang, J. Liu, J. Ruan, J. Cui, W. Shi and Y. Xia, “Electrical properties of [100]-oriented CVD diamond film,” *Solid-State Electronics*, vol. 49, pp. 1044-1048, 2005.

[27] E.J. Correa, Y. Wu, J. Wen, R. Chandrasekharan and M. Shannon, “Electrical conduction in undoped ultrananocrystalline diamond thin films and its dependence on chemical composition and crystalline structure,” *Journal of Applied Physics*, vol. 102, 2007.

[28] B.R. Stoner, J.T. Glass, L. Bergman, R.J. Nemanich, L.D. Zoltal and J.W. Vandersande, “Electrical conductivity and photoluminescence of diamond films grown by downstream microwave plasma CVD,” *Journal of Electronic Materials*, vol. 21, pp. 629-634, 1992.

[29] G.S. Sandhu, and W.K. Chu, “Reactive ion etching of diamond,” *Applied Physics Letter*, vol. 55, no. 5, pp.437-438, 1989.

[30] O. Dorsch, M. Werner and E. Obermeier, “Dry etching of undoped and boron doped polycrystalline diamond films,” *Diamond & Related Materials*, vol. 4, pp.456-459, 1995.

[31] C. Vivensang, L. Ferlazzo-Manin, and M.F. Ravet, “Surface smoothing of diamond membranes by reactive ion etching process,” *Diamond & Related Materials*, vol. 5, pp. 840-844, 1996.

[32] Gopi M.R. Sirineni, H.A. Naseem, A.P. Malshe, and W.D. Brown, “Reactive ion etching of diamond as a means of enhancing chemically-assisted mechanical polishing efficiency,” *Diamond and Related Materials*, vol. 6, pp. 952-958, 1997.

[33] H. Shiomi, “Reactive ion etching of diamond in O_2 and CF_4 Plasma, and fabrication of porous diamond for field emitter cathodes,” *Japanese Journal of Applied Physics*, vol. 36, pp. 7745-7748, 1997.

[34] E.-S. Baik, and Y.-J. Baik, “Aligned diamond nanowhiskers,” *Journal of Materials Research*, vol. 15, no. 14, pp. 923-926, 2000.

[35] E.-S. Baik, Y.-J. Baik, S.W. Lee, and D. Jeon, “Fabrication of diamond nano-whiskers,” *Thin Solid Films*, no. 377-378, pp. 295-298, 2000.

[36] E.-S. Baik, Y.-J. Baik, and D. Jeon, “Control of diamond micro-tip geometry for field emitter,” *Thin Solid Films*, no. 377-378, pp. 299-302, 2000.

[37] T. Shibata, Y. Kitamoto, K. Unno, and E. Makino, “Micromachining of diamond film for MEMS applications,” *Journal of Microelectromechanical Systems*, vol. 9, no. 1, pp. 47-51, 2000.

[38] R. Otterbach, U. Hilleringmann, and K. Goser, “Reactive ion etching of CVD-diamond for sensor devices with Al feature size of 100 nm,” *Industrial Electronics Society Conference*, vol.3, pp. 1873-1877, 2000.

[39] Y. Nishibayashi, Y. Ando, H. Saito, T. Imai, T. Hirao, and K. Oura, "Anisotropic etching of a fine column on a single crystal diamond," *Diamond and Related Materials*, vol. 10, pp. 1732-1735, 2001.

[40] P.W. Leech, G.K. Reeves, and A. Holland “Reactive ion etching of diamond in CF_4, O_2, O_2 and Ar-based mixtures,” *Journal of Materials Science*, vol. 36, no. 14, pp. 3453-3459, 2001.

[41] Y. Fu, H. Du, and J. Miao, “Patterning of diamond microstructures on Si substrate by bulk and surface micromachining,” *Journal of Materials Processing Technology*, 132, pp. 73-81, 2003.

[42] X. Wang, G.D. Hong, J. Zhang, B.L. Lin, H.Q. Gong, and W.Y. Wang, "Precise patterning of diamond films for MEMS application," *Journal of Materials Processing Technology*, vol. 127, pp. 230-233, 2002.

[43] Y. Ando, Y. Nishibayashi, K. Kobashi, T. Hirao, and K. Oura, “Smooth and high-rate reactive ion etching of diamond,” *Diamond and Related Materials*, vol. 11, pp. 824-827, 2002.

[44] Y. Ando, Y. Nishibayashi, A. Sawabe, “‘Nano-rods’ of single crystalline diamond,” *Diamond and Related Materials*, vol. 13, pp. 633-637, 2004.

[45] C.Y. Li, and A. Hatta, “Effect of metal coating on the formation of diamond whiskers in O_2 RF plasma,” *Diamond & Related Materials*, vol. 15, pp. 357-360, 2006.

[46] G. Ding, H. Mao, Y. Cai, Y. Zhang, X. Yao, and X.L. Zhao, “Micromachining of CVD diamond by RIE for MEMS applications,” *Diamond & Related Materials*, vol. 14, pp. 1543-1548, 2005.

[47] C.Y. Li, and A. Hatta, “Preparation of diamond whiskers using Ar, O_2 plasma etching,” *Diamond & Related Materials*, vol. 14, pp. 1780-1783, 2005.

[48] C.Y. Li, and A. Hatta, “Nanowhiskers formation by radio frequency Ar/O_2 plasma etching of Al coated diamond films,” *Thin Sold Films*, vol. 515, pp. 4172-4176, 2007.

[49] M.D. Stoikou, P. John, and J.I. Wilson, "Unusual morphology of CVD diamond surfaces after RIE," *Diamond and Related Materials*, vol. 17, pp. 1164-1168, 2008.

[50] H. Y. Chan, D. M. Aslam, J. A. Wiler, and B. & Casey, “A novel diamond microprobe for neuro-chemical and-electrical recording in neural prosthesis,” *Microelectromechanical Systems, Journal of*, vol. 18(3), pp. 511-521, 2009.

[51] H.Y. Chan, “Polycrystalline CVD Diamond Probes for use in In Vivo and In Vitro Neural Studies,” Ph.D. dissertation, Dept. Elect. Eng., Mich. State Univ., East Lansing, MI, 2008.

[52] Z. Cao and D. Aslam, “Fabrication technology for single-material MEMS using polycrystalline diamond,” *Diamond and Related Materials*, vol. 19(10), pp. 1263-1272, 2010.

[53] Z. Cao, “Single-material MEMS using Polycrystalline Diamond,” Ph.D. dissertation, Dept. Elect. Eng., Mich. State Univ., East Lansing, MI, 2011.

CHAPTER 3:

Neural Probe Fabrication

3.1 Introduction

As no testing could be conducted without probes, the most critical step in this work must be the fabrication of the single-material diamond neural probes. But before single-material diamond probes could be fabricated, the previous diamond probe technology had to be repeated in order to learn the processing techniques required and to produce samples for comparison. This chapter discusses the fabrication process for making diamond neural probes and single-material diamond neural probes. In order to understand the purpose of this work, it is important to understand the differences between the diamond neural probes fabricated in this (and previous) work and the single-material diamond neural probes that are unique to this work.

Single-material diamond probes are fabricated entirely out of polycrystalline diamond. However, other materials are used during fabrication and for the devices' electrical interface. The six-electrode variant of the single-material diamond probes are approximately 99.6% diamond by volume with the remaining portion making up the metal pads on the backend of the probe. Previous "all-diamond" neural probe research [1-4] were <30% diamond by, using the same probe geometry. The previous "all-diamond" probes included a Si backend, multiple SiO_2 insulating layers, and Au interconnects. Even discounting the Si backend, the front portion of these probes, which is inserted into the brain, is ~50% diamond by volume. It is immediately apparent that the current research differs dramatically from earlier research in terms of process and materials used.

While the final single-material diamond probe is comprised almost entirely of diamond, other materials are utilized during fabrication. Probes are fabricated on top of a Si substrate with a 1 μm layer of SiO_2. Furthermore, Al is used as a masking layer during each of the diamond patterning steps. Finally, as previously stated, Cr and Au are used to make the pads on the backend of the probe for the electrical interface. After each etch step, the Al masking layer is removed, and after the final step, the Si/SiO_2 substrate is removed.

In this chapter, the fabrication processes for each probe type is discussed. Each process is illustrated and detailed process steps for each method are presented. In addition, micrographs of the single-material diamond neural probes are shown. The design and layout of the diamond-based neural probes has been presented in [4], the SMM diamond neural probes share the same layout with a reduced number of masks.

3.2 Diamond Neural Probe Fabrication

Diamond probe fabrication is accomplished in 12 major steps, beginning with an n-Si wafer. The Si wafer is selectively doped p^{++} in order to form the thick Si backend of the probe (Fig 3-1a). The p^{++}-Si is used as a chemical etch stop during the final probe release step. After doping the Si, a layer of SiO_2 is deposited on the wafer (Fig 3-1b). The wafer is then seeded with diamond and undoped diamond is grown (Fig. 3-1c). Next an insulating layer of oxide is deposited on the undoped diamond (Fig 3-1d). The wafer is again seeded and doped diamond is grown (Fig 3-1e). Next, two diamond patterning steps are performed. First the doped diamond is patterned in order to form electrodes (Fig. 3-1f). The backside oxide is etched as it is an unwanted masking material for probe release (Fig. 3-2g). Then, the underlying undoped diamond is patterned to form the shape of the probes (Fig. 3-2h). A dielectric layer of SiO_2 is deposited and patterned (Fig. 3-2i). Next, a Ti/Au layer is deposited and patterned using liftoff to form interconnects and backend pads (Fig. 3-2j). SiO_2 is deposited as the top insulating layer and is patterned using a buffered HF solution (Fig. 3-2k). The final fabrication step is releasing the probes, which is done by EDP (Fig. 3-2l).

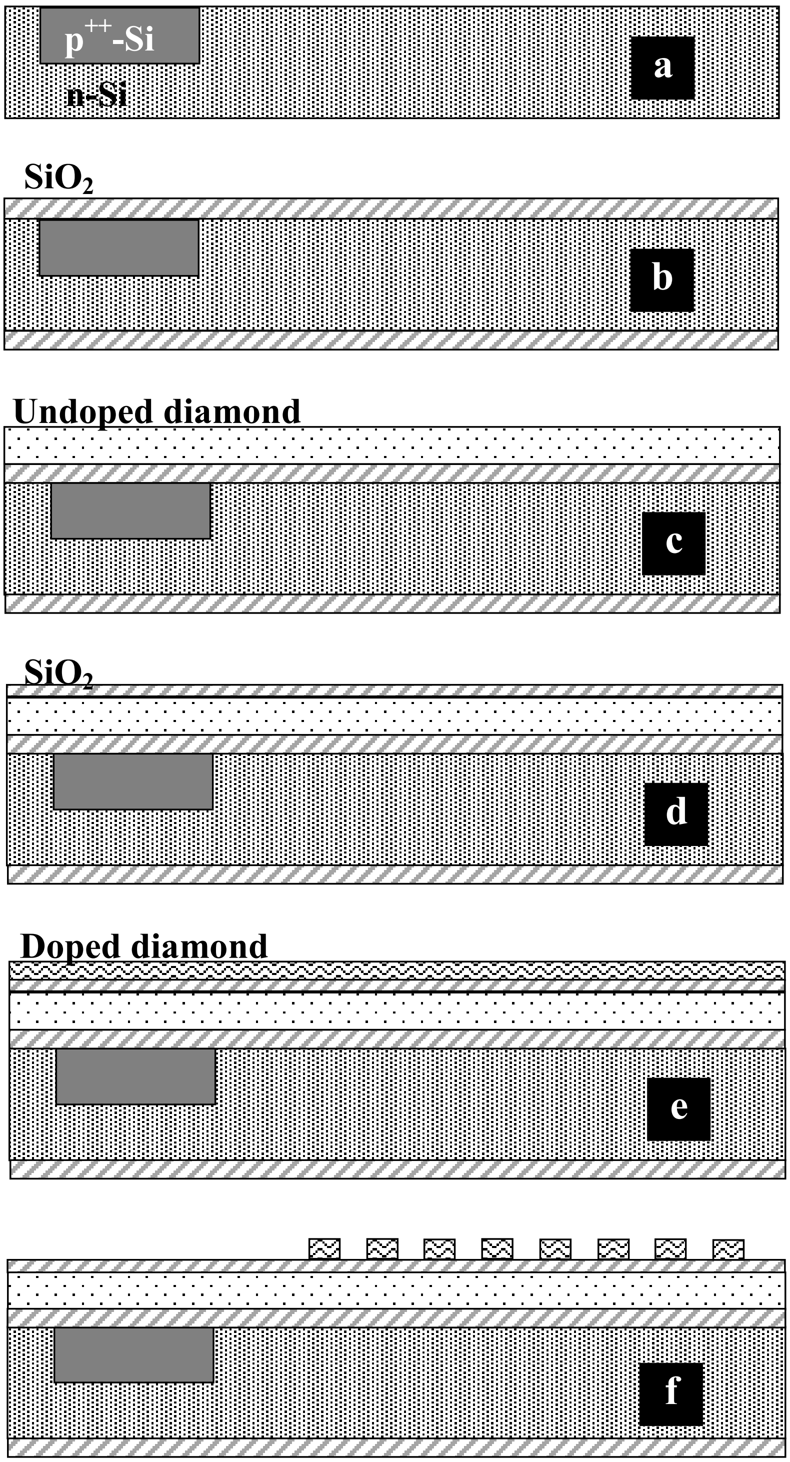

Figure 3-1: First part of diamond neural probes fabrication process. (a) p^{++} Si doping of backend. (b) Deposition of dielectric layer. (c) Growth of undoped diamond. (d) Deposition of dielectric layer. (e) Growth of doped diamond. (f) Patterning of doped diamond.

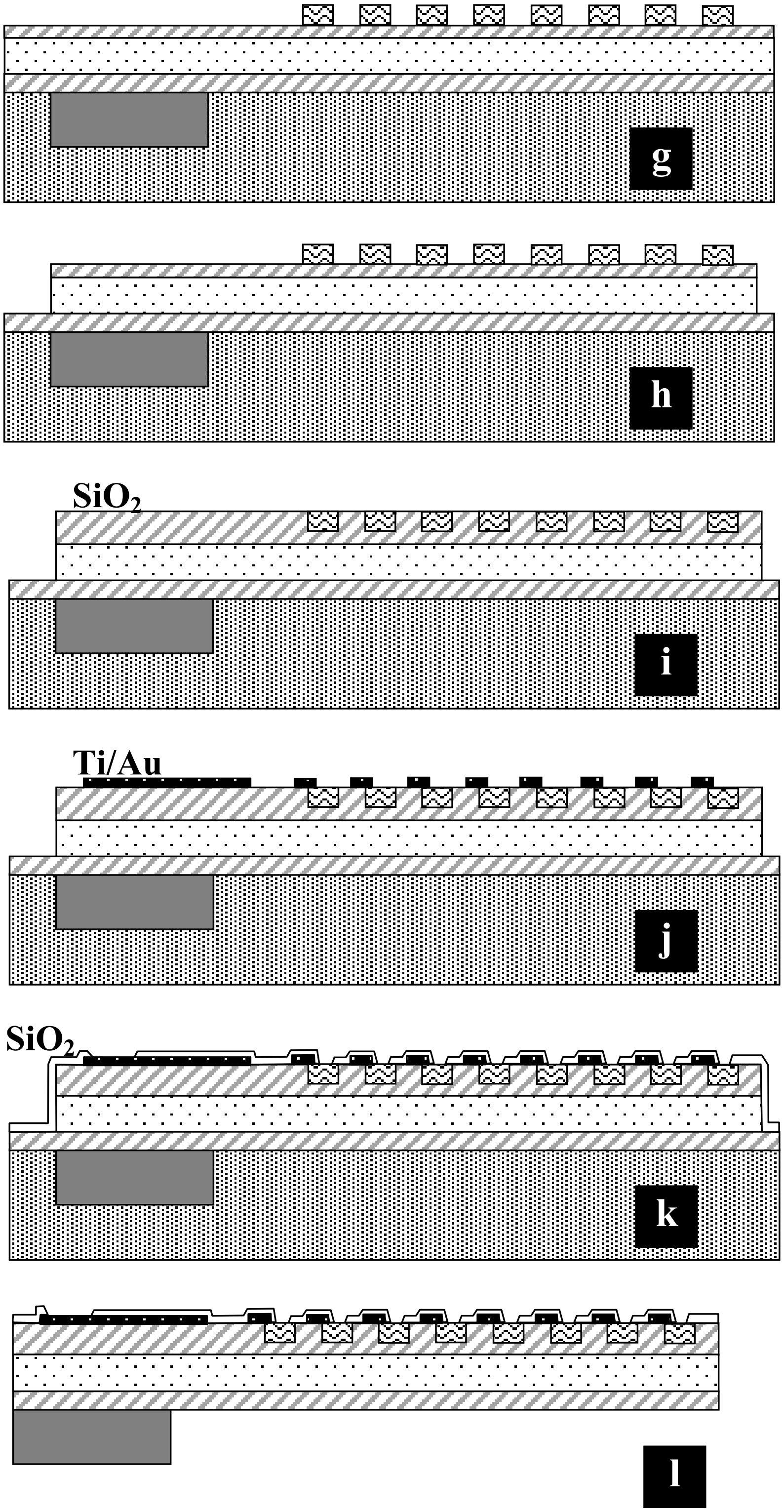

Figure 3-2: Second part of diamond neural probe fabrication process. (g) Removal of backside oxide. (h) Patterning of undoped diamond. (i) Deposition and patterning of dielectric layer. (j) Deposition of Ti/Au interconnects. (k) Deposition and patterning of SiO$_2$ top insulating layer. (l) Probe release via EDP.

The first major step in the fabrication of diamond neural probes is defining the backend of the probe by selectively doping the n-Si wafer heavily with B (p^{++}). This is done so that the backend of the probes is not etched away during the release step in EDP. The reason for keeping a layer of Si underneath the backend of the probes is to make sure that the probes could be handled and bonded without breaking the backend of the probes. Silicon-based probes have a thicker backend as well for this same reason. In order to selectively dope the silicon wafer, a layer of oxide was first grown on the wafer. Before growing the oxide, an RCA clean was performed to remove any metallic or organic contaminants from the surface of the wafer. The oxide was patterned with buffered HF using the first mask. Another RCA clean was performed to remove the photoresist and any contaminants. Deep boron diffusion and drive-in are performed in separate furnaces. After the boron doping, the masking oxide layer was removed in HF.

The next step in the fabrication process is dielectric deposition. The purpose of this step is to prevent out-diffusion of boron during the diamond growth steps, which would lead to unintentional doping of the undoped diamond film. Before depositing oxide, another RCA clean was performed to remove impurities. This step can be skipped if the oxide deposition is done immediately after the previous step, as HF will remove any metal or organic residue from the wafer. To complete this step, LPCVD oxide was deposited, at 450 °C, on the wafer.

Before diamond growth can be achieved, diamond nanoparticles must be spread over the substrate, a process known as diamond seeding (or nucleation). Seeding was performed using a 0.5% solution of ~0.1 μm diamond particles in water. Before seeding can effectively be performed on SiO_2, the surface needs to be refreshed to become hydrophilic. This was done by briefly etching the SiO_2 surface in diluted hydrofluoric acid for a short time (<30 seconds). The diamond solution must also be prepared, which has been done using an ultrasonic bath to agitate the solution for 30 minutes to ensure an even distribution of diamond particles. Once the solution and substrate are prepared, some diamond solution was pipetted onto the substrate until about 70% of the substrate was covered. At this point, the wafer was spun at 500 RPM for 5 seconds and then 2000 RPM for 30 seconds to evenly distribute diamond particles over the substrate. Diamond growth was accomplished using microwave-plasma-assisted chemical vapor deposition (MPCVD). Before the growth process, the MPCVD chamber was pumped to a vacuum of less than 20 mTorr absolute pressure. Once the chamber has been evacuated, gas flow was initiated and the pressure in the chamber was maintained at 40 Torr absolute. The main constituent of the growth plasma was H_2, as such H_2 has the highest flow rate of 100 sccm. Once the pressure has stabilized, the MPCVD was started and the output power was slowly increased to 2.3 kW as the temperature increases to about 750 °C. The source of carbon for diamond growth was CH_4 which was next added at a rate of 1.5 sccm. Undoped diamond was allowed to grow for 20 hours to form the structural backing of the probes. After the diamond growth process there was a layer of undoped diamond that was approximately 3 μm thick. The quality of diamond was experimentally verified using Raman spectroscopy to verify the main peak of Raman shift was at 1332 cm^{-1}, as expected.

Next another layer of oxide was deposited on top of the undoped diamond. This dielectric layer prevents conduction between interconnects through the undoped diamond. This is necessary due to the poor resistivity (~10^2-10^3 Ω-cm) of the undoped diamond. A layer of PECVD oxide with a thickness of ~1 μm was deposited on the wafer. Annealing of the oxide was done using rapid thermal processing, 10 minutes at 650 °C, 10 minutes at 750 °C, and finally 3 minutes at 970 °C.

Next doped diamond was grown. Because the top layer of the wafer was oxide, the wafer must first be seeded as described before for undoped diamond growth. The growth parameters in the MPCVD are almost the same, except the gases used are different. In doped diamond growth the gases used are H_2, CH_4, and trimethlyborane [$B(CH_3)_3$] diluted in H_2 to 0.005% as a boron source. The flow rates used are 100 sccm of H_2, 1 sccm of CH_4, and 2 sccm of diluted $B(CH_3)_3$. The diamond was grown for 13 hours and the resulting layer was approximately 1 μm thick.

The next fabrication step is patterning the doped diamond layer to form the electrodes of the probes. Diamond was patterned using RIE with Al as a masking layer. For this mask, photoresist 1827 was patterned using the second mask. Then 1 μm of Al was deposited on the sample. The Al was patterned through a lift-off process. Diamond was then etched in O_2 plasma at 50 mTorr with 300 W of RF power for 2 hours. Etching diamond in pure O_2 plasmas leaves columnar microstructures of diamond called diamond whiskers. These diamond whiskers were removed by immersing the sample in diluted HF for 10 seconds. Finally, the Al mask was removed using Al Etch A, a combination of H_3PO_4, HNO_3, and $C_2H_4O_2$.

Next the backside oxide was etched. This step is important to the probe fabrication because oxide has a very low etch rate in EDP, which is used to release the probes. Leaving the oxide on the backside of the wafer would make the release process take much longer. The front side of the wafer was protected by spinning photoresist 9260. The oxide was etched using buffered HF for 15 minutes. The photoresist was then removed using acetone.

The next fabrication step is to pattern the undoped diamond to from the probe sheaths. Again, an Al mask was used for the RIE of diamond. However, for this step the mask was patterned using wet etching of Al rather than lift-off. First, 1 µm of Al was deposited on the wafer. Then the negative photoresist 5214 was patterned using mask 3. The Al was patterned using Al Etch A and the photoresist was removed using acetone. RIE was performed with a more aggressive recipe that had 20 sccm of O_2 and 5 sccm of CF_4, at 50 mTorr with 300 W of RF power, for 3 hours. The Al mask was then removed using Al etch A.

Next a dielectric layer of oxide was deposited and patterned. 1 µm of PECVD oxide was deposited on the wafer. The second mask (boron-doped diamond) was used in order to expose the electrodes. For this mask, photoresist 9260 was used as a mask. The oxide was etched by RIE using a typical SiO_2 etching recipe for 50 minutes. The remaining photoresist residue was removed using acetone and ashing in O_2 plasma. The dielectric layer was also patterned using the third mask (undoped diamond). For this mask, photoresist 5214 had to be used. However, since 5214 is a much thinner photoresist than 9260, the patterning of photoresist and etching of oxide had to be done twice. The 5214 would be etched completely in 50 minutes of RIE, so there were two separate RIE sessions of 25 minutes each. The photoresist residue between RIE and after RIE was removed using acetone and O_2 plasma ashing.

At this point, additional steps could be taken to deposit electrodes of different metals. In the past, probes had been fabricated with Pt and Ag electrodes in addition to boron-doped diamond electrodes for electrochemical detection applications. These electrodes would be deposited using a lift-off process as described before. Each electrode type requires an additional mask.

Next the metal interconnects and contact pads were deposited on the probes. This was done with a lift-off process using photoresist 9260. The photoresist was patterned with the fourth mask (interconnects and pads). Ti and Au were deposited on the probes with thickness of 500 Å and 4000 Å respectively. The Ti layer was necessary because it has better adhesion to diamond and creates an ohmic contact with boron-doped diamond. Lift-off was performed in acetone.

The next fabrication step is the deposition and patterning of the top oxide insulating layer. This layer protects the interconnects so that only the electrodes and backend pads are exposed. 2 μm of PECVD oxide was deposited on the sample. Photoresist 9260 was patterned using the fifth mask (top insulator). The oxide layer was etched using RIE with a standard oxide etch recipe for 90 minutes. The remaining photoresist residue was removed using acetone and O_2 plasma ashing.

The final fabrication step is releasing the probes. This is done by first thinning the wafer using HF and nitric acid. Before thinning the wafer, the front side is protected by a layer of wax. The wafer was then thinned in the acid mixture for 30 minutes. Then the wax was removed and the probes were released by dissolving the remainder of the n-Si using ethlyenediamine pyrocatechol (EDP). Finally the released probes were thoroughly rinsed. At this point the diamond neural probe fabrication is complete and the probes are ready for packaging and testing. Pictures of these probes can be seen in Fig. 3-3. The complete fabrication process is detailed in Table 3-1.

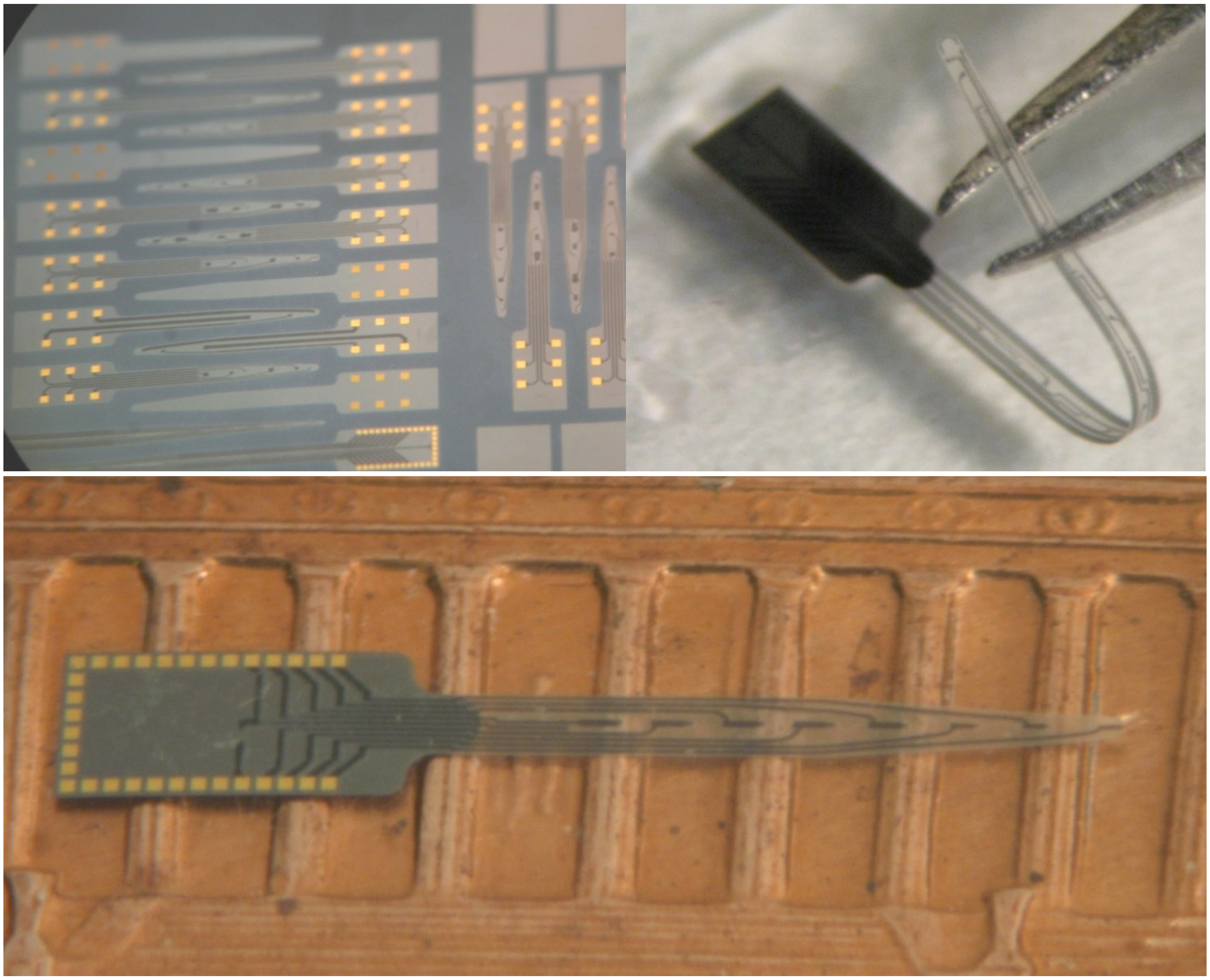

Figure 3-3: Fabricated diamond neural probes: before release (top-left), being manipulated by forceps (top-right), and on the back of a US one-cent coin (bottom).

Table 3-1: Fabrication process for diamond neural probes.

Process Step		Detail	Equipment	Parameters
Pattern Probe Backend	Pre-furnace Clean		Wet Bench	RCA Clean of n-Si wafer
	Grow Oxide	Oxide thickness ≈1.2 μm	B2 tube	Recipe: DWD/TCA Parameter Table: DWDSKIN 4 hours, 1000 °C
	Spin 1813	Photoresist thickness ≈1.4 μm	Spinner	4000 RPM, 30 seconds
	Soft Bake		Hotplate	1 minute, 95 °C
	Expose	Mask 1: BDF	MA6	5 seconds
	Develop Photoresist		Wet Bench	MIF 318, 1 minute
	Oxide Etch		Wet Bench	BHF, 17 minutes
	Pre-furnace Clean		Wet Bench	RCA Clean
	Deep Boron Diffusion		A2 tube	Recipe: BEDEP99 Parameter Table: BORON99 5 hours, 1175 °C
	Drive-in		A4 tube	Recipe: N2ANL/OX Parameter Table: N2ANL/OX 5 hours, 1175 °C
	Oxide Etch	Strips deep boron masking oxide	Wet Bench	$HF:H_2O$ (1:1), 7 minutes
Dielectric Deposition	Pre-furnace Clean		Wet Bench	RCA Clean
	LPCVD Oxide	Oxide thickness ≈1.2 μm	D4 tube	Recipe: HTO 3 hours 17 minutes, 450 °C
Undoped Diamond Growth	Refresh Oxide Surface		Wet Bench	$HF:H_2O$ (1:7), 5 seconds
	Diamond Nucleation	0.5% Diamond powder loaded water	Spinner	500 RPM for 5 seconds, 2000 RPM for 30 seconds
	Diamond Growth	Diamond thickness ≈3 μm	MPCVD	$H_2:CH_4$ (100:1.5 sccm), 2.3 kW, 20 hours, 750 °C
Dielectric Deposition	PECVD Oxide	Oxide thickness ≈1 μm	PECVD	
	Annealing		RTP	10 minutes, 650 °C
	Annealing		RTP	10 minutes, 750 °C
	Annealing		RTP	3 minutes, 970 °C

Table 3-1 (cont'd)

Process Step		Detail	Equipment	Parameters
Doped Diamond Growth	Refresh Oxide Surface		Wet Bench	HF:H_2O (1:7), 5 seconds
	Diamond Nucleation	0.5% Diamond powder loaded water	Spinner	500 RPM for 5 seconds, 2000 RPM for 30 seconds
	Diamond Growth	Diamond thickness ≈1 μm	MPCVD	H_2:CH_4:TMB (100:1:2), 2.3 kW,13 hours, 750 °C
Pattern Doped Diamond	Spin 1827	Photoresist thickness ≈3 μm	Spinner	3000 RPM, 30 seconds
	Soft Bake		Hotplate	1 minute, 95 °C
	Expose	Mask 2: BDP	MA6	17 seconds
	Develop Photoresist		Wet Bench	MIF 318, 1 minute
	Masking Layer Deposition	Al thickness ≈1 μm	Enerjet Evaporator	Al 10000 Å
	Ashing		March Asher	O_2, 100 W, 1 minute
	Lift-off		Wet Bench	Acetone, 2 hours
	RIE		PlasmaTherm 790	O_2 20 sccm, 300 W, 50 mTorr, 2 hours
	Remove Diamond Whiskers		Wet Bench	HF:H_2O (1:7), 10 seconds
	Remove Al Mask		Wet Bench	Al Etchant Type A
Etch Backside Oxide	Spin 9260	Photoresist thickness ≈6 μm	Spinner	4000 RPM, 30 seconds
	Oxide Etch		Wet Bench	BHF, 15 minutes
	Remove Photoresist		Wet Bench	Acetone

Table 3-1 (cont'd)

Process Step		Detail	Equipment	Parameters
Pattern Undoped Diamond	Masking Layer Deposition	Al thickness ≈1 μm	Enerjet Evaporator	Al 10000 Å
	Spin 5214	Photoresist thickness ≈1.6 μm	Spinner	3000 RPM, 30 seconds
	Soft Bake		Hotplate	1 minute, 95 °C
	Expose	Mask 3: UDP	MA6	4 seconds
	Hard Bake		Hotplate	1.5 minutes, 115 °C
	Flood Expose		MA6	1 minute
	Develop Photoresist		Wet Bench	AZ300, 1 minute
	Pattern Mask		Wet Bench	Al Etchant Type A
	Remove Photoresist		Wet Bench	Acetone
	RIE		PlasmaTherm 790	O_2:CF_4 (20:5 sccm), 300 W, 50 mTorr, 3 hours
	Remove Al Mask		Wet Bench	Al Etchant Type A
Dielectric Deposition and Patterning	PECVD Oxide	Oxide thickness ≈1 μm	PECVD	
	Spin 9260	Photoresist thickness ≈6 μm	Spinner	4000 RPM, 30 seconds
	Soft Bake		Hotplate	2.5 minutes, 95 °C
	Expose	Mask 2: BDP	MA6	35 seconds
	Develop Photoresist		Wet Bench	AZ400:H_2O (4:1), 2 minutes
	RIE		PlasmaTherm 790	Recipe: n_SiO2, 50 minutes
	Remove Photoresist		Wet Bench	Acetone
	Ashing		March Asher	O_2, 100W, 100 seconds
	Spin 5214	Photoresist thickness ≈1.6 μm	Spinner	3000 RPM, 30 seconds
	Soft Bake		Hotplate	1 minute, 95 °C
	Expose	Mask 3: UDP	MA6	4 seconds
	Hard Bake		Hotplate	1.5 minutes, 115 °C
	Flood Expose		MA6	1 minute

Table 3-1 (cont'd)

Process Step		Detail	Equipment	Parameters
Dielectric Deposition and Patterning	Develop Photoresist		Wet Bench	AZ300, 1 minute
	RIE		PlasmaTherm 790	Recipe: n_SiO2, 25 minutes
	Remove Develop Photoresist		Wet Bench	Acetone
	Ashing		March Asher	O_2, 100W, 100 seconds
	Spin 5214	Photoresist thickness ≈1.6 µm	Spinner	3000 RPM, 30 seconds
	Soft Bake		Hotplate	1 minute, 95 °C
	Expose	Mask 3: UDP	MA6	4 seconds
	Hard Bake		Hotplate	1.5 minutes, 115 °C
	Flood Expose		MA6	1 minute
	Develop Photoresist		Wet Bench	AZ300, 1 minute
	RIE		PlasmaTherm 790	Recipe: n_SiO2, 25 minutes
	Remove Develop Photoresist		Wet Bench	Acetone
	Ashing		March Asher	O_2, 100W, 100 seconds
Pattern Counter Electrode (Optional Electrochemical Probe Step)	Spin 9260	Photoresist thickness ≈6 µm	Spinner	4000 RPM, 30 seconds
	Soft Bake		Hotplate	2.5 minutes, 95 °C
	Expose	Mask 4: CEP	MA6	35 seconds
	Develop Photoresist		Wet Bench	AZ400:H_2O (4:1), 2 minutes
	Ashing		March Asher	O_2, 100 W, 1 minute
	Metal Deposition		SJ20 Evaporator	Ti/Au 500/4000 Å
	Lift-off		Wet Bench	Acetone, 2 hours
Pattern Reference Electrode (Optional Electrochemical Probe Step)	Spin 9260	Photoresist thickness ≈6 µm	Spinner	4000 RPM, 30 seconds
	Soft Bake		Hotplate	2.5 minutes, 95 °C
	Expose	Mask 5: REP	MA6	35 seconds
	Develop Photoresist		Wet Bench	AZ400:H_2O (4:1), 2 minutes
	Ashing		March Asher	O_2, 100 W, 1 minute
	Metal Deposition		Enerjet Sputterer	Ti/Au/Ag 100/80/4000 Å
	Lift-off		Wet Bench	Acetone, 2 hours

Table 3-1 (cont'd)

Process Step		Detail	Equipment	Parameters
Pattern Metal Interconnects	Spin 9260	Photoresist thickness ≈6 μm	Spinner	4000 RPM, 30 seconds
	Soft Bake		Hotplate	2.5 minutes, 95 °C
	Expose	Mask 6: IP	MA6	35 seconds
	Develop Photoresist		Wet Bench	AZ400:H_2O (4:1), 2 minutes
	Ashing		March Asher	O_2, 100 W, 1 minute
	Metal Deposition		SJ20 Evaporator	Ti/Au 500/4000 Å
	Lift-off		Wet Bench	Acetone, 2 hours
Top Oxide Insulator	PECVD Oxide	Oxide thickness ≈2 μm	PECVD	
	Spin 9260	Photoresist thickness ≈6 μm	Spinner	4000 RPM, 30 seconds
	Soft Bake		Hotplate	2.5 minutes, 95 °C
	Expose	Mask 7: TIP	MA6	35 seconds
	Develop Photoresist		Wet Bench	AZ400:H_2O (4:1), 2 minutes
	RIE		PlasmaTherm 790	Recipe: n_SiO2, 90 minutes
	Remove Photoresist		Wet Bench	Acetone
	Ashing		March Asher	O_2, 100W, 100 seconds
Probe Release	Wafer Thinning		Wet Bench	HF-Nitric, 30 minutes
	Probe Release		Wet Bench	EDP, 4 hours, 115 °C

3.3 Single-material Diamond Neural Probe Fabrication

SMM probe fabrication is accomplished is 7-8 major steps, depending on the application. A schematic of these steps can be seen in Fig. 3-4. The substrate is a Si wafer coated in 1 μm of SiO_2 (Fig. 3-4a). The first step is growing undoped and then doped diamond (Fig. 3-4b). Next the doped diamond layer is patterned to form the electrodes, interconnects, and pads (Fig. 3-4c). Then an additional layer of undoped diamond is grown over the probes (Fig. 3-4d). Next the probe shapes are defined by patterning the undoped diamond all the way down to the substrate (Fig. 3-4e). Then the electrodes and pads are exposed by etching the top layer of undoped diamond (Fig. 3-4f). Next, the metal pads are deposited on top of the exposed doped diamond pads (Fig. 3-4g). Optionally, the electrodes can be selectively modified for other applications (Fig. 3-4h). Finally, the probes are released from the substrate by chemically etching the SiO_2 from underneath the probes (fig. 3-4i).

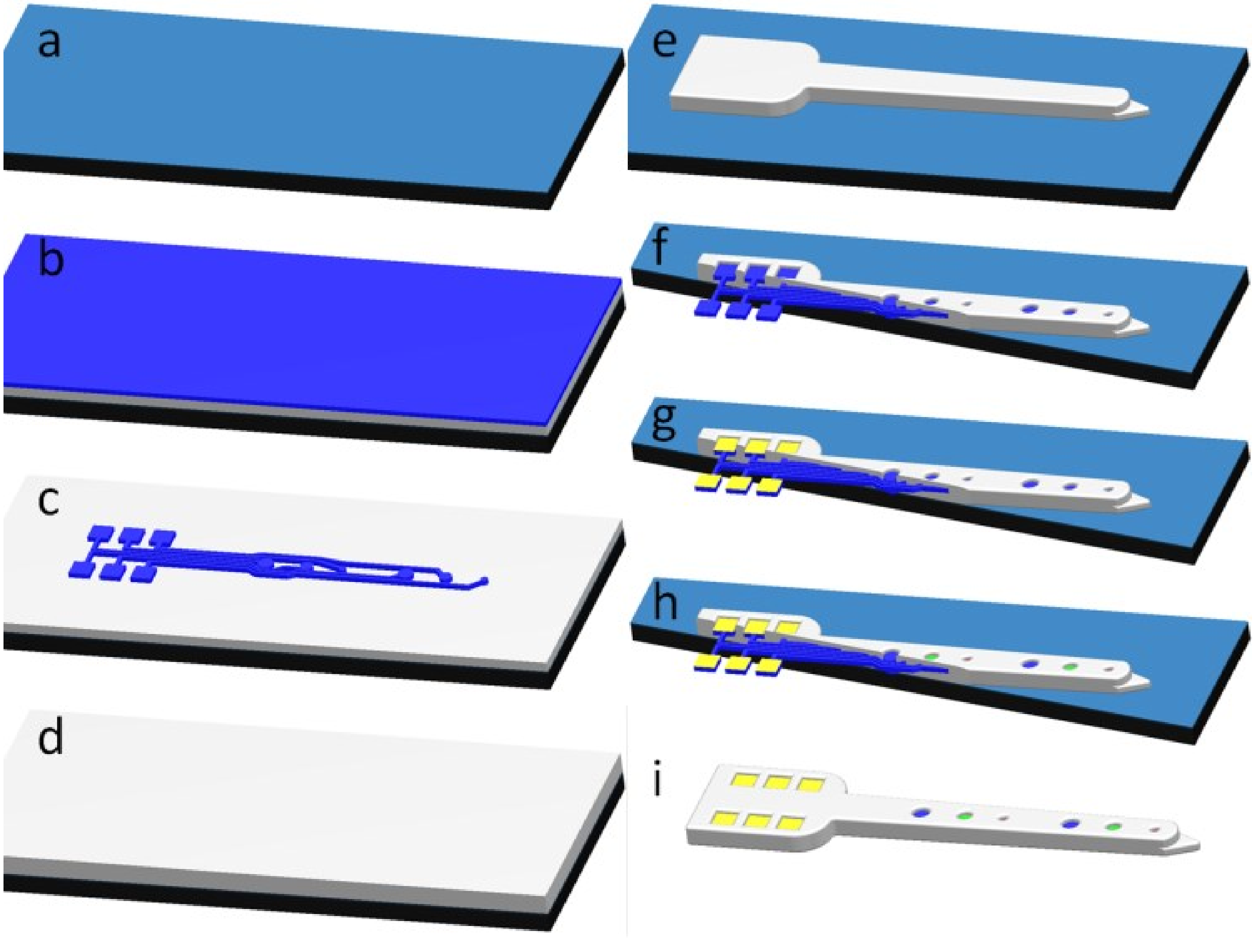

Figure 3-4: SMM probe fabrication process. (a) Si/SiO2 Substrate. (b) Undoped and doped diamond growth. (c) Doped diamond patterning. (d) Undoped diamond growth. (e) Probe patterning. (f) Insulation patterning. (g) Metal pad deposition. (h) Optional electrode modification. (i) Probe release.

Before SMM diamond probes can be fabricated, an appropriate substrate must be prepared. Almost any material with a melting point above 900 °C could be used. However, other useful characteristics are a thermal expansion coefficient similar to poly-C, resistance to out-diffusion of potential diamond dopants, mechanical strength, and it must be able to be chemically etched. As such, sapphire would appear to be an ideal candidate. For the purpose of cost reduction, a 750 μm thick, n-type Si wafer with a 1 μm layer of SiO_2, hand-cut to a size of 5 cm by 5 cm, was used.

Before diamond growth can be achieved, diamond nanoparticles must be spread over the substrate, a process known as diamond seeding (or nucleation). Seeding was performed using a 5% solution of diamond particles in water. As such, before seeding can effectively be performed on Si or SiO_2, the surface needs to be modified to become hydrophilic. This can be done by briefly etching the Si or SiO_2 surface. Typically diluted hydrofluoric acid is used for a short time (<30 seconds) to achieve this aim. Alternatively, O_2 plasma has been used for similar results. The diamond solution must also be prepared, which has been done using an ultrasonic bath to agitate the solution for 30 minutes to ensure an even distribution of diamond particles. Once the solution and substrate are prepared, some diamond solution is pipetted onto the substrate until about 70% of the substrate is covered. At this point, the wafer is spun at 4000 RPM for 45 seconds to evenly distribute diamond particles over the substrate.

Diamond growth is accomplished using microwave-plasma-assisted chemical vapor deposition (MPCVD). Before the growth process, the MPCVD chamber is pumped to a vacuum of less than 20 mTorr absolute pressure. Once the chamber has been evacuated, gas flow is initiated and the pressure in the chamber is maintained at 40 Torr absolute. The main constituent of the growth plasma is H_2, as such H_2 has the highest flow rate of 100 sccm. Once the pressure has stabilized, the MPCVD is started and the output power is slowly increased to 2.3 kW as the temperature increases to about 700 °C. The source of carbon for diamond growth is CH_4 which is next added at a rate of 1.5 sccm. Undoped diamond is allowed to grow for 20 hours to form the structural backing of the probes. In order to improve the probe performance by reducing the conductivity between interconnects, oxygen is added to the growth environment. The addition of .38 sccm of

O_2 to the growth environment increases the resistivity from about ≈10^2-10^3 Ω-cm to ≈10^7 ohm-cm at a cost of reduced the growth rate. O_2 is added to the growth environment for 4 hours. Once the undoped diamond layer is done growing, doped diamond is grown by removing O_2 from the growth environment and adding trimethylboron [$B(CH_3)_3$] (TMB) (diluted in H_2 to .005%) to the growth environment at a rate of 10 sccm. Doped diamond growth continues for about 4 hours. At the end of diamond growth, the flow of CH_4 and TMB is ended and the hydrogen plasma removes the imperfect surface layer for 15 minutes. After the diamond growth process there is a layer of undoped diamond that is approximately 5 μm thick and a layer of doped diamond that is approximately 1 μm thick. The quality of diamond is experimentally verified using Raman spectroscopy to verify the main peak of Raman shift is at 1332 cm^{-1}, as expected.

The next step in the fabrication process is to etch the doped diamond layer to form the electrodes, interconnects, and pads. Diamond is patterned using reactive ion etching (RIE). The RIE process for etching thicker diamond layers requires a metal masking material. The metal that is used is Al as it has a lower etch rate in the specific etch recipe used for etching diamond. Al is patterned using liftoff; PR 9260 is used for the liftoff process because its thickness allows for thick layers of Al to be patterned. After developing the photoresist, the photoresist residue is removed using O_2 plasma in a March Asher with a power of 100 W for 3 minutes. Next the Al is deposited with a thickness of 1 μm using an evaporator. Liftoff is performed in PRS 2000 which is agitated by ultrasound. Once the Al masking layer is prepared, the doped diamond is etched in a Plasmatherm 790 RIE system. The etch process is done at a pressure of 50 mTorr absolute, with 5 sccm CF_4 and 20 sccm Ar. The RF etch power is 300 W. The etching is performed for 75 minutes to ensure that the doped layer is completely etched. The etch rate varies across the sample but is typically in the range of 0.9-1.5 μm/h. The etching is verified by measuring the resistance between interconnects. If the doped diamond layer is completely etched, the resistance between interconnects cannot be measured using a multimeter. Once the etching is done, the Al mask layer is removed using Al etch A. Micrographs of a probe after the first etch step can be seen in Fig. 3-5.

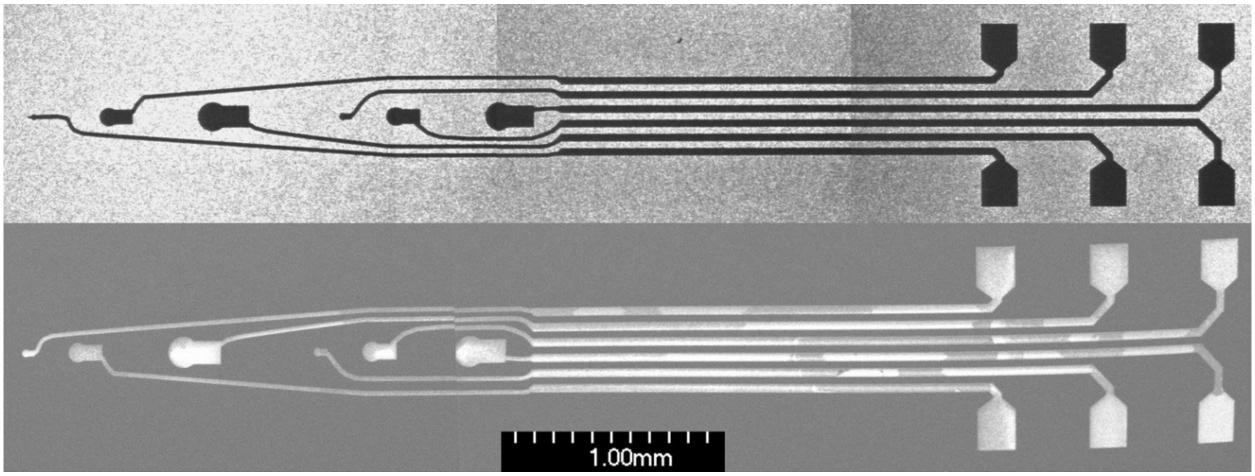

Figure 3-5: Optical micrograph of probe after first etch step (top) and scanning electron micrograph of probe after first etch step (bottom).

The next step in fabrication is growth of undoped diamond to form the top insulating layer. As there is a preexisting diamond layer, seeding for diamond growth is unnecessary. The growth conditions are the same as the previous undoped diamond growth with gas flow rates of 100 sccm, 1.5 sccm, and .38 sccm for H_2, CH_4, and O_2, respectively. Undoped diamond is grown for about 4 hours, resulting in a layer that is approximately 1 μm thick. Micrographs of a probe after the second undoped diamond growth can be seen in Fig. 3-6.

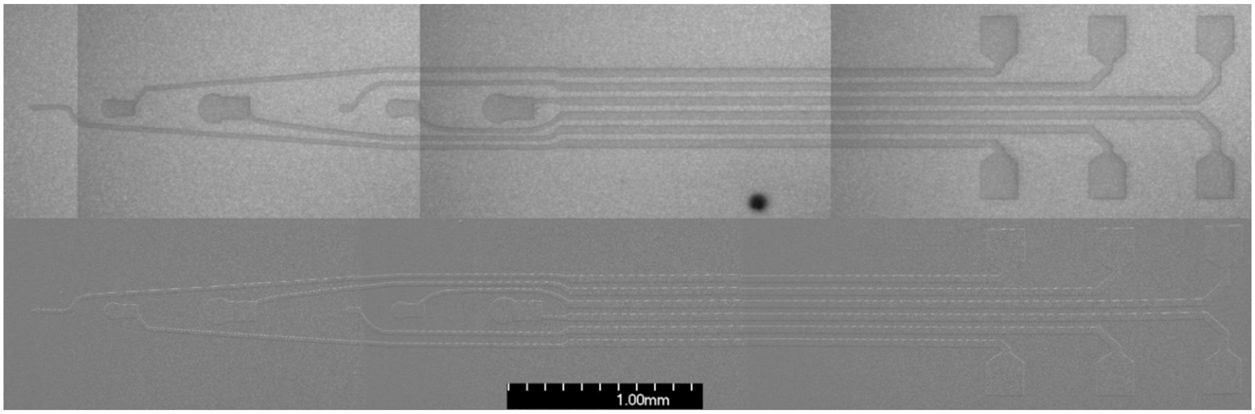

Figure 3-6: Optical micrograph of probe after second growth step (top) and scanning electron micrograph of probe after second growth step (bottom).

Next, the shape of probes is defined by RIE. An Al mask is made using the same process as above, except its thickness is 1.5 μm. The RIE conditions are also the same except the etch time is increased to 4 hours in order to etch through both undoped layers. The CF_4 plasma also aggressively etches the SiO_2 layer underneath the diamond. Knowing this, it can be determined whether etching is complete by measuring the resistance between two points off of the probes. If the diamond is completely etched, as well as the underlying SiO_2, then there will be a low resistance between any two points on the surface of the n-Si wafer. Once complete etching has been verified, the Al mask is removed, again using Al etch A. An optical micrograph of a probe after the probe shape has been defined can be seen in Fig. 3-7.

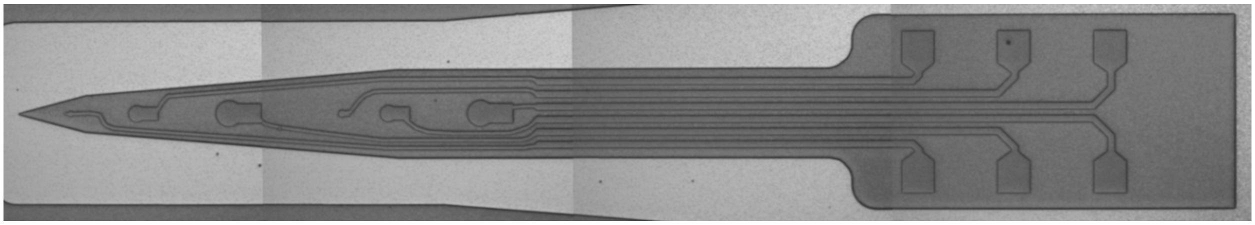

Figure 3-7: Optical micrograph of probe after second etching step.

After patterning the probe shape, the electrodes and pads are exposed by etching the undoped diamond layer above them. For this process, a 1 μm thick Al mask is made using the negative photoresist PR 5214, rather than PR 9260. The RIE recipe remains unchanged and the etch time is 75 minutes. The etch process can be verified by measuring the resistance between an electrode and the pad it's connected to. If the undoped layer is completely removed, there is a low resistance between the pad and electrode. The Al mask is removed by Al etch A. An optical micrograph after this step can be seen in Fig. 3-8.

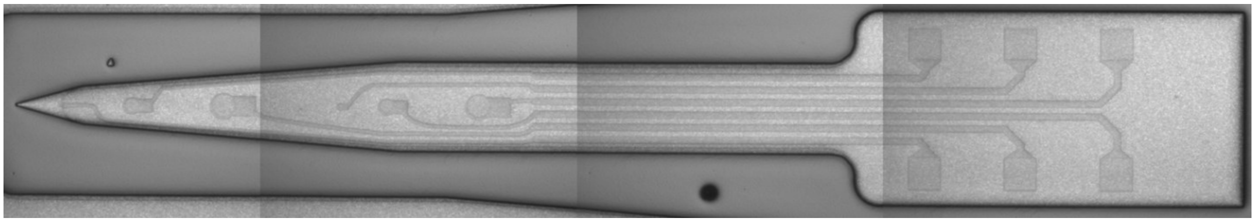

Figure 3-8: Optical micrograph of a probe after exposing the electrodes and pads.

At this point, the single-material diamond probes are entirely made of diamond. The next step in the process is to add the metal pads on the backend for use in wire bonding. The metal pads are made up of two different metal layers. The top metal layer is Au because it is easy to wire bond to and it is resistant to the HF etch that releases the probes. However, Au does not adhere well to diamond, and if only gold is used, the metal pads will peel off of the diamond during the bonding process. To alleviate this problem, and to achieve an ohmic contact between the metal and doped diamond, a layer of Ti or Cr is put underneath the Au. Ti and Cr form a thin layer of TiC and CrC, respectively, which give an ohmic contact and good adhesion to diamond. In this process, Cr is used because it is resistant to etching in HF. The metal layers are patterned using liftoff. The photoresist used is again 9260. The metal layers are deposited by evaporation with thicknesses of 50 nm and 500 nm for Cr and Au. Micrographs of a probe after depositing pads can be seen in Fig. 3-9.

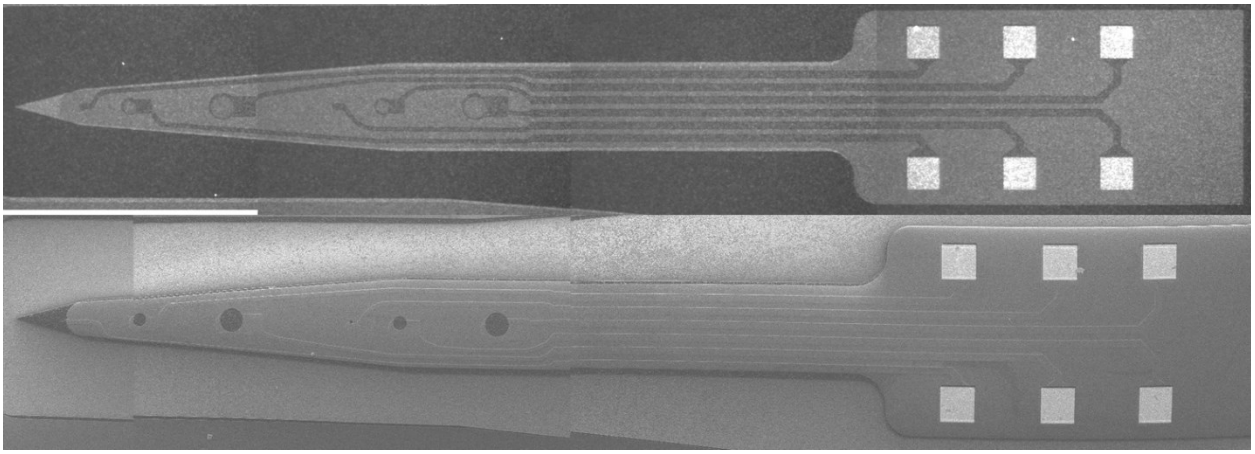

Figure 3-9: Optical micrograph of probe after pad deposition (top). Scanning electron micrograph of probe after pad deposition (bottom).

At this point in fabrication the electrodes can selectively be modified for various applications. For the purpose of electrochemical detection it is of interest to modify the electrodes to be terminated with F, rather than H or O. The reason is because the performance of the diamond as a working electrode in an electrochemical cell improves dramatically, as seen in Fig. 3-10. In the figure, BDD represents a hydrogen-terminated boron-doped-diamond electrode. F-BDD represents a fluorine-terminated boron-doped-diamond electrode. The Pt and Au electrodes are provided as a performance reference. In the figure, a cyclic voltammogram is presented that shows the potential window of several different working electrodes. It is apparent from Fig 3-10 that the potential window of the F-BDD electrode is significantly wider than the BDD electrode (as well as the Au and PT electrodes). This means that an F-BDD working electrode could be used in analytical electrochemistry experiments to detect more analyte types than the other working electrodes. The electrodes on the SMM diamond neural probe can be modified to be fluorine-terminated by exposing them the CF_4 plasma for a short time (< 1 minute). Other modifications of the surface of diamond are possible for other applications, but have not been thoroughly explored.

The final step of single-material diamond probe fabrication is releasing the probes by etching the SiO_2 underneath the probes. The etching of SiO_2 is accomplished using HF. After release the probes are thoroughly rinsed in deionized water for 20 minutes and then dried. An example of a released probe can be seen in Fig. 3-11. The full process flow with detailed steps can be found in Table 3-2.

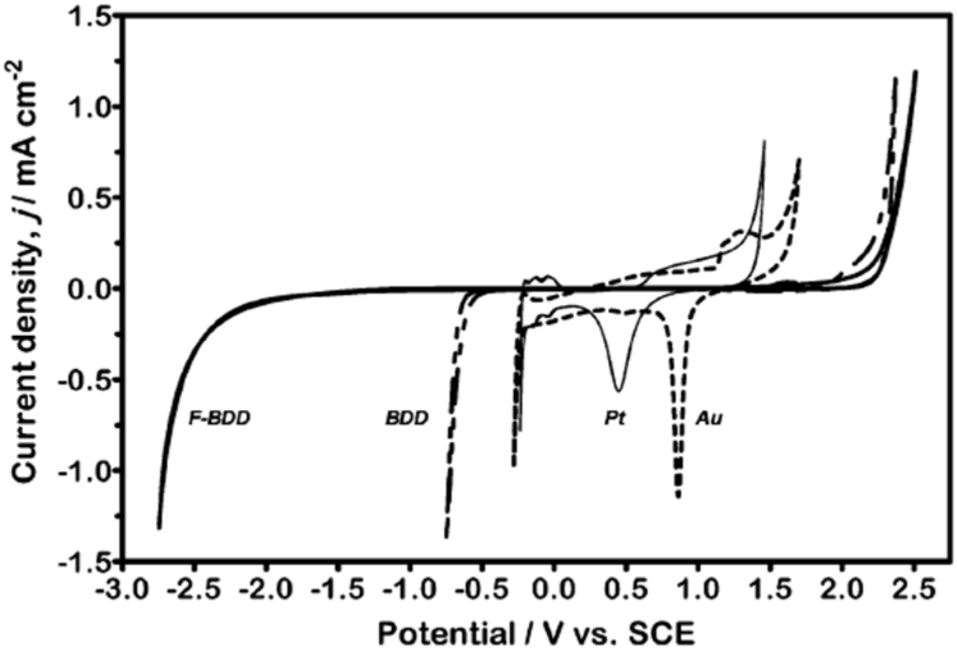

Figure 3-10: Comparison of CV curves using different working electrodes in 1M HClO4, highlighting the improvement of fluorine-terminated diamond over hydrogen-terminated diamond. Scan rate is 0.2 V/s.

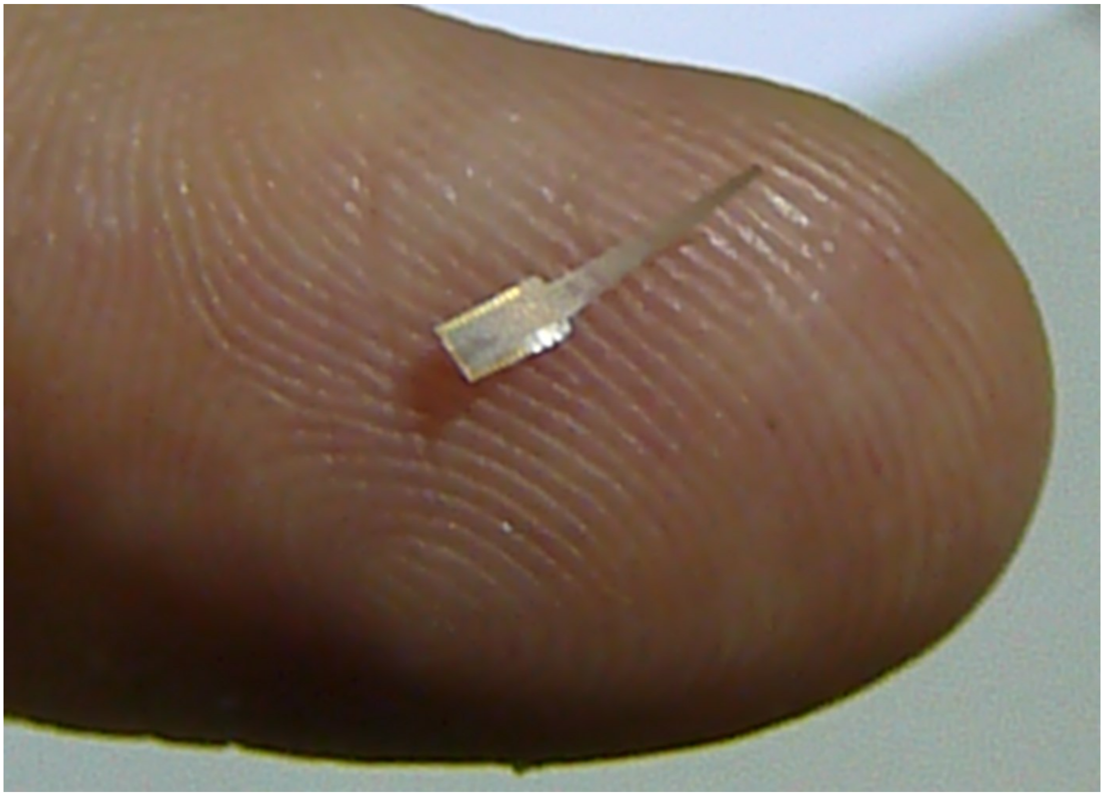

Figure 3-11: Image of a released SMM diamond probe on a fingertip.

Table 3-2: Fabrication process for single-material diamond neural probes.

Process Step		Detail	Equipment	Parameters
Undoped and Doped Diamond Growth	Refresh Oxide Surface	n-Si wafer with 10 µm of SiO2	March Asher	O_2, 100 W, 1 minute
	Diamond Nucleation	5% Diamond powder loaded water	Spinner	4000 RPM for 45 seconds
	Undoped Diamond Growth		MPCVD	H_2:CH_4 (100:1.5 sccm), 2.3 kW, 20 hours, 750 °C
	High-resistivity Undoped Diamond Growth	Undoped Diamond thickness ≈5 µm	MPCVD	H_2:CH_4:O_2 (100:1.5:0.38 sccm), 2.3 kW, 4 hours, 750 °C
	Boron-doped Diamond Growth	Doped Diamond thickness ≈1 µm	MPCVD	H_2:CH_4:TMB (100:1.5:10 sccm), 2.3 kW, 4 hours, 750 °C
Pattern Doped Diamond	Spin 9260	Photoresist thickness ≈6 µm	Spinner	4000 RPM, 30 seconds
	Soft Bake		Hotplate	2.5 minutes, 95 °C
	Expose	Mask 1: Boron-doped Diamond Electrodes and Interconnects	MA6	35 seconds
	Develop Photoresist		Wet Bench	AZ400:H_2O (4:1), 2 minutes
	Ashing		March Asher	O_2, 100 W, 1 minute
	Masking Layer Deposition	Al thickness ≈1 µm	Enerjet Evaporator	Al 10000 Å
	Lift-off		Wet Bench	PRS 2000, 1 hour with ultrasonifcation
	RIE		PlasmaTherm 790	Ar:CF_4 (20:5 sccm), 300 W, 50 mTorr, 75 minutes
	Remove Al Mask		Wet Bench	Al Etchant Type A
Undoped Diamond Growth	High-resistivity Undoped Diamond Growth	Undoped Diamond thickness ≈1 µm	MPCVD	H_2:CH_4:O_2 (100:1.5:0.38 sccm), 2.3 kW, 4 hours, 750 °C

Table 3-2 (cont'd)

Process Step		Detail	Equipment	Parameters
Pattern Undoped Diamond Probe Shape	Spin 9260	Photoresist thickness ≈6 µm	Spinner	4000 RPM, 30 seconds
	Soft Bake		Hotplate	2.5 minutes, 95 °C
	Expose	Mask 2: Undoped Diamond Probe Sheath	MA6	35 seconds
	Develop Photoresist		Wet Bench	AZ400:H_2O (4:1), 2 minutes
	Ashing		March Asher	O_2, 100 W, 1 minute
	Masking Layer Deposition	Al thickness ≈1 µm	Enerjet Evaporator	Al 15000 Å
	Lift-off		Wet Bench	PRS 2000, 1 hour with ultrasonifcation
	RIE		PlasmaTherm 790	Ar:CF_4 (20:5 sccm), 300 W, 50 mTorr, 4 hours
	Remove Al Mask		Wet Bench	Al Etchant Type A
Pattern Undoped Diamond Probe Electrodes and Pads	Spin 5214	Photoresist thickness ≈1.6 µm	Spinner	3000 RPM, 30 seconds
	Soft Bake		Hotplate	1 minute, 95 °C
	Expose	Mask 3: Undoped Diamond Electrodes and Pads	MA6	4 seconds
	Hard Bake		Hotplate	1.5 minutes, 115 °C
	Flood Expose		MA6	1 minute
	Develop Photoresist		Wet Bench	AZ300, 1 minute
	Ashing		March Asher	O_2, 100 W, 1 minute
	Masking Layer Deposition	Al thickness ≈1 µm	Enerjet Evaporator	Al 10000 Å
	Lift-off		Wet Bench	PRS 2000, 1 hour with ultrasonifcation
	RIE		PlasmaTherm 790	Ar:CF_4 (20:5 sccm), 300 W, 50 mTorr, 75 minutes
	Remove Al Mask		Wet Bench	Al Etchant Type A

Table 3-2 (cont'd)

Process Step		Detail	Equipment	Parameters
Pad Deposition	Spin 9260	Photoresist thickness ≈6 μm	Spinner	4000 RPM, 30 seconds
	Soft Bake		Hotplate	2.5 minutes, 95 °C
	Expose	Mask 4: Metal Pads	MA6	35 seconds
	Develop Photoresist		Wet Bench	AZ400:H_2O (4:1), 2 minutes
	Ashing		March Asher	O_2, 100 W, 1 minute
	Metal Deposition		Enerjet Evaporator	Cr/Au 500/5000 Å
	Lift-off		Wet Bench	PRS 2000, 1 hour with ultrasonifcation
Electrode Modification (Optional)	RIE		PlasmaTherm 790	CF_4 20 sccm, 300 W, 50 mTorr, 30 seconds
Probe Release	Probe Release		Wet Bench	HF, 30 minutes
	Probe Cleaning		Wet Bench	DI Water rinse, 20 minutes

In order to effectively use the probes, they must be bonded to a PCB after release. Al wire was used for bonding. After bonding, the wires and backend of the probe are covered in nonconductive epoxy so that the probe can be immersed in liquid during testing or use. This fabrication represents the first SMM neural array ever fabricated. Furthermore it is the first SMM bioMEMS device ever fabricated, and one of the first functional SMM devices ever produced.

3.4 Conclusion

Both diamond neural probes and single-material diamond neural probes have been successfully fabricated. Detailed fabrication processes were discussed for each probe type. Micrographs of the single-material diamond neural probe fabrication process were also shown. Some of the advantages of SMM fabrication are demonstrated as the complexity of probe fabrication is significantly reduced for the SMM diamond neural probe fabrication. While the diamond-based probe fabrication has a 5-page table showing the fabrication detail and requires a minimum of 6 masks, the SMM diamond probe fabrication has a 2.5 page table showing the fabrication details and requires a minimum of 4 masks. This work represents a milestone in SMM development as it was the first SMM microelectrode array, the first SMM bioMEMS device, and one of the first functional SMM devices ever fabricated.

REFERENCES

REFERENCES

[1] H.-Y. Chan, M. Varney, D.M. Aslam K.D. and Wise, “Fabrication and characterization of all-diamond microprobes for electrochemical analysis,” *Proceedings of IEEE Int. Conf. on Nano/Micro Engineered and Molecular Syst.*, pp. 532-535, 2008.

[2] H.-Y. Chan, D.M. Aslam, S.H. Wang, G.M. Swain and K.D. Wise, “Fabrication and testing of a novel all-diamond neural probe for chemical detection and electrical sensing applications,” *Proceedings of IEEE Int. Conf. on Micro Electro Mechanical Systems*, pp. 244-247, 2008.

[3] H.-Y. Chan, D. M. Aslam, J. A. Wiler, and B. & Casey, “A novel diamond microprobe for neuro-chemical and-electrical recording in neural prosthesis,” *Microelectromechanical Systems, Journal of*, vol. 18(3), pp. 511-521, 2009.

[4] H.-Y. Chan, “Polycrystalline CVD Diamond Probes for use in In Vivo and In Vitro Neural Studies,” Ph.D. dissertation, Dept. Elect. Eng., Mich. State Univ., East Lansing, MI, 2008

CHAPTER 4:

Electrochemical Detection Experiments

4.1 Introduction

One property of diamond that is of particular interest for electrochemical applications is its large electrochemical potential window (~4 V). Diamond has been used in many electrochemical detection applications, as can be seen in Table 4-1 [1]. For biomedical applications, diamond has been used to detect neurotransmitters, such as: dopamine [2-4], norepinephrine [2, 5], epinephrine [2], serotonin [6-8], histamine [8], nicotinamide adenine dinucleotide (NADH) [9] and adenosine [10].

Table 4-1. Substances electrochemically detected using diamond electrodes.

Organic Substances	Inorganic Substances
adenosine, ascorbic acid, caffeine, carbamate pesticides, catecholamines, cephalexin, chlorophenols, chlorpromazine, p-cresol, cysteine, dopamine, formaldehyde, flavonoids, glucose, glutathione, guanosine, histamine, indoles, NADH, nitrophenol, nucleic acids, oxalic acid, penicillamine, phenol, polyamines, purine, pyrimidine, serotonin, sulfa drugs, tetracycline antibiotics, theobromine, theophylline, tiopronin and xanthine	azide anion, hydrazine, hydrogen peroxide, iodide, nitrate, nitrite, dissolved oxygen, dissolved ozone, peroxodisulfate, sulfate, sulfide, Ag^+, As(III), Cd^{2+}, Cu^{2+}, Hg^+, Mn^{2+}, Ni^{2+}, Pb^{2+}, Sn^{4+} and Zn^{2+}

Other studies on capillary electrophoresis to detect neurotransmitters using boron-doped-diamond have revealed a detection limit down to 10 nM [2, 3]. Sarada *et al*. [8] explored the electrochemistry of histamine and serotonin with boron-doped diamond using cyclic voltammetry, hydrodynamic voltammetry and low inject analysis. The boron-doped poly-C electrode in histamine had a signal-to-noise ratio (SNR) an order-of-magnitude greater than that of the glassy carbon electrode, a linear dynamic range of 3–4 orders of magnitude and a detection limit of about 1 μM. Comparatively, they found that the detection limit of 5-hydroxytryptamine was about 10 nM.

Rao *et al*. [9] studied nicotinamide adenine dinucleotide (NADH) using boron-doped poly-C. They found a lower detection limit of 10 nM, while maintaining a SNR of at least seven. Furthermore, they were able to distinguish between NADH and ascorbic acid when the concentrations were comparable. Herlambang *et al*. [6] detected neurotransmitters using an overoxidized poly pyrrole-modified, boron-doped-diamond microfiber electrode. They found detection limits of 500 fM for dopamine and 600 fM for serotonin.

Boron-doped diamond is an excellent candidate as a working electrode in an electrochemical cell for chemical detection, as well as having several other notable applications in electrochemistry. As such, electrochemical applications for diamond and single-material microprobes are very promising. Diamond electrodes offer a benefit over other electrode types typically used in neural probe applications. Other probes, such as the silicon-based probe, typically use Au or Pt as a working electrode. Iridium oxide electrodes have also been used as quasi-reference electrodes. As such, the probes with boron-doped diamond electrodes can measure more types of analytes at a higher sensitivity than silicon-based probes. The scope of this work is limited to detection of neurotransmitters. However, diamond microprobes could be useful for many electrochemical applications where electrode placement is critical or electrode spacing resolution is critical.

This work is unique because it is the only electrochemical detection of neurotransmitters that has been performed using a SMM diamond probe with boron-doped-diamond electrodes as a working electrode.

4.2 Results

In order to detect a neurotransmitter using analytical electrochemistry, an electrochemical cell must be established and a test must be performed which can be compared against known standards for different neurotransmitters. The single-material neural probe, or MEA, was used with a commercial Ag/AgCl in 1M KCl reference electrode and a commercial Pt counter electrode. The working electrode was boron-doped diamond. A counter electrode could be added to the single-material probe design, however, an independent reference electrode is required. Diamond (even with different terminations) does not meet the prerequisites for a reference electrode, as it does not have a well-known and stable equilibrium electrode potential independent of electrolytes present in the electrochemical cell. Cyclic voltammetry measurements were performed on the electrochemical cell using a CH Instruments model 750C bipotentiostat.

In an effort to optimize the diamond electrodes for electrochemical detection, some were modified to have a fluorine-terminated surface, rather than the typical oxygen-terminated surface, by being exposed to CF_4 plasma. Cyclic voltammetry was performed on a KCl solution to compare the potential window of the oxygen- and fluorine-terminated diamond working electrodes. It has been found that the potential window of the BDD working-electrode can be altered significantly by modifying the surface of the diamond. Fluorine-terminated diamond has a much greater potential window than oxygen-terminated diamond. As seen in Figure 4-1, the potential window of a fluorine-terminated electrode extends much further on the reduction side of the voltammogram. This is likely due to the extreme hydrophobicity of the fluorine-terminated BDD [11] preventing hydrogen evolution on the surface of the electrode. This means that more analytes could be detected by means of reduction using this electrode.

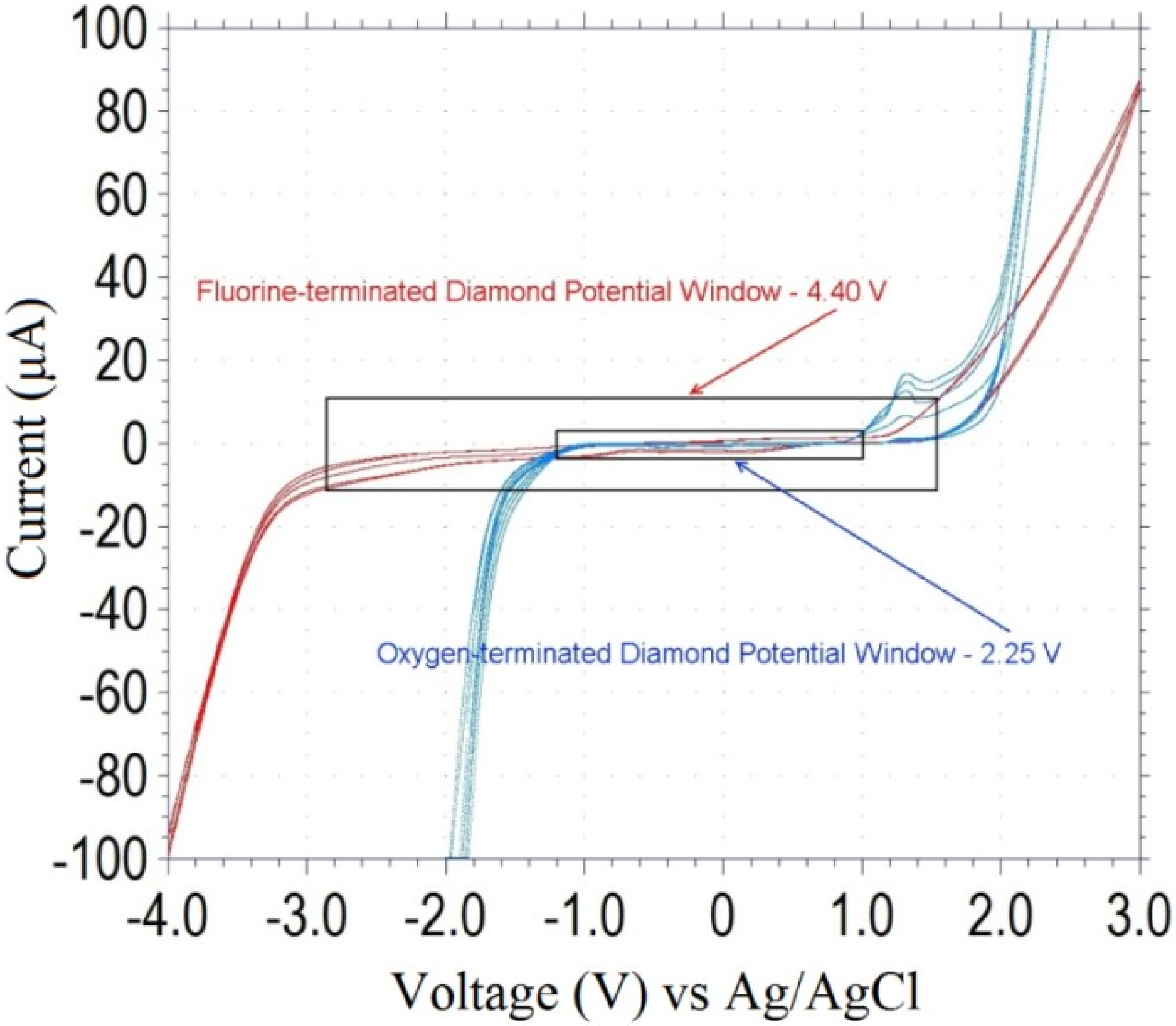

Figure 4-1. Cyclic voltammogram comparing the potential windows of oxygen-terminated diamond and fluorine-terminated diamond in 1 M KCl.

To test repeatability of the electrochemical properties of fabricated probes, several probes were used to perform cyclic voltammetry of 1M KCl solution to determine the potential window of each electrode on each probe. Several electrodes were omitted (6 out of 36 electrodes) from two of the probes because there was no electrical connection to the electrodes (presumably from complications in fabrication or packaging). The results of the other 30 electrodes can be seen in the voltammograms in Fig. 4-2. It can be seen that the potential window of different electrodes and different probes is very repeatable. All of the electrodes have a potential window of ~4.4 V in 1M KCl.

In addition to testing the potential window, the impedance of each electrode was also measured. The impedance spectroscopy was performed using the same bipotentiostat system with the probes immersed in a 1M KCl solution. The measured impedance of each electrode on a single probe can be seen in Fig. 4-3. Measurements from additional probes are very comparable to the probe shown. The impedances are comparable between different electrodes, with the average impedance at 1 kHz being 31.6 kΩ with a standard deviation of 2.8 kΩ.

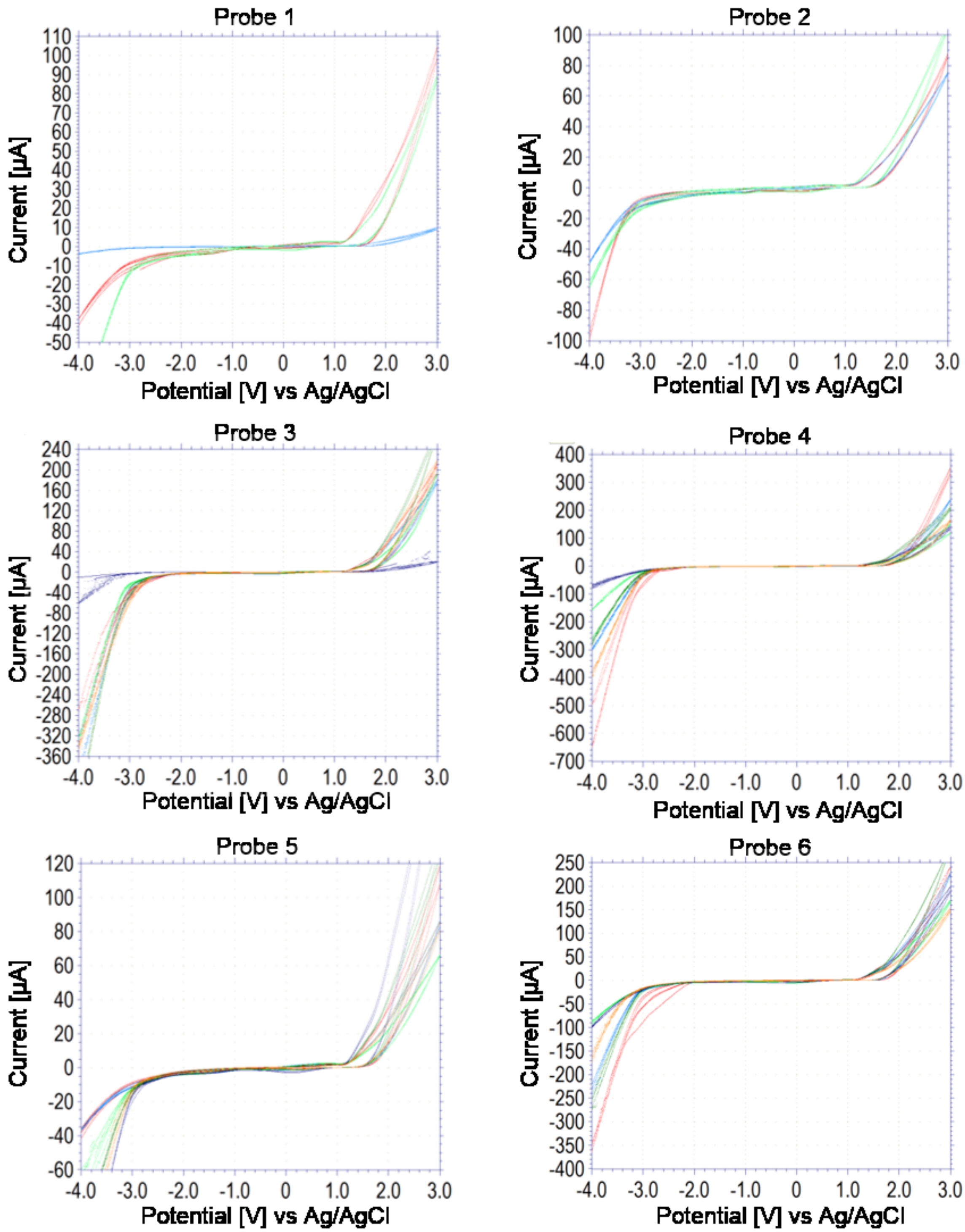

Figure 4-2: Cyclic voltammograms of 1M KCl performed by 30 electrodes on 6 different probes.

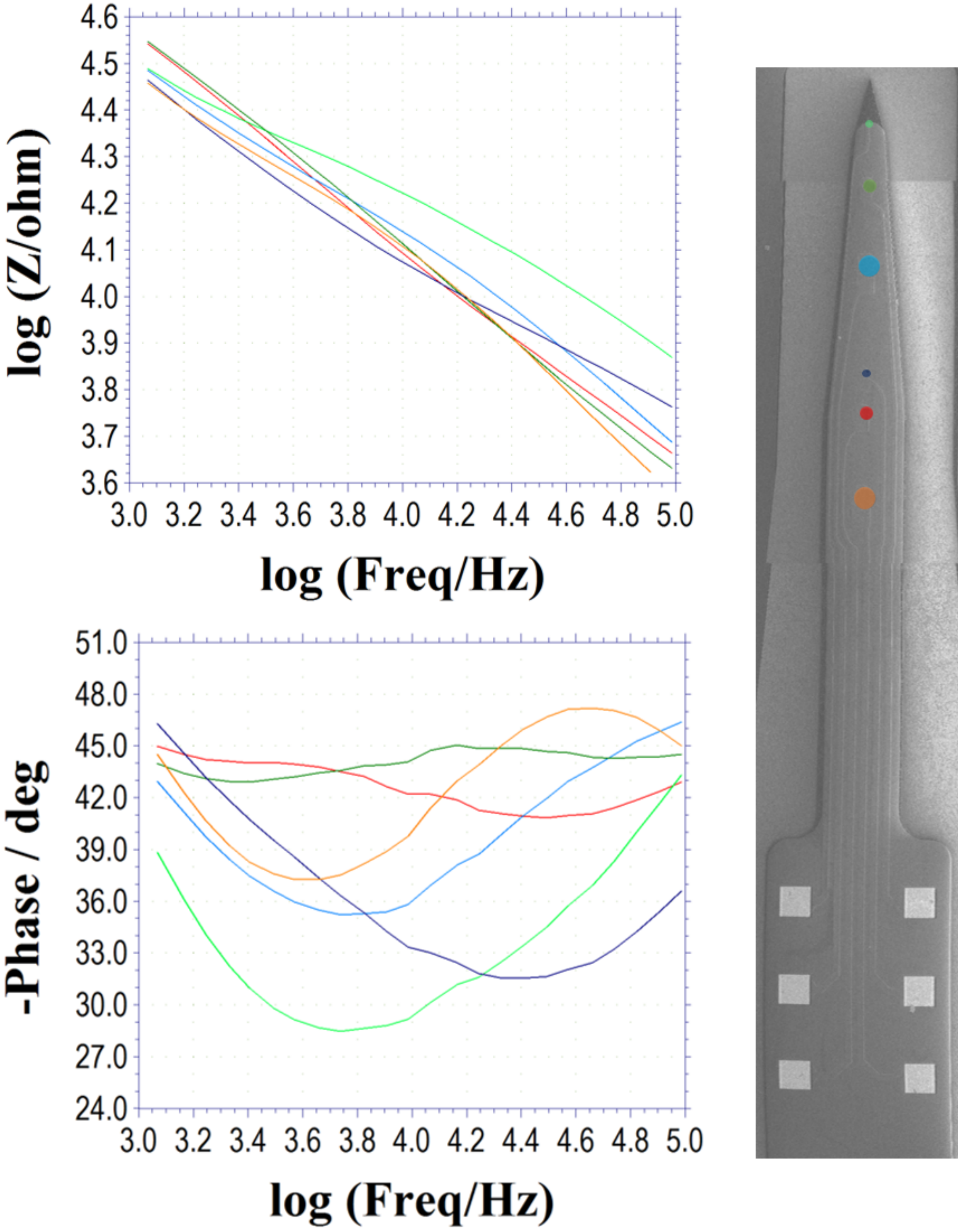

Figure 4-3: Impedance spectroscopy of 6 electrodes on a single single-material probe. Spectroscopy was performed *in vitro*, using a 1M KCl solution. The image on the right acts as a legend, showing which colors correspond to which electrodes on the fabricated probe.

In order to test the detection of neurotransmitters, an experiment was designed to add small amounts of norepinephrine to Krebs solution and then perform cyclic voltammetry. The experiment was performed using electrodes from a diamond probe as the working electrode, a commercially available Pt counter electrode, and a commercially available Ag/AgCl reference electrode. The measured current in the experiment was then compared to the current from a cyclic voltammogram of pure Krebs solution. In the voltammograms in Fig. 4-4 the change in current from adding norepinephrine to a pure Krebs solution can be seen. The inset shows the cyclic voltammograms before subtracting the background current. The figure shows that there is a clear difference between 1 nM, 5 nM and 15 nM concentrations of norepinephrine, indicating a quantification limit in the 5 nM range. This detection limit is consistent with other results using diamond as a working electrode [2, 3, 8, 9]. This detection limit should be sufficient for *in vivo* biomedical applications as typical neurotransmitter levels are several orders of magnitude larger in the mM range [12]. The figure also demonstrates an extremely low background current, a major advantage of the diamond electrode. Performing this cyclic voltammetry with other fabricated diamond probes has comparable results. The cyclic voltammetry method was chosen to test the electrochemical probe because it is easy to interpret and is applicable to testing for small concentrations of analytes. This method could potentially be used to detect other analytes with the same probe. Peaks will be detected at different voltages on the CV curve which can be used to identify several analytes and their concentrations so long as the redox voltages are distinct. It is likely that some *a priori* knowledge of the biological system would be required to isolate several neurotransmitter concentrations. Similar diamond probes have been used to detect many types of analytes including several neurotransmitters, as described in Section 4.1 of this dissertation.

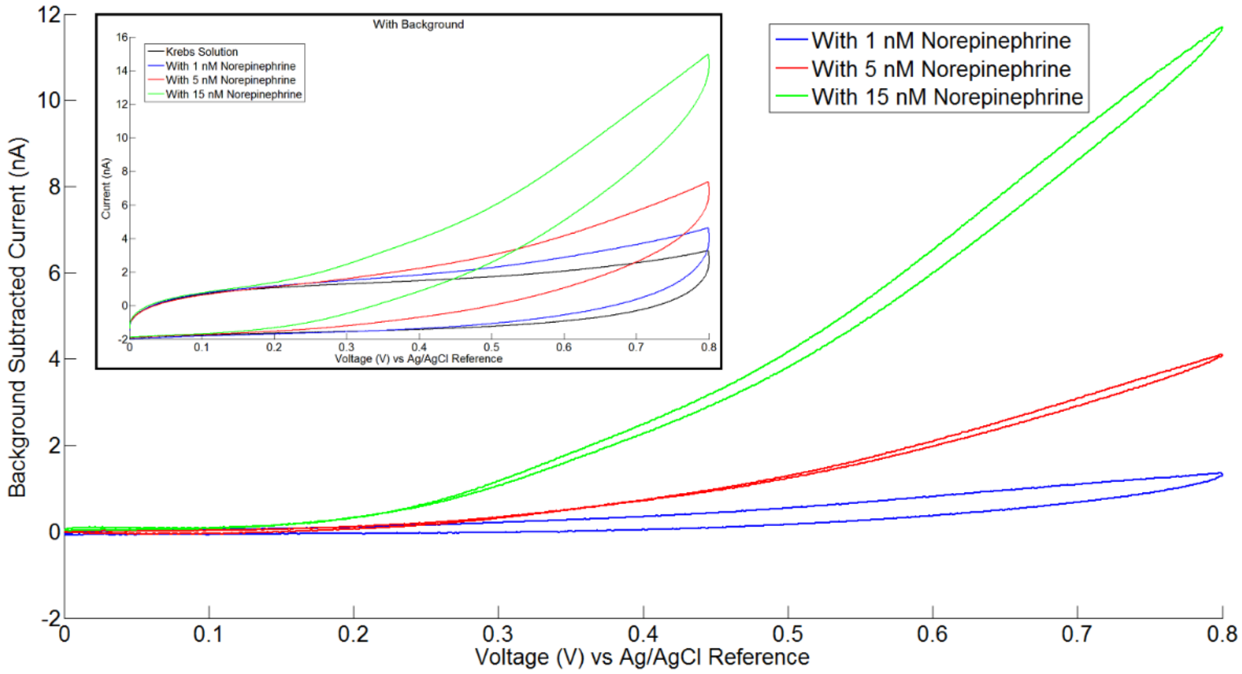

Figure 4-4: Family of background-subtracted cyclic voltammograms of krebs solution with varying amounts of norepinephrine (NE), demonstrating a lower detection limit of 5 nM or less. The inset shows the cyclic voltammograms before subtracting the krebs solution background.

4.3 Conclusion

It has been demonstrated that diamond probes can be used for some electrochemical applications. The potential window of the fluorine-terminated boron-doped-diamond electrodes is ~4.4 V in 1M KCl and is very repeatable between different electrodes and probes. The impedance of the electrodes is also repeatable and the average impedance at 1 KHz is ~30 KΩ. The diamond working electrodes have been used, *in vitro*, to quantify the detection limit of the neurotransmitter norepinephrine in Krebs solution. It appears that diamond microprobes (or similar devices) may be of use in electrochemical detection applications where controlled electrode size and spacing are critical.

REFERENCES

REFERENCES

[1] A. Kraft, “Doped diamond: A compact review on a new, versatile electrode material,” *Int. J. Electrochem. Sci.*, *2*, pp. 355-385, 2007.

[2] D. Shin, B.V. Sarada, D.A. Tryk, and A. Fujishima, “Application of diamond microelectrodes for end-column electrochemical detection in capillary,” *Anal. Chem.*, vol. *75*, pp. 530-534, 2003.

[3] J. Cvacka, V. Quaiserova, J. Park, Y. Show, A. Muck, and G.M. Swain, “Boron-doped diamond microelectrodes for use in capillary electrophoresis with electrochemical detection,” *Anal. Chem.*, vol. *75*, pp. 2678-2687, 2003.

[4] P.S. Siew, K.P. Loh, W.C. Poh, and H. Zhang, “Biosensing properties of nanocrystalline diamond film grown on polycrystalline diamond electrodes,” *Diamond Relat. Mater.,* vol. *14*, pp. 426-431, 2004.

[5] J. Park, V.Q. Mocko, K. Peckova, J.J. Galligan, G.D. Fink, and G.M. Swain, “Fabrication, characterization, and application of a diamond microelectrode for electrochemical measurement of nore-pinephrine release from the sympathetic nervous system,” *Diamond Relat. Mater.,* vol. *15*, pp. 761-772, 2006.

[6] O. Herlambang, B.V. Sarada, and T.N. Rao, “Miniturization of diamond microsensor system for *in vivo* detection,” *Chem. Sens. B,* vol. *18*, pp. 121-123, 2002.

[7] J.M. Halpern, S. Xie, G.P. Sutton, B.T. Higashikubo, C.A. Chetek, H. Lu, H.J. Chiel, and H.B. Martin, “Diamond electrodes for neurodynamic studies in Aplysia californica,” *Diamond Relat. Mater.,* vol. *15*, pp. 183-187, 2006.

[8] B.V. Sarada, T.N. Rao, D.A. Tryk, A. Fujishima, “Electrochemical oxidation of histamine and serotonin at highly boron-doped diamond electrodes,” *Anal. Chem.*, vol. *72*, pp. 1632-1638, 2002.

[9] T.N. Rao, I. Yagi, T. Miwa, D.A. Tryk, A. Fujishima, “Electrochemical oxidation of NADH at highly boron-doped diamond electrode,” *Anal. Chem.*, vol. *71*, pp. 2506-2511, 1999.

[10] S. Xie, G. Shafer, C.G. Wilson, and H.B. Martin, “*In vitro* adenosine detection with a diamond-based sensor,” *Diamond Relat. Mater., vol. 15*, pp. 225-228, 2006.

[11] G. Sine, L. Ouattara, M. Panizza, and Ch Comninellis, "Electrochemical behavior of fluorinated boron-doped diamond," *Electrochemical and solid-state letters* 6, no. 9, D9-D11, 2003.

[12] A. Scimemi and M. Beato, “Determining the neurotransmitter concentration profile at active synapses,” *Molecular neurobiology*, vol. 40, no. 3, pp. 289-306, 2009.

CHAPTER 5:

Electrical Neural Recording Experiments

5.1 Introduction

Single-material neural probes were designed for *in-vivo* electrical recording of neural signals. As such, the ultimate test of their efficacy is being used to record neural activity. In order to validate the recordings, the results must match the expected results of an experiment. Two neural recording experiments were performed on a pigmented guinea pig (*Cavia porcellus*) at the Kresge Hearing Research Institute at the University of Michigan. The animal use procedures were approved by the University of Michigan. For one experiment, data was recorded from silicon probes, diamond probes, and single-material diamond probes, and each can be compared. For the other recording experiment, only single-material diamond probes were used. In this analysis, only a basic threshold method will be used to detect action potentials. The detection was performed by the recording equipment, a Plexon Neural Data Acquisition System, while the experiment was performed. These analyses represent the capability of single-material diamond probes using traditional recording and detection methods. Neural recordings have been previously performed using diamond probes, but this work is the first time that single-material diamond probes have been used.

5.2 *In-Vivo* Neural Recording

In order to test the SMM neural probe, the probe was surgically implanted into a live guinea pig's auditory cortex. This marked the first implantation of a SMM device into a living animal. Before the experiment, the guinea pig was anesthetized and a bolt was affixed to the skull of the animal to hold the skull (and brain) in place (Fig. 5-1). Once the animal was restrained, a partial craniotomy was performed above the right auditory cortex. A ground wire was attached to the pericranium far from the implantation site. A speaker was placed in the animal's left ear (corresponding to the right auditory cortex). Finally the packaged neural probe was inserted through the dura matter into the auditory cortex (Fig. 5-2).

Figure 5-1: Anesthetized guinea pig with bolt affixed to skull.

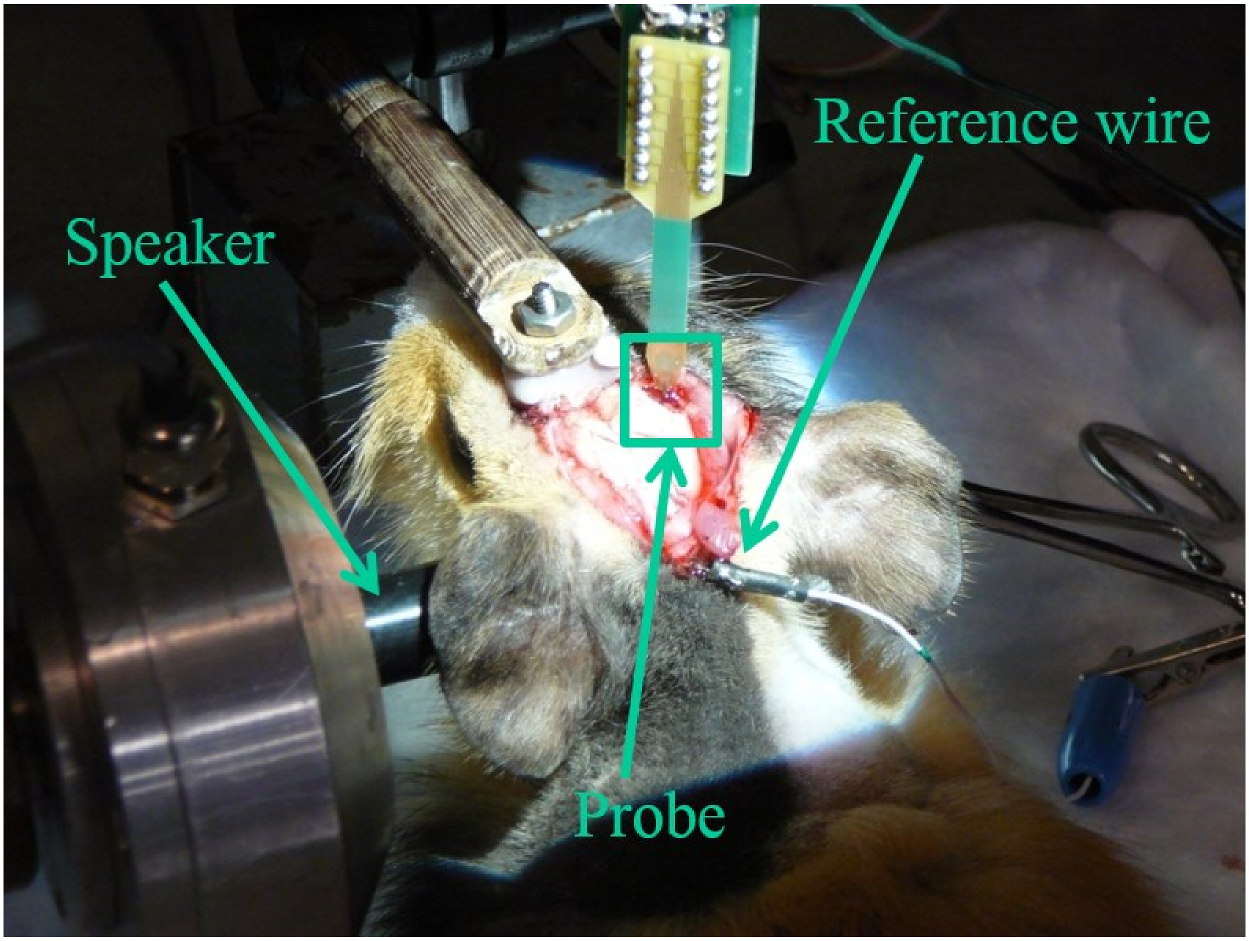

Figure 5-2: Anesthetized guinea pig with neural probe inserted in right audio cortex and speaker placed at left ear.

In the experiment, the anesthetized guinea pig was subjected to 200 ms, wide-frequency audio-pulses at a frequency of 2 Hz. During the experiment, the electrical activity at all electrodes was recorded. In addition, the recording equipment also detected action potentials using a threshold technique. Fig. 5-3 shows a close-up example of an electrical signal recorded from a single-material diamond probe. For the purpose of comparison, Fig. 5-4 shows a similar recording from a diamond neural probe and Fig. 5-5 shows a recording from a silicon-based neural probe. Recordings from all electrodes on each probe type can be seen in Fig. 5-6, Fig. 5-7, and Fig. 5-8.

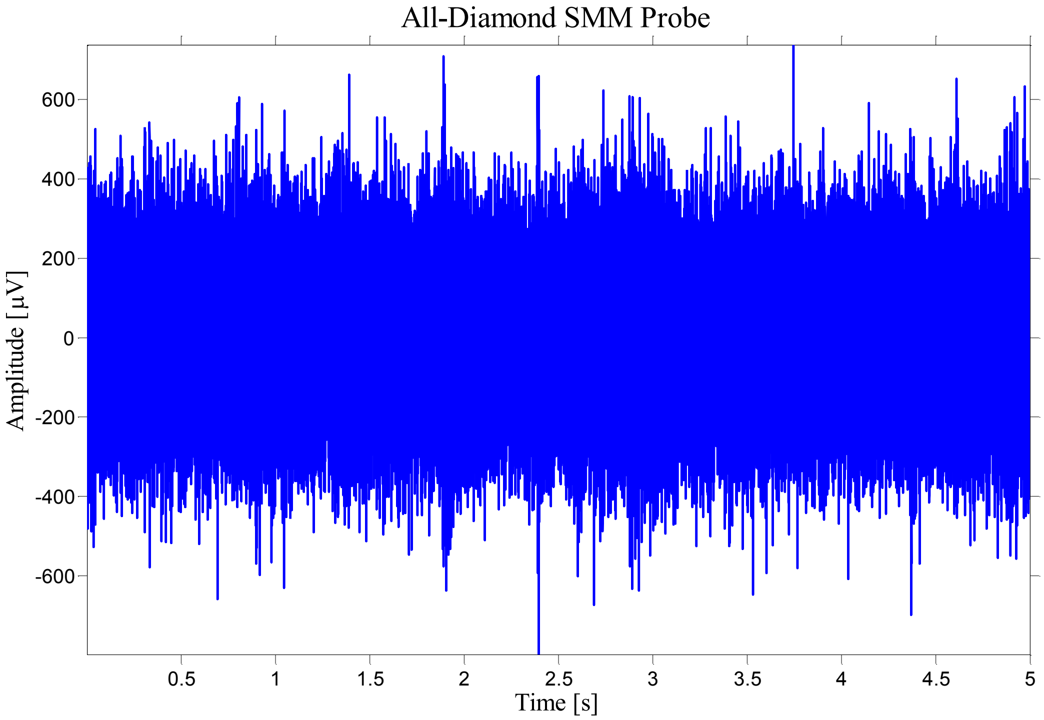

Figure 5-3: Neural recording from the audio cortex of a guinea pig taken with a single-material diamond neural probe with boron-doped-diamond Electrode.

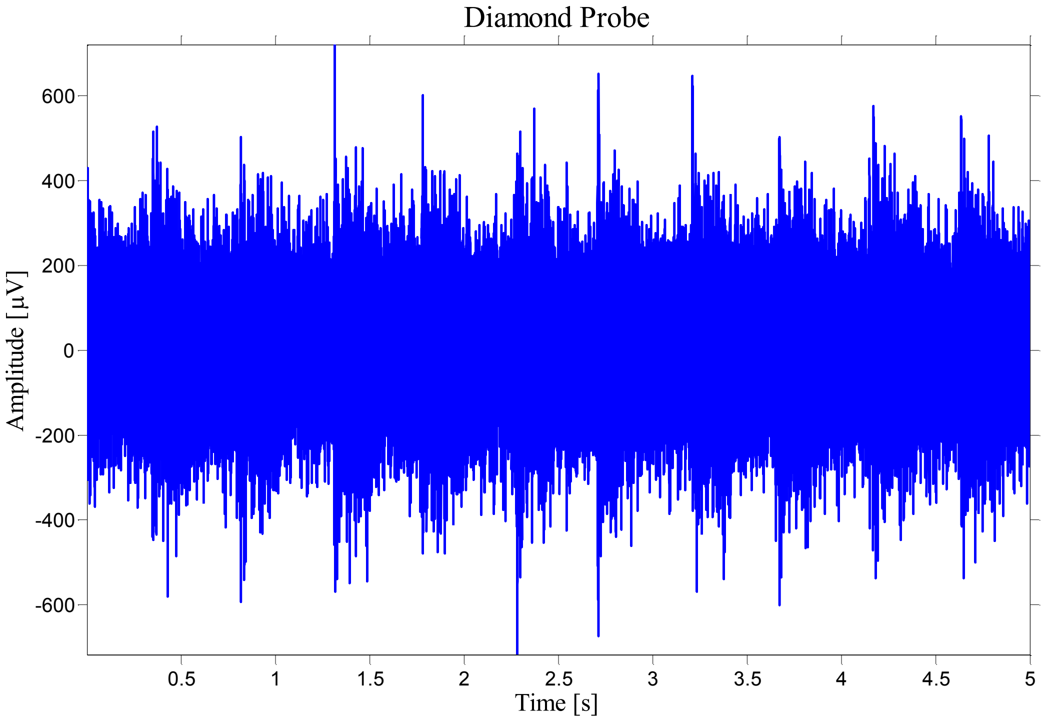

Figure 5-4: Neural recording from the audio cortex of a guinea pig taken with a diamond-based neural probe with a boron-doped-diamond electrode.

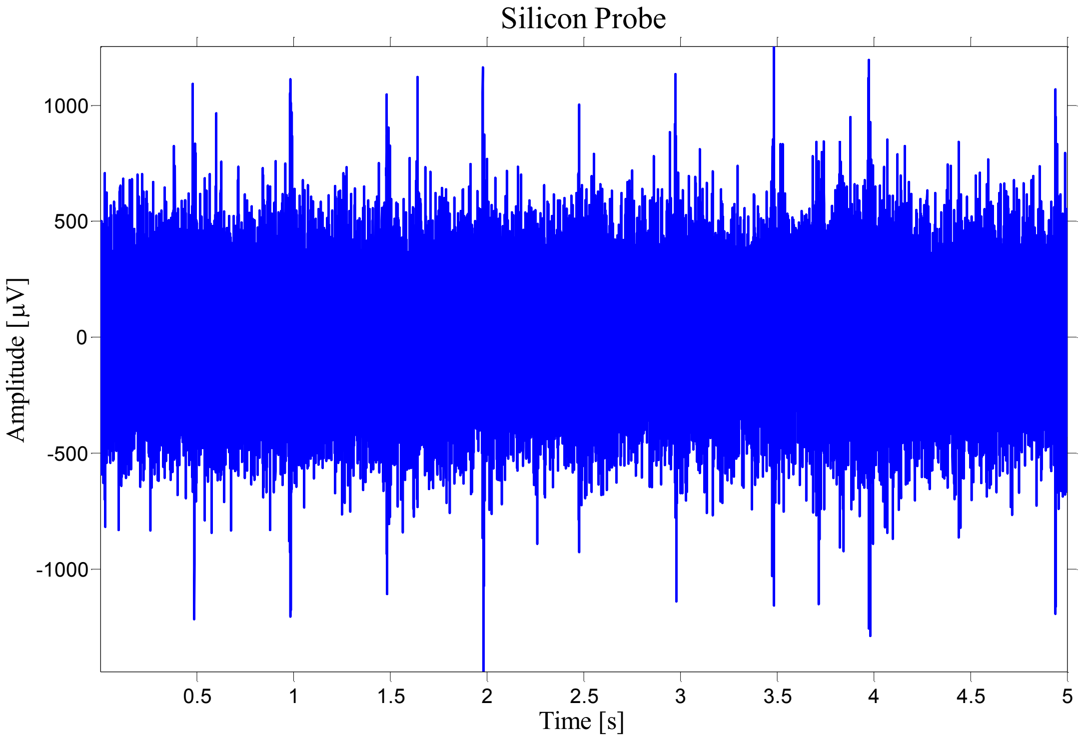

Figure 5-5: Neural recording from the audio cortex of a guinea pig taken with a silicon-based neural probe with an iridium oxide electrode.

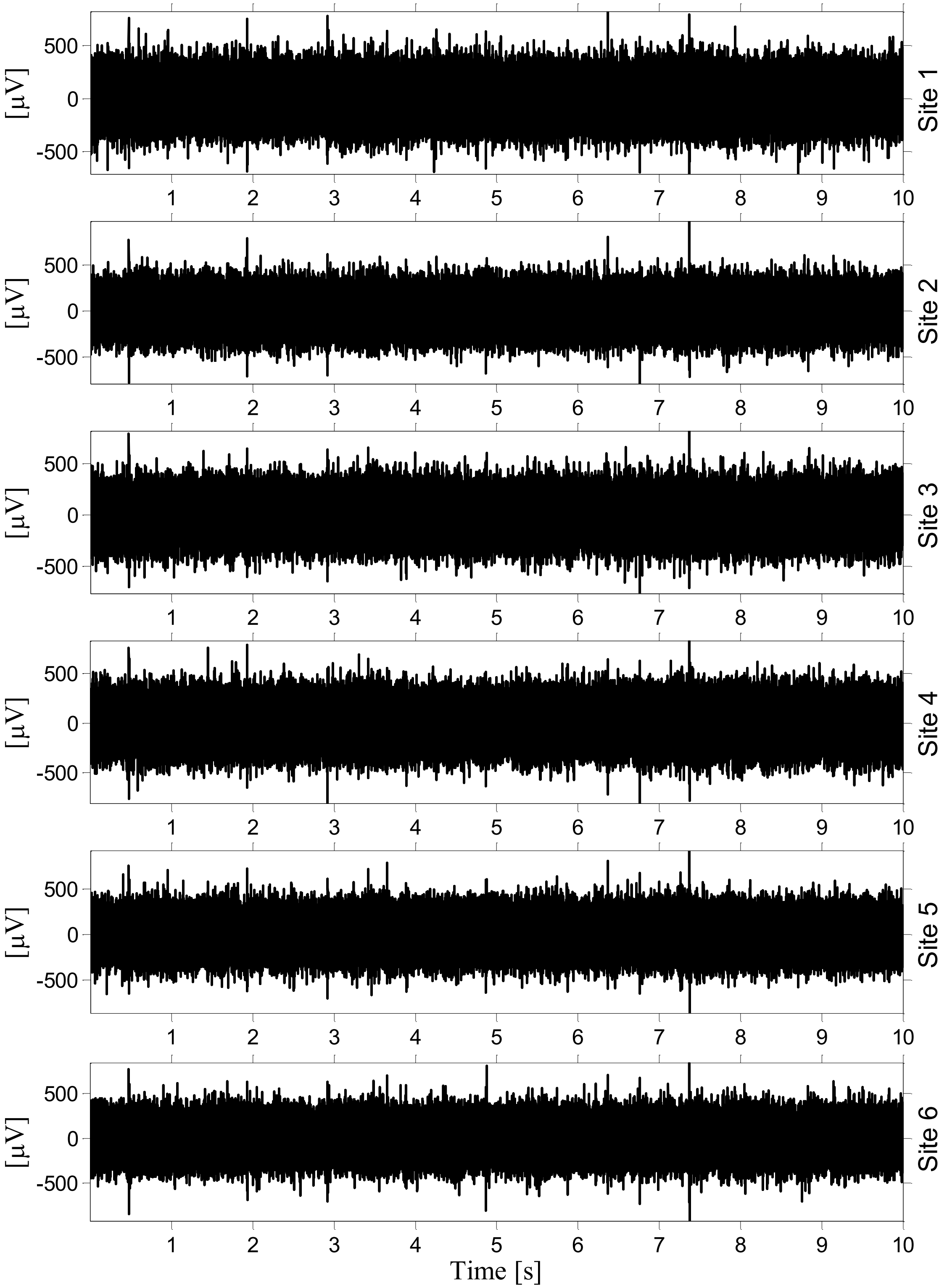

Figure 5-6: Electrical neural recordings from the audio cortex of a guinea pig taken with a single-material diamond neural probe with boron-doped-diamond electrodes.

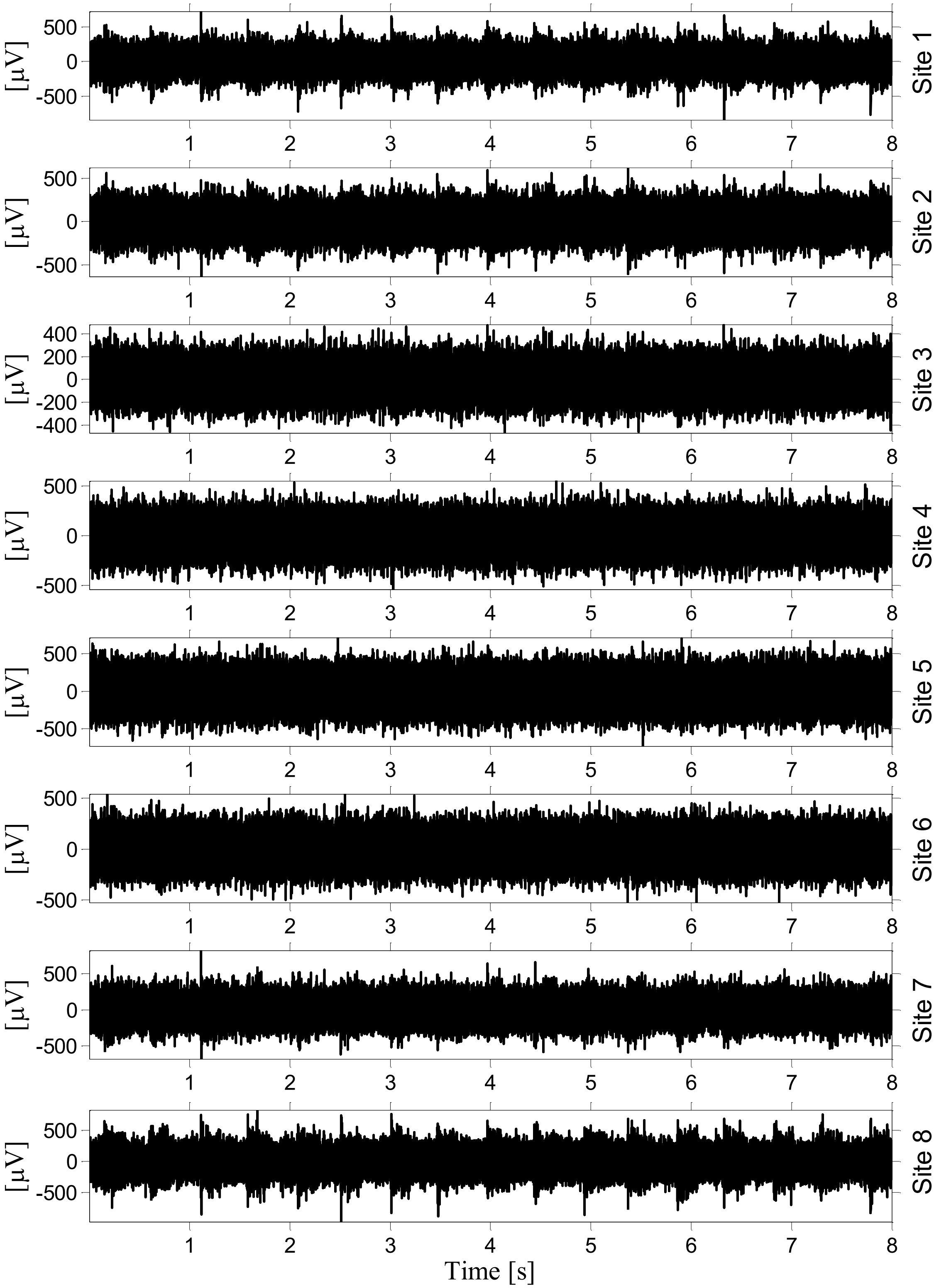

Figure 5-7: Electrical neural recordings from the audio cortex of a guinea pig taken with a diamond-based neural probe with boron-doped-diamond electrodes.

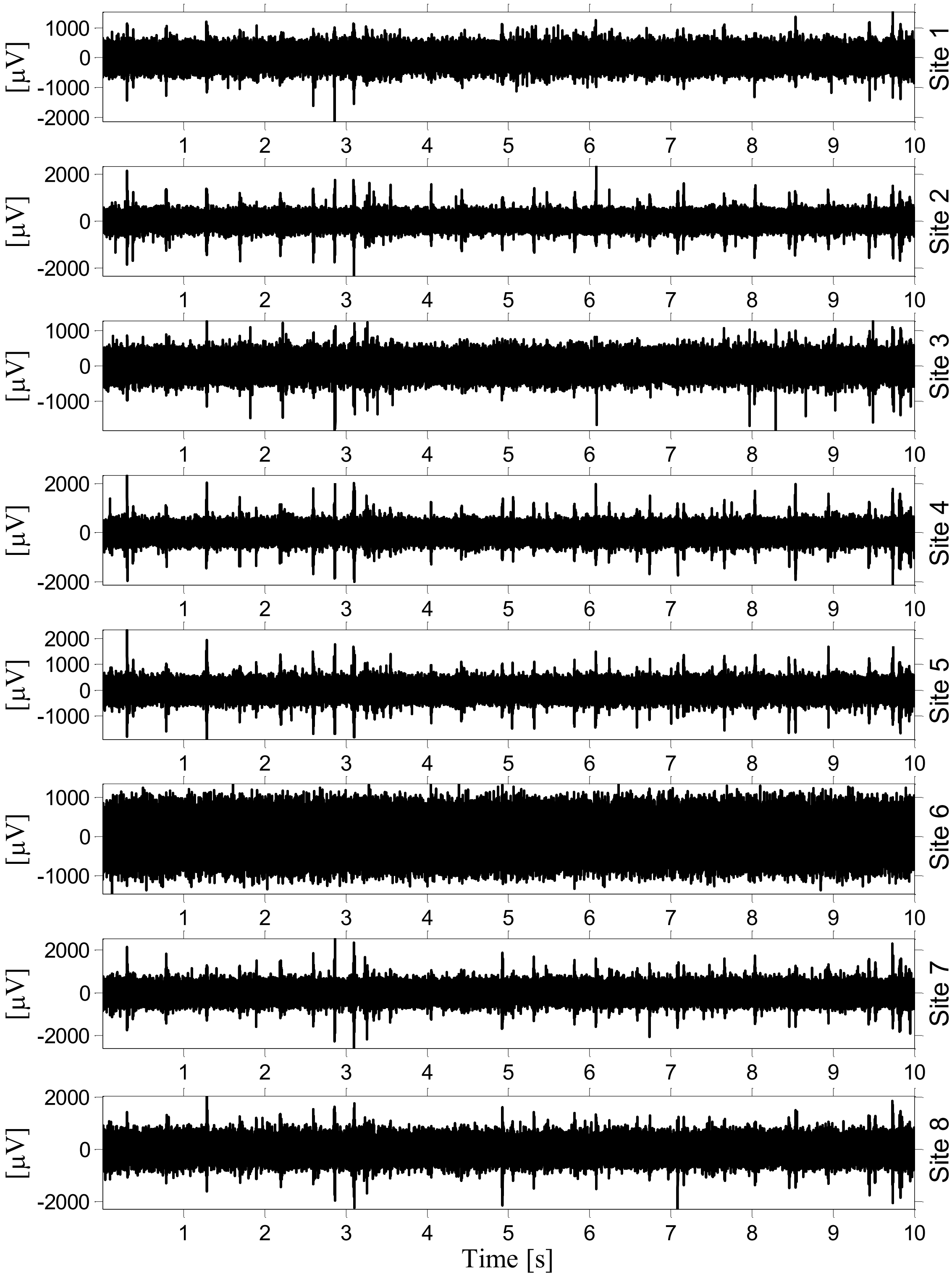

Figure 5-8: Electrical neural recordings taken from the audio cortex of a guinea pig with a silicon-based neural probe with iridium oxide electrodes. Electrodes 1 – 8.

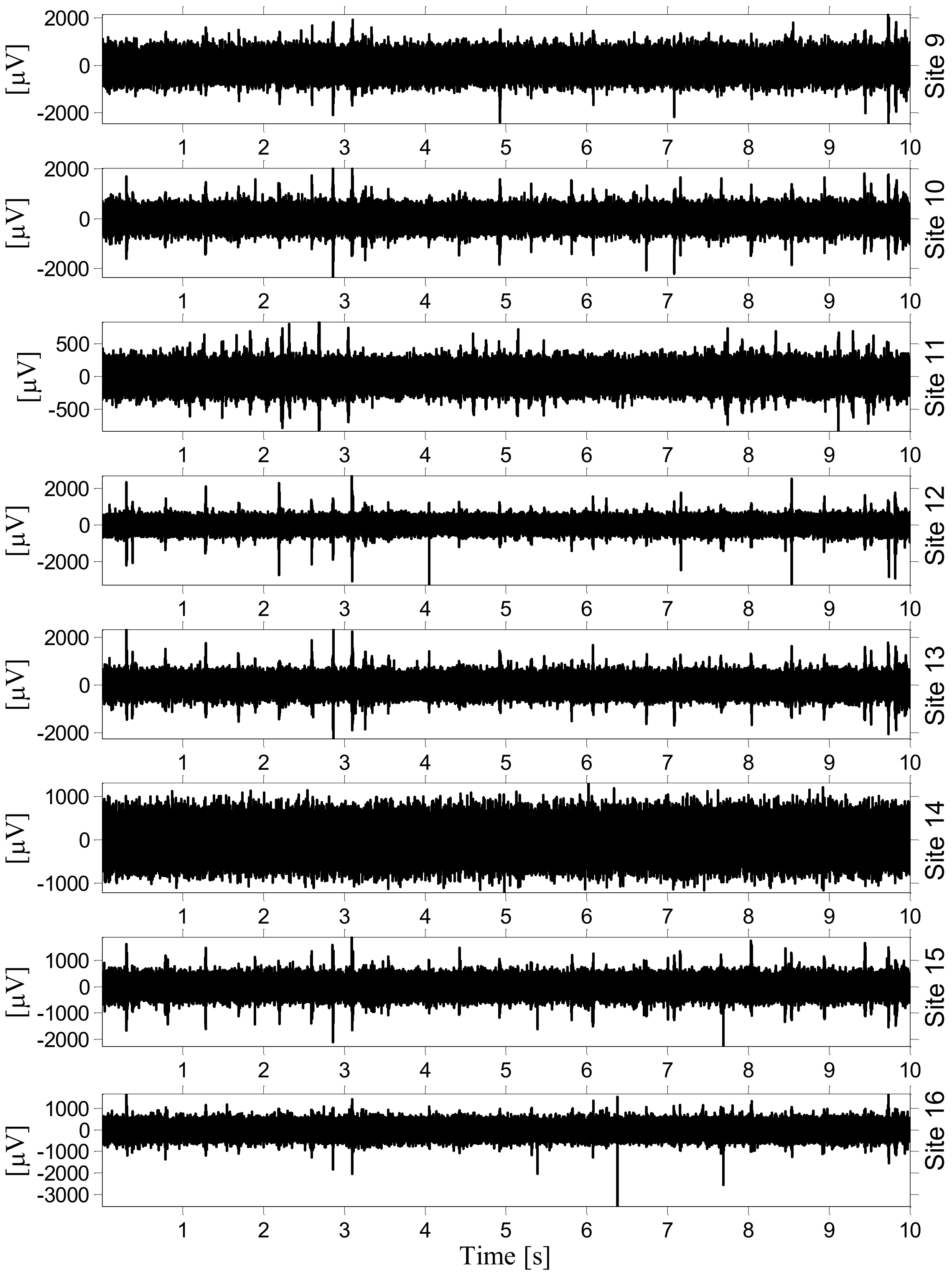

Figure 5-9: Electrical neural recordings taken from the audio cortex of a guinea pig with a silicon-based neural probe with iridium oxide electrodes. Electrodes 9 – 16.

The recordings show peak values every 500 ms, corresponding to the frequency of the applied stimulus. However, the recorded signals from the diamond probes and the single-material diamond probes appear to have a lower SNR than what is often presented for silicon-based neural probes with other electrode materials. Low SNR could be due to a myriad of reasons, such as: a large distance between the neurons and electrodes (probe placement), inappropriately sized electrodes (diameter was 30 μm), high impedance per unit area of the electrode (electrode impedance of ~30 kΩ at 1 kHz), or poor insulation between recording sites (>1 MΩ). The SNR issue can be alleviated through signal processing. The SMM neural probes have an SNR which is comparable to other diamond electrodes (e.g., Figs. 5-4 and 5-7), but slightly worse. The slightly poorer SNR can be accounted for by the lower conductivity of doped diamond, as compared to metals typically used for probe interconnects. Further work has been done in signal processing to detect action potentials in these relatively noisy recordings.

A second recording experiment was performed where the stimulus was a range of different single-frequency tones. The neuron firing rate at each electrode site was recorded for each tone. Tones ranged from 1,000 Hz to 30,000 Hz and were played in a random order. The amplitude of the audio stimulus was also randomized between 37.7 and 87.7 dB SPL. The experiment was repeated 30 times. The results of the experiment can be seen in Fig. 5-10. Fig. 5-10 shows the sum of detected action potentials versus audio frequency for all 30 iterations. The expected result of this experiment is that certain electrode sites should be sensitive to certain frequencies because the neurons being recorded have higher firing rates with those audio frequencies [1-3]. However, the action potential detection algorithm was a simple thresholding technique (window discriminator) that was inadequate to accurately detect action potentials due to the poor SNR of the recordings. The result is that there is little correlation between detected firing rate and applied audio stimulus. The activity was higher for lower frequency stimuli for all recording sites. There is no discernable difference between recording sites.

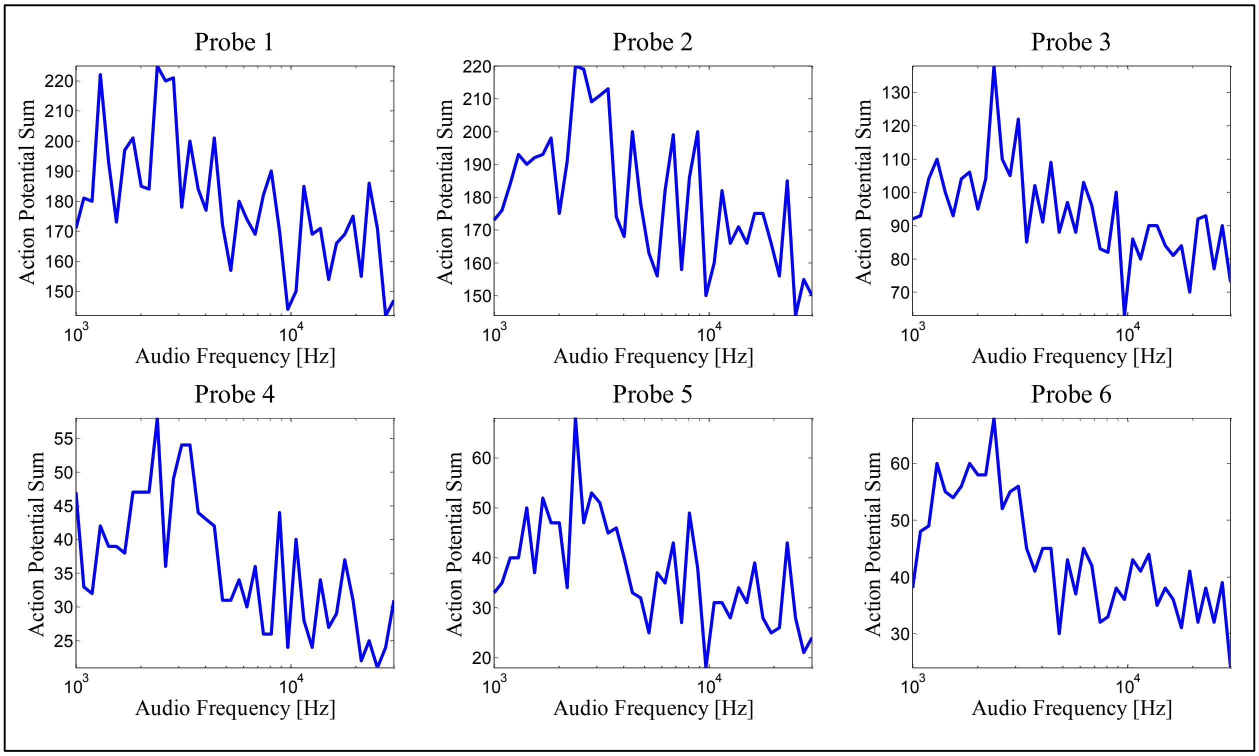

Figure 5-10: Detected action potentials versus frequency of applied audio stimulus.

5.3 Analysis of Neural Recordings using Threshold Detection Method

In the initial recording experiment, a six-electrode SMM probe was implanted into the auditory cortex of a guinea pig. During the experiment, a wide-band audio stimulus was played through a speaker placed at the ear of the guinea pig. The stimulus lasted 200 ms and was applied every 500 ms. During the experiment, the electrical activity at all 6 electrodes was recorded. In addition, the recording equipment also detected action potentials using a threshold technique. Action potentials were detected if the recorded signal went above or below user-set thresholds.

The expected result from this experiment is to see a correlation between the application of stimuli and the firing rate of neurons. Specifically, as stimulus is applied, the firing rate is expected to increase, especially at the onset of stimulus. It is expected to see a large number of action potentials within the first 50 ms of stimulus, and few during the period where no stimulus is applied. It is known that specific neurons are often tuned to certain frequencies, and entire regions of the auditory cortex can be mapped to tuned frequencies, a technique known as tonotopy [1-3]. However, the stimuli in this experiment are wide band stimuli, so all neurons should be sensitive to the stimuli. In order to determine how many action potentials were detected during the stimuli and at the beginning of stimuli, the action potential detection times were compared with the times that stimuli started. For every action potential detected, the time after the onset of stimulus was recorded, a number between 0 and 500 ms. In order to visualize this information, the action potential times were plotted as a histogram, with 25 ms bins. These results can be seen in Fig. 5-11 for each of the 6 electrodes for the single-material diamond neural probe.

Fig. 5-12 has histograms for the diamond-based neural probe. Fig. 5-13 and Fig. 5-14 have the histograms from the silicon-based neural probe. In the figures, stimulus was applied from 0 to 200 ms.

For the single-material diamond neural probes, it is apparent that the number of action potentials occurring near the onset of stimulus (first 50 ms) is much higher than the rest of the recording. These results are consistent with the expected result; there is a sharp increase in firing rate at the onset of stimulus. For the diamond-based neural probes, there is an increase of firing rate during the stimulus in most of the recordings. Several electrodes (4, 5, and 6) show little correlation to the stimulus and fewer detected spikes. It is presumed that either these electrodes were not near neurons or (more likely) there was a poor connection due to complications in fabrication or packaging. The silicon-based neural probes show a sharp increase in firing rate at the onset of stimulus and an increased firing rate through the duration of the stimulus. Again, several electrodes appear to have poor connections (electrodes 6, 11, and 14). These results all coincide with the expected results of the experiment which suggest that all 3 probes may be viable for use in neural recording experiments. However, the poor signal-to-noise ratio of the single-material diamond and diamond-based neural probes may cause some action potentials to be missed and a more thorough detection algorithm may be prudent.

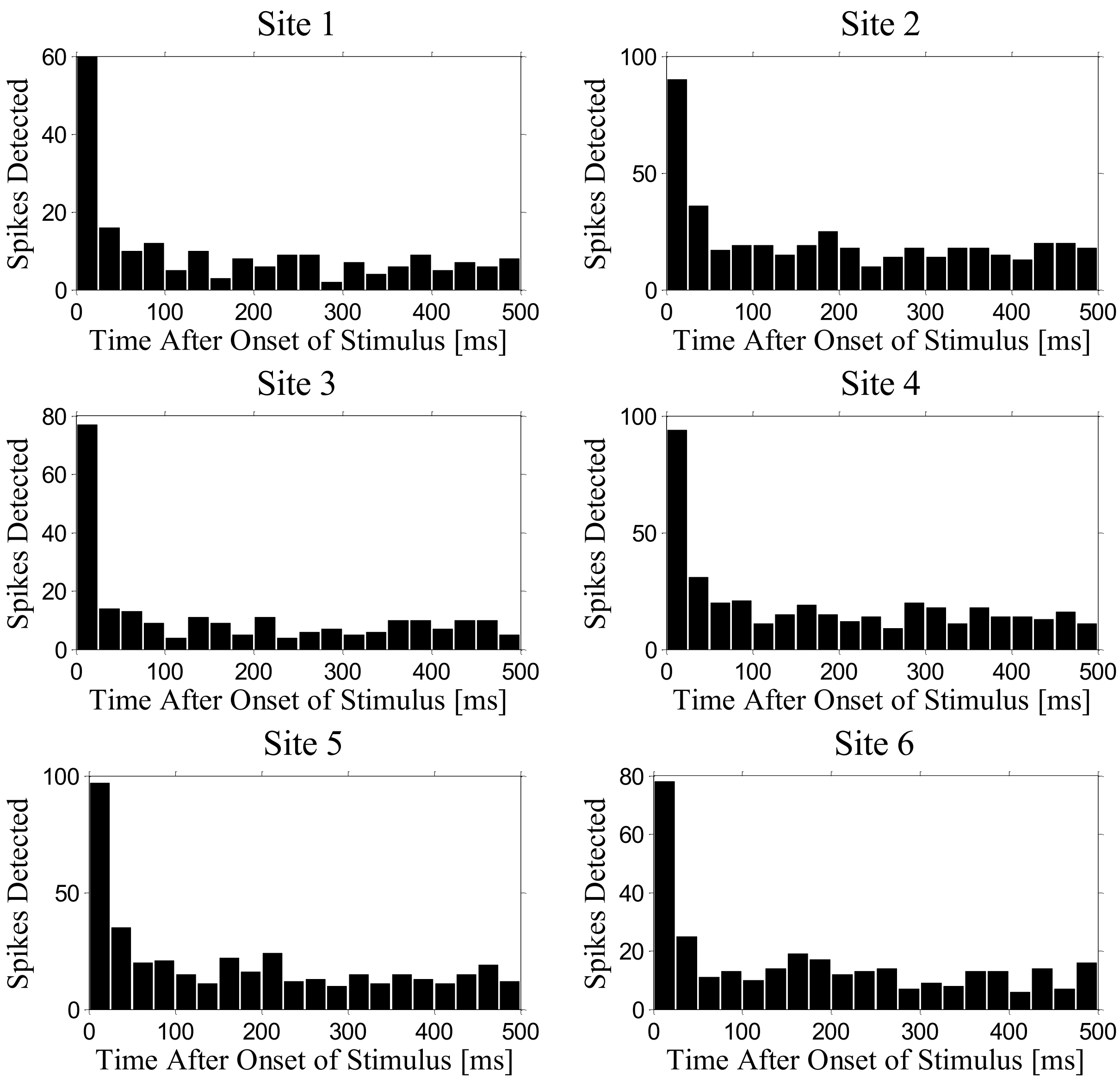

Figure 5-11: Histograms showing detected action potential times relative to the onset of stimulus for a diamond SMM probe with boron-doped diamond electrodes.

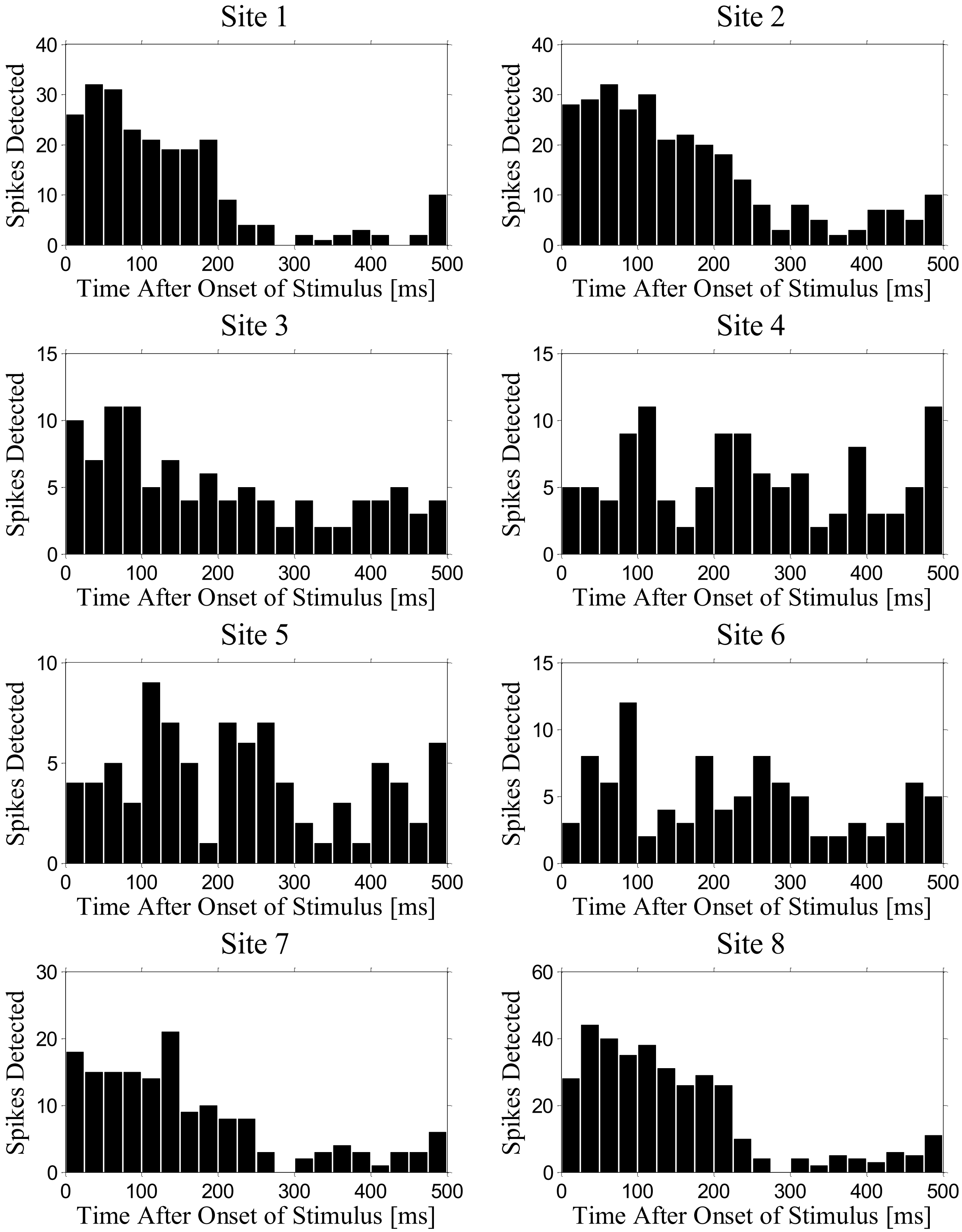

Figure 5-12: Histograms showing detected action potential times relative to the onset of stimulus for a diamond-based neural probe with boron-doped-diamond electrodes.

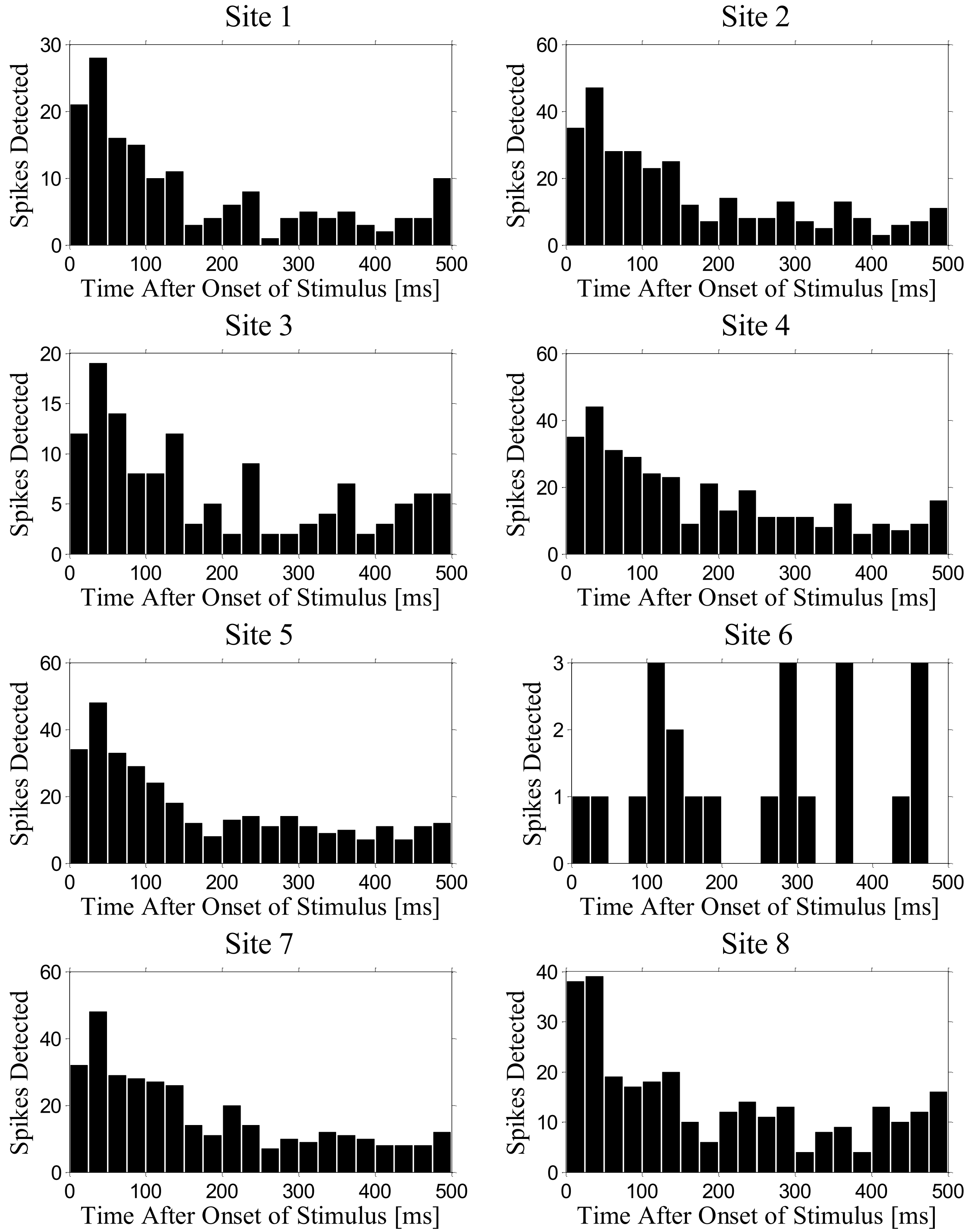

Figure 5-13: Histograms showing detected action potential times relative to the onset of stimulus for a silicon-based neural probe with iridium oxide electrodes. Electrodes 1 – 8.

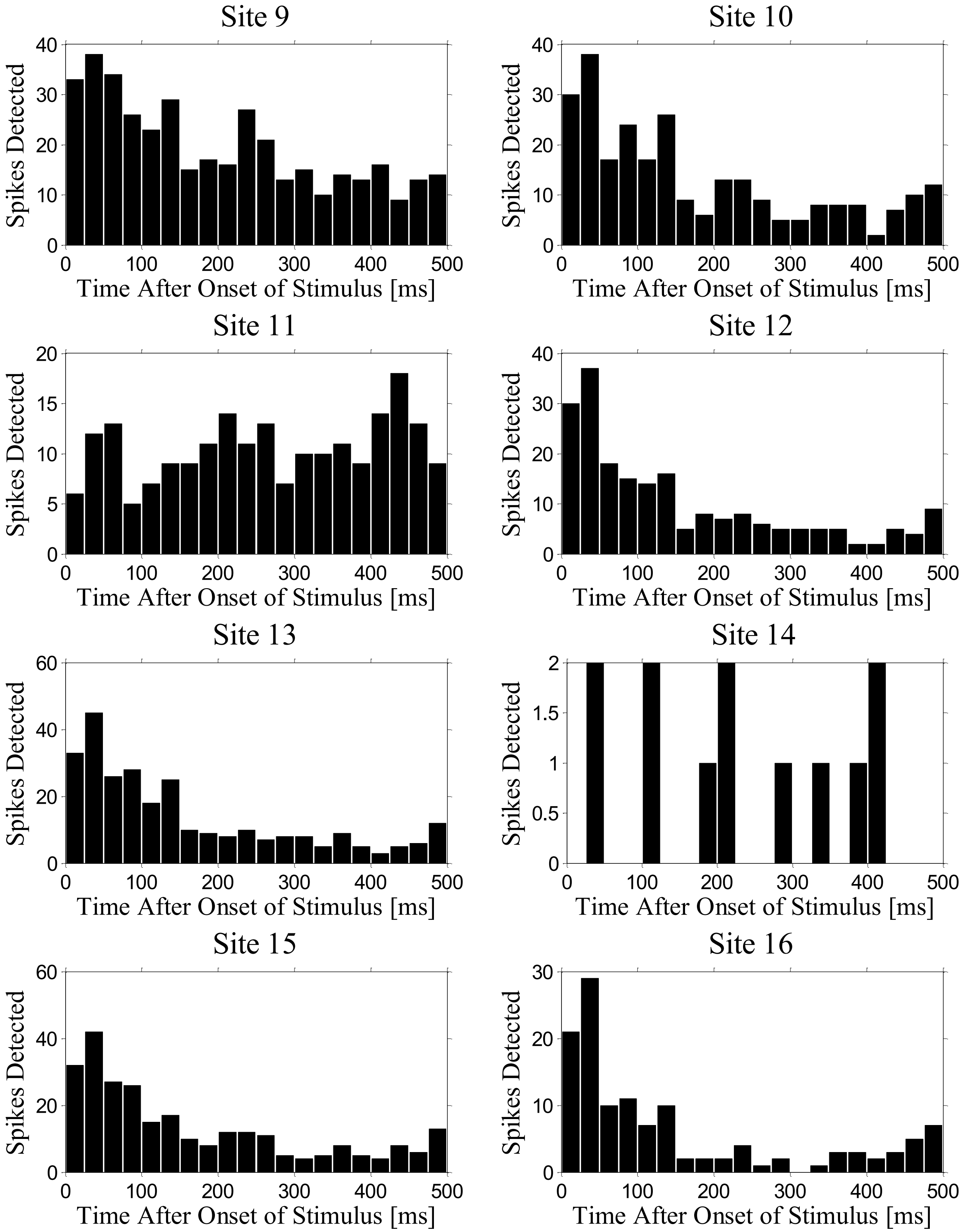

Figure 5-14: Histograms showing detected action potential times relative to the onset of stimulus for a silicon-based neural probe with iridium oxide electrodes. Electrodes 9 – 16.

The second recording experiment also came from the auditory cortex of a guinea pig. In this experiment, however, different frequency stimuli were applied rather than wide-band audio stimuli. Detected action potentials were recorded for each electrode. The expectation is that the firing rate should increase for certain audio frequencies as neurons are often tuned to certain audio frequencies. Furthermore, different electrodes should be sensitive to different audio ranges.

In order to determine the firing rate for different frequencies, the number of action potentials detected for a particular frequency are summed across the 30 repetitions of the experiment. The stimulus time for a particular frequency was also summed from all 30 repetitions. The firing rate was calculated by dividing the total number of detected action potentials for a given frequency by the total amount of time the frequency was applied. In addition, the average firing rate when no stimulus was applied was calculated in a similar fashion. The average firing rate versus applied stimulus frequency can be seen in Fig. 5-15. The hashed horizontal line represents the average firing rate with no stimulus applied and can be considered the background measurement. The results show an increase in neural activity when the stimulus is applied. The firing rate is consistently higher during stimulus than when no stimulus is applied. However, the firing rate does not appear to be frequency dependent. For all electrodes, the firing rate seems to be slightly higher for lower frequencies. For example, on electrode 6 there seems to be a peak at about 2 kHz with a firing rate of about 7.5 Hz, whereas the average firing rate about 4 kHz seems to be about 4.5 Hz. While there appears to be some correlation between frequency and firing rate, it does not appear to be significant. As such the experimental results are inconsistent with the expected results. This is likely due to poor SNR of the original recording and the simple thresholding method used to detect action potentials.

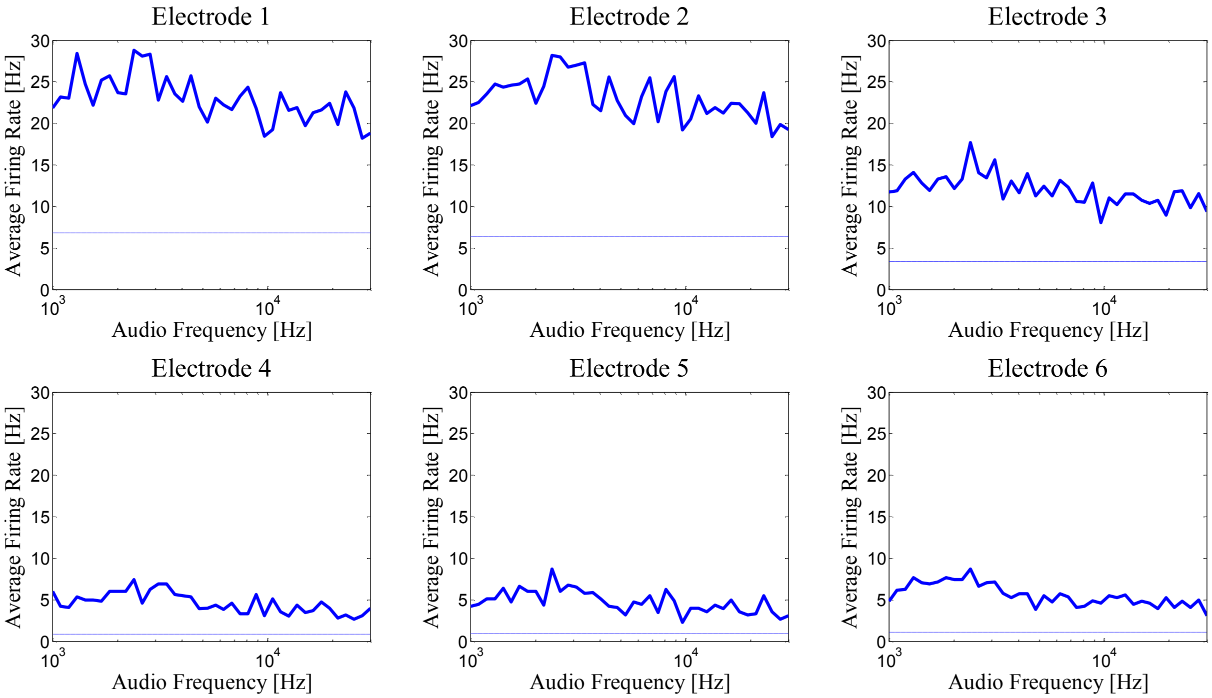

Figure 5-15: Average firing rate versus frequency of applied audio stimulus for a single-material diamond neural probe. The hashed line represents the background average firing rate when no stimulus was applied.

5.4 Conclusion

Single-material diamond, diamond-based, and silicon-based neural probes have been surgically implanted into the audio cortex of a guinea pig for *in-vivo* electrical recording. This is the first time that a single-material neural probe has been tested *in vivo* and the first time that a single-material MEMS device was tested *in vivo*. A wide-band audio stimulus was applied to the ear of the guinea pig, and the resulting neural activity was recorded with each type of probe. As expected, each type of probe showed a rise in neural firing rate during the stimulus, while the single-material diamond and silicon-based neural probes showed a significant rise at the onset of stimulus. This demonstrates that the single-material diamond probe can successfully record action potentials *in vivo*. A second experiment was performed with the single-material diamond neural probes where the frequency response of the neurons was tested. There was an increase in firing rate during the stimuli. However, there was not an appreciable frequency dependency for any of the recording sites.

REFERENCES

REFERENCES

[1] F.C. Hellweg, R. Kock, and M. Volrath, “Representation of the cochlea in the neocortex of guinea pigs,” *Exp. Brain Res.*, vol. 29, pp.467–474, 1977.

[2] H. Redies, U. Sieben, and O.D. Creutzfeldt, “Functional subdivisions in the auditory cortex of the guinea pig,” *J. Comp. Neurol.*, vol. 282, pp. 473–488, 1989.

[3] J. G. Arenberg, S. Furukawa, and J.C. Middlebrooks, “Auditory cortical images of tones and noise bands,” *Journal of the Association for Research in Otolaryngology*, vol. 1, no. 2, pp. 183-194, 2000.

CHAPTER: 6

Action Potential Detection in Low Signal-to-Noise Applications

6.1 Introduction

Recordings of electrical signals from neurons are critical in developing brain-machine interfaces and neuroprosthetics, studying neural disorders, or researching other neuroscience applications. Unfortunately, these recordings are typically buried within noise signals, as can be seen in the real neural recordings in Fig. 6-1. In an ideal experiment, electrodes can be positioned near neurons and a very high signal-to-noise ratio (SNR) can be achieved. However in most real experiments, complications arise negatively impacting SNR. In chronic implantations, this can be due to movement of the electrode or biofouling of the electrode. This can result in significant degradation of SNR that can cause traditional action potential detection methods (thresholding [1]) to be ineffective. Biofouling can affect recording action potentials more than just affecting the amplitude of the spike. The layer of protein that adheres to the electrode surface adds not only a resistive component to the impedance of the electrode (lowering the detected voltage), but also a capacitive component which affects the spectral composition of the action potential. This can affect the performance of band-pass filtering as a method of reducing noise, as the range of frequencies of interest can change during chronic implantation. There are additional reasons why electrode arrays could have poor SNR, including poor electrode placement (it is improbable that every electrode in an array would be ideally placed), sparsely located neurons, electrode material, or tissue damage during surgical implantation. To compensate for the low SNR inherent in neural recordings, many techniques have been developed to attempt to detect action potentials from noisy signals.

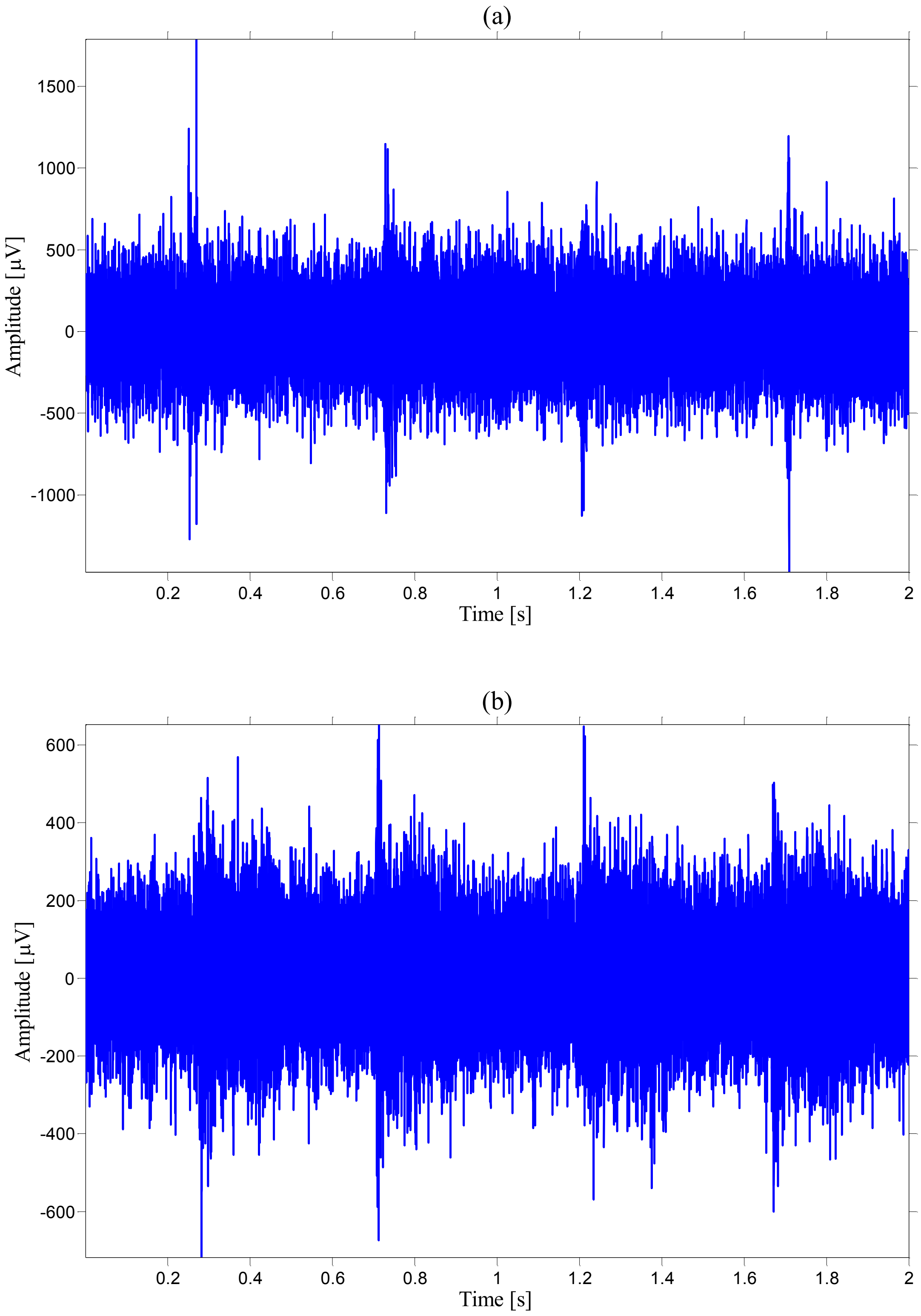

Figure 6-1: Graphs of neural recordings taken from the audio cortex of a guinea pig using (a) an iridium oxide electrode and (b) a boron-doped-diamond electrode.

Some techniques can be extremely useful in certain situations where the expected action potential shape is known before the experiment, or the action potential detection can be supervised, and a template devised during the experiment. However, in chronic implantations where the shape of the action potentials might change, or in experiments where supervision is impractical, these methods (matched filtering [2] or principal components [3]) are not sufficient. Instead, methods that are unsupervised and require no *a priori* knowledge are of the greatest interest. The methods being considered involve power detection [4], the discrete wavelet transform (DWT) [5-7], and the continuous wavelet transform (CWT) [8]. The goal of this work is to compare these methods by using them to detect simulated neural spikes in varying amounts (and types) of noise. This work differs from previous work because the same method for identifying action potentials is used for each transform method (the DWT, CWT, and energy transform). This work should identify which unsupervised method(s) are best suited for use in detecting action potentials in very poor SNR applications.

6.2 Action Potential Detection Techniques

6.2.1 Traditional Techniques

Thresholding

The simplest method of detecting action potentials is thresholding. In thresholding, the signal level is compared to a preset threshold (requiring supervision), and anytime the signal exceeds the threshold, an action potential is detected. Additional thesholding techniques include absolute thesholding and double thesholding (Also known as the window discriminator). In absolute thresholding, the absolute value of the signal is taken before thresholding (any DC component is typically removed before taking the absolute value). Thresholding and absolute thresholding don’t take any account of frequency or event length, they depend solely on voltage. Double thresholding depends on event length, as well as the amplitude, of the recorded signal. In double thresholding, the signal must exceed a first threshold, then fall beneath a second threshold, within a certain period of time. Examples showing each thresholding method can be seen in Fig. 6-2. Thresholding can be unsupervised, being set from estimates of the mean and standard deviation of the noise. More advanced detection techniques always rely on some form of thresholding for ultimately detecting action potentials.

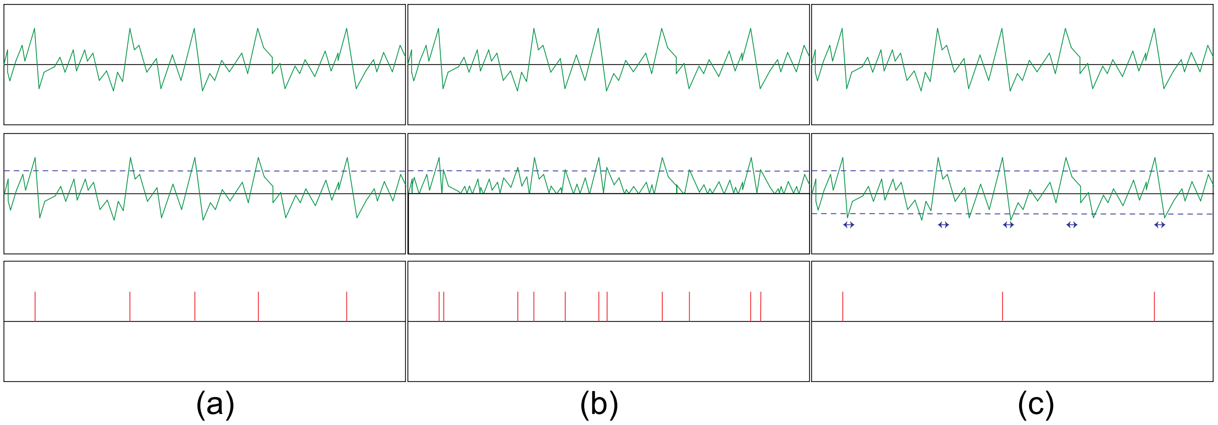

Figure 6-2: Demonstration of how thresholding is performed, with the top row showing the input signal, the second row showing the threshold being applied, and the bottom row showing the detected neural spikes, for (a) single thresholding, (b) absolute thresholding, and (c) double thresholding.

Band-Pass Filtering

Band-pass filtering takes advantage of the fact that action potentials are highly stereotyped and have a particular power spectrum. If the power spectrum of the action potentials is known, band-pass filtering can be used to remove noise from other frequencies. This is very useful when there is little overlap between the power spectra of the action potential signal and the noise signal. However, this is typically not the case. There are typically two large sources of noise in the recorded signal. The first source of noise comes from the equipment being used to record the signal. This noise is typically adequately modeled by white noise, and band-pass filtering can be used to sufficiently filter this noise in all but the most extreme noise levels. The second source of noise comes from the recording environment, made up of signals from nearby neurons and the superposition of many far-away neurons. Unfortunately since this noise is largely generated from action potentials, the power spectrum is not white, but resembles the spectrum of individual action potentials. Due to the related spectra, band-pass filtering is not very effective at removing this noise.

6.2.2 Advanced Techniques

Discrete Wavelet Transform

Several techniques have been developed that use the discrete wavelet transform (DWT). The DWT is a transformation technique similar to the discrete Fourier transform (DFT), but whereas the DFT converts temporal information into frequency information, the DWT retains temporal information as well as obtaining frequency information. This is accomplished by the use of wavelets in the transformation rather than the waves (sinusoids) used in the Fourier transform. The wavelet transformation is defined by:

$$W(\alpha,\tau) = \int_{-\infty}^{\infty} x(t)\frac{1}{\alpha^{1/2}}\psi\left(\frac{t-\tau}{\alpha}\right)dt$$

Where $W(\alpha,\tau)$ are the wavelet coefficients for scale (α) and translation (τ), $\Psi(t)$ is the mother wavelet, and $x(t)$ is the original signal. For the DWT, dydadic scales and translations from a discrete set ($\alpha = 2^j$; $\tau = k*2^j$; $j,k \in Z$) are necessary so that the basis functions ($\Psi[\alpha,\tau]$) form an orthonormal basis. This means that the data at each scale is unique in that the original signal can be reconstructed from the approximations at all of the scales. Different levels of the DWT give different resolutions of temporal versus frequency information. As the frequency resolution increases (low frequencies), the temporal resolution decreases. Whereas at high frequencies, the frequency resolution is poor, and the temporal resolution is increased. The DWT works as an action potential detector because at some scales (levels) the frequency spectra of the wavelet match the frequency spectra of the action potential. One technique uses a non-linear combination of multiple DWT scales to detect action potentials [5]. This technique has excellent results under certain conditions, but requires *a priori* information about the action potentials being detected and predictable noise. Another DWT technique uses a sum of multiple DWT scales [6]. This technique has better overall performance than the previous technique as shown by [5]. Other techniques include array denoising using the DWT [7], and a simplified version of the DWT known as wavelet lifting (WL). One of the most promising aspects of the DWT method is the simplicity of implementation. The WL method further simplifies the implementation making it an ideal candidate for real-time detection for implantable devices. One drawback of the DWT is that it is negatively impacted by non-stationary noise.

Power Detection

Power detection is also known as energy detection and involves calculating the instantaneous power of the signal and comparing it to the mean and standard deviation of the power to detect neural spikes. The power detection methods of interest use the Teager energy operator (TEO) (also known as the Teager-Kaiser energy operator) and the multi-resolution Teager energy operator (MTEO) [4]. The TEO in discrete time is simply:

$$P[n] = x^2[n] - x[n-1]x[n+1]$$

Where P is the power of the signal x. The output from an energy operator is typically windowed. The TEO can also be changed to work at different resolutions. The TEO at different scales is typically known as the kTEO, which is calculated by:

$$P[n] = x^2[n] - x[n-k]x[n+k]$$

Where k indicates the resolution of the operator. The MTEO uses multiple kTEO's in order to detect action potentials. This results in a much more robust action potential detector.

The limitation of the MTEO is in cases of severe SNR, where the MTEO has more false positives than other techniques.

Continuous Wavelet Transform

The CWT is almost identical to the DWT, even the definition is the same:

$$W(\alpha,\tau)=\int_{-\infty}^{\infty}x(t)\frac{1}{\alpha^{1/2}}\psi\left(\frac{t-\tau}{\alpha}\right)dt$$

The difference between the DWT and CWT lies in the selection of scales. The DWT is for discrete signals with dydadic scales and translations, ensuring the original signal can be recovered from the transform and the basis of the transform is orthonormal. The CWT has discrete signals, scales, and translations, but they scales and translation need not be dydadic, leading to redundancy in the wavelet coefficients and inability to recreate the original signal. The translations are discrete and determined by the sampling rate, i.e. $\tau=n/f_s$ where n is the sample number and f_s is the sampling frequency. The scales are also discrete, but determined by the user depending on the expected length of the action potential. Action potential lengths are highly regular, although the lengths vary in different animals and brain areas. The CWT only considers events with lengths similar to the expected action potential. This serves to limit much of the noise from other frequencies. For this reason, the CWT is expected to have the fewest false positives in poor SNR applications.

6.3 Methods

6.3.1 Simulating Neural Signals

In order to determine which action potential detection method performs the best for low SNR applications, a sample signal needs to be generated in order to test the detection methods. For this purpose, simulated action potentials were used, which can be seen in Fig. 6-3. The simulated signal had a sampling frequency of 10 kHz.

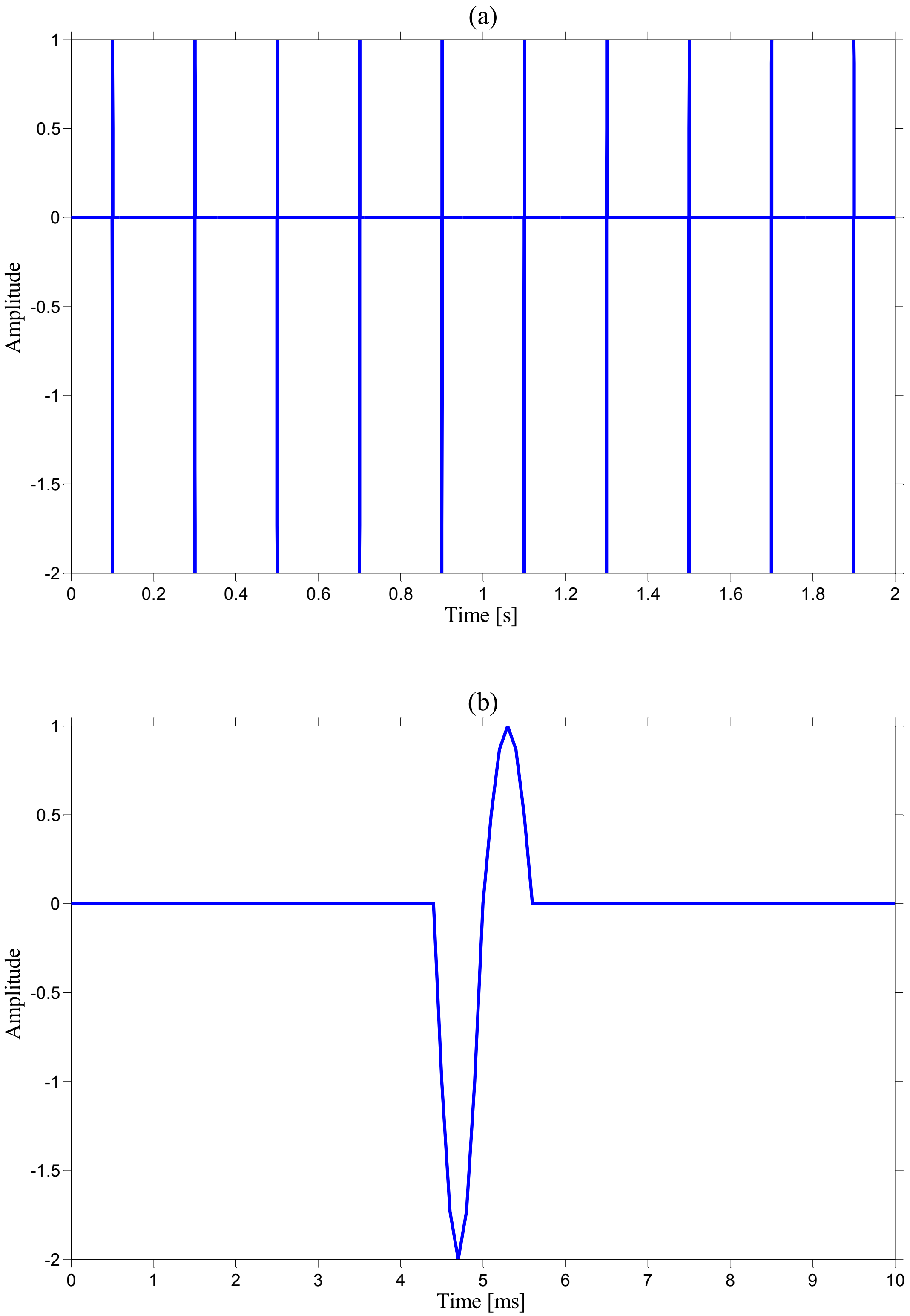

Figure 6-3: Graphs of (a) a simulated neural spike train and (b) an individual simulated neural spike.

To thoroughly test the detection methods, several forms of noise were added to the signal. Two different colors of noise were considered. White noise was considered because it accurately represents noise generated from recording hardware. Pink noise was also considered since it approximates the power spectrum of noise from the recording environment. The power spectra of the clean signal, white noise, and pink noise can all be seen in Fig. 6-4. It is apparent that action potential detection should be more difficult in pink noise. In addition to two colors of noise, non-stationary noise was also considered. To generate non-stationary noise, the amplitude of the noise was varied throughout a short (10 second) simulated neural signal. An example of non-stationary pink noise added to the simulated spike train can be seen in Fig. 6-5. So the four forms of noise considered are stationary white noise, non-stationary white noise, stationary pink noise, and non-stationary pink noise.

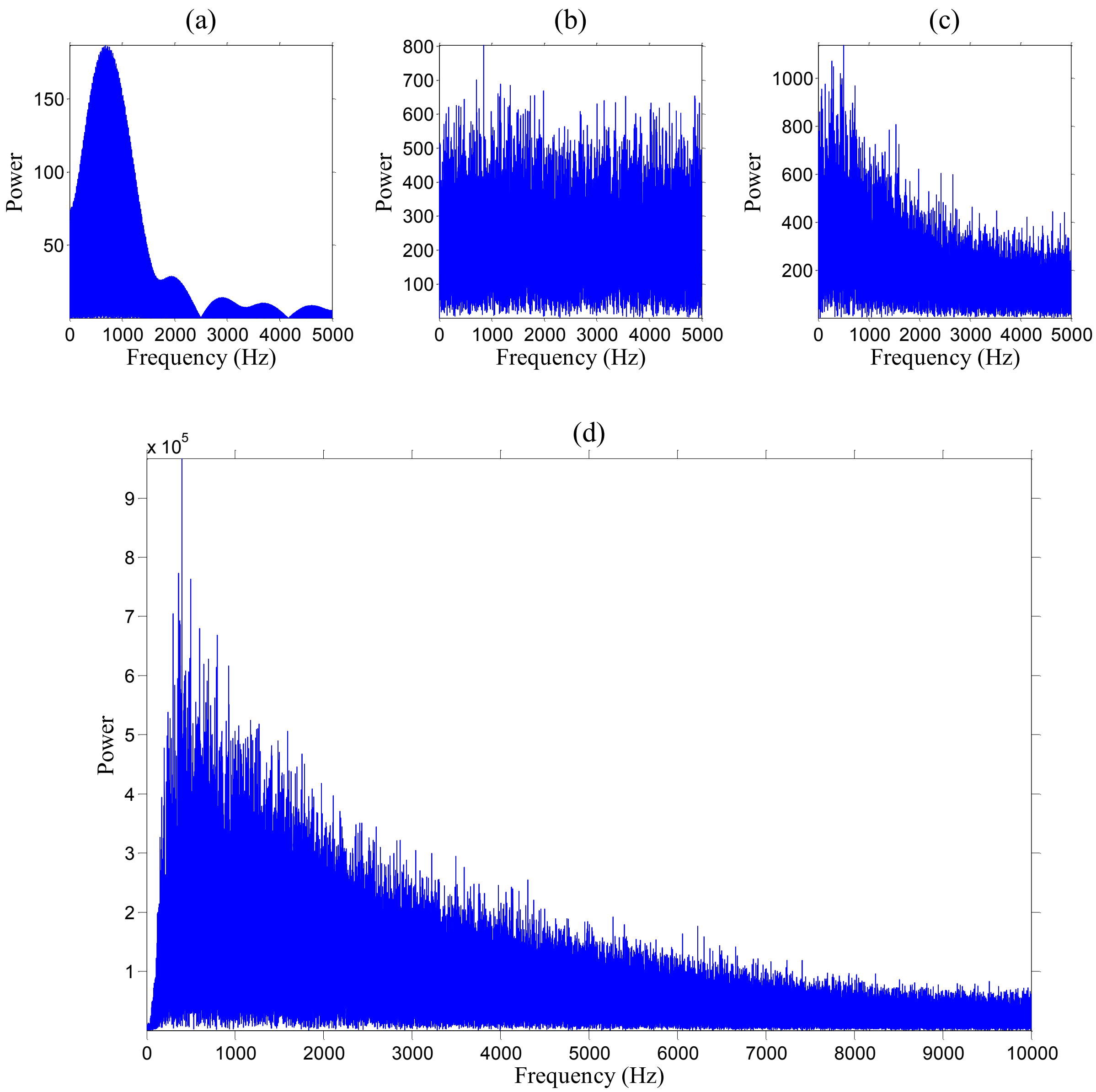

Figure 6-4: Power spectra of (a) a simulated neural spike train, (b) generated white noise, (c) generated pink noise, and (d) recorded neural signal shown in Fig. 6-1, from a boron-doped-diamond electrode.

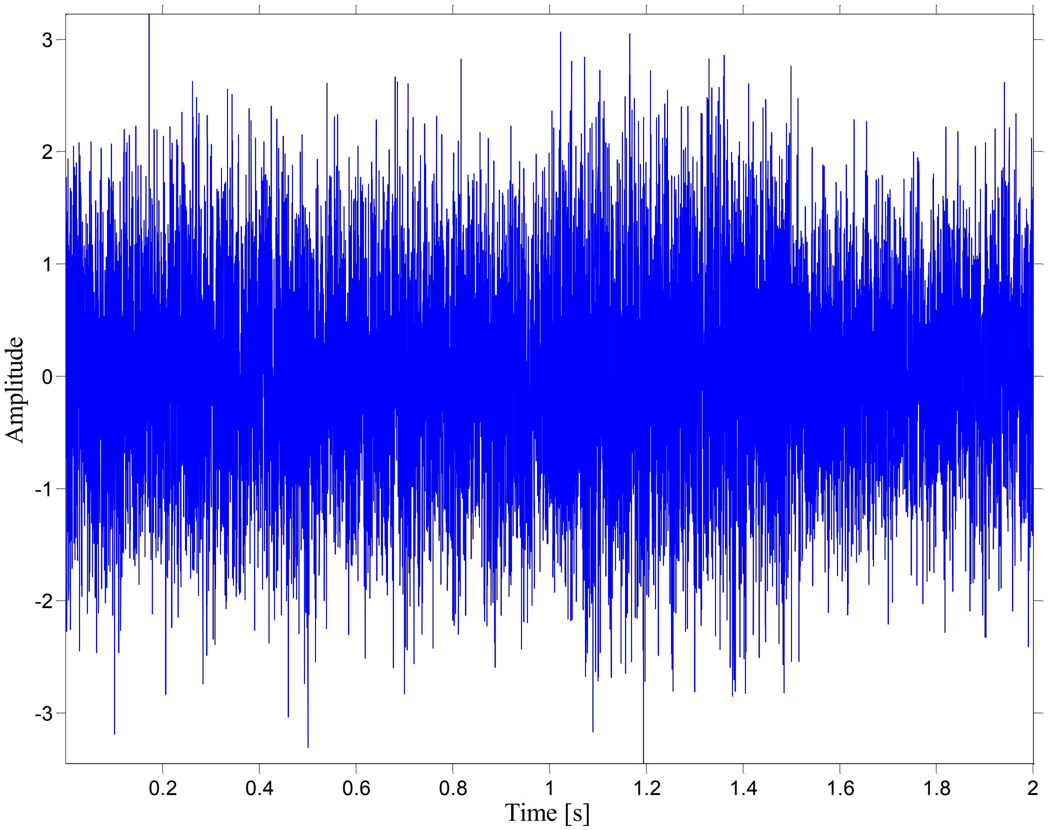

Figure 6-5: Graph of simulated neural spike train with non-stationary pink noise added with a base SNR of -20 dB.

To test each detection method, 1000 trials were conducted for each form of noise over a range of different SNRs. The SNR was determined by the ratio of the power of the clean signal to the power of the noise. The SNRs used ranged from -10 dB to -20 dB in 1 dB increments. The final variable varied was a cost measure, I. This variable represents the ratio of cost of false alarms to the cost of omission of real spikes. The range considered covered ratios of less than .001 and greater than 1000. In total, 396,000 trials were performed.

6.3.2 DWT Method

As seen by the spectrum of the simulated neural spikes (Fig 6-4), the principle frequencies of interest range from about 250 Hz to 1250 Hz (.8 to 4 ms). With a sampling rate of 10 kHz, the first 4 dydadic scales of the DWT correspond to 5000 Hz, 2500 Hz, 1250 Hz, and 625 Hz (.2, .4, .8, and 1.6 ms). These are the scales considered in the DWT algorithm to detect action potentials. The wavelet used for the DWT was the biorthonormal 1.5 wavelet, as its shape is reminiscent of a biphasic action potential.

6.3.3 MTEO Method

For the MTEO detection method, 4 kTEO filters were used (k=5, 10, 15, and 20 [corresponding to frequencies of 2000, 1000, 667, and 500 Hz and event lengths of .5, 1, 1.5, and 2 ms]). Each kTEO filter was windowed.

6.3.4 CWT Method

For the CWT detection, again 4 scales were used, this time corresponding to .5, 1, 1.5, and 2 ms (or 2000, 1000, 667, and 500 Hz; the same as the MTEO method). The wavelet used for the CWT was the biorthonormal 1.5 wavelet.

6.3.5 Resolving Action Potentials

The method of detecting action potentials at each scale, combining the decisions at individual scales, and estimating the spike arrival times is described by Nenandic *et al.* [8], whose method was based on work from Donoho *et al.* [9]. At each individual scale, the noise level is estimated from the mean, median, and standard deviation of the wavelet coefficients. Any coefficients exceeding a threshold are marked. The coefficients from each scale exceeding their noise threshold are all combined and if the event length is less than the longest expected neural spike event length, it is considered an action potential. The cost variable I is used in setting the threshold at each scale. The results from the detection algorithm were then compared to the times of simulated action potentials. The number of true positives, false positives, and omissions were tracked for all trials.

6.4 Results

For every combination of cost variable l (-0.2, -0.15, -0.1, -0.05, 0, 0.05, 0.1, 0.15, 0.2), SNR (-10, -11, -12, -13, -14, -15, -16, -17, -18, -19, -20), and noise type (white Gaussian noise [WGN], non-stationary white Gaussian noise [NSWGN], pink Gaussian noise [PGN], non-stationary pink Gaussian noise [NSPGN]), 1000 simulations were run for each detection method (DWT, CWT, and MTEO). The number of correct detections (true positives) from each trial was recorded and averaged, along with the number of false alarms (false positives). The number of simulated spikes in each test was 10, so the number of omissions is simply the number of true positives subtracted from 10.

For the case where the cost of omissions is equal to the cost of false positives (l=0) the average number of true positives versus the SNR is plotted in Fig. 6-6 for each of the noise types. In Fig. 6-6 (and subsequent figures), the DWT method's results are plotted in blue, the CWT method's results are plotted in red, and the MTEO method's results are plotted in green. Fig. 6-7 shows the number of false positives for the same equal cost case. In terms of number of true positives, it would appear that the MTEO method has the best performance at low SNR, while the CWT method had the best performance in higher SNR. In terms of number of false positives, the DWT method has the fewest under a SNR lower than -14 dB for white noise and lower than -12 dB for pink noise. In signals with relatively little noise (-10 dB) the MTEO method has the fewest false positives in white noise. However, in poor SNR applications, the MTEO method results in a staggering number of false positives for all noise types. To help determine which wavelet method has better performance in low SNR applications, the ratio of false positives to true positives was evaluated, seen in Fig. 6-8. The false positive to true positive ratio is comparable between the two methods.

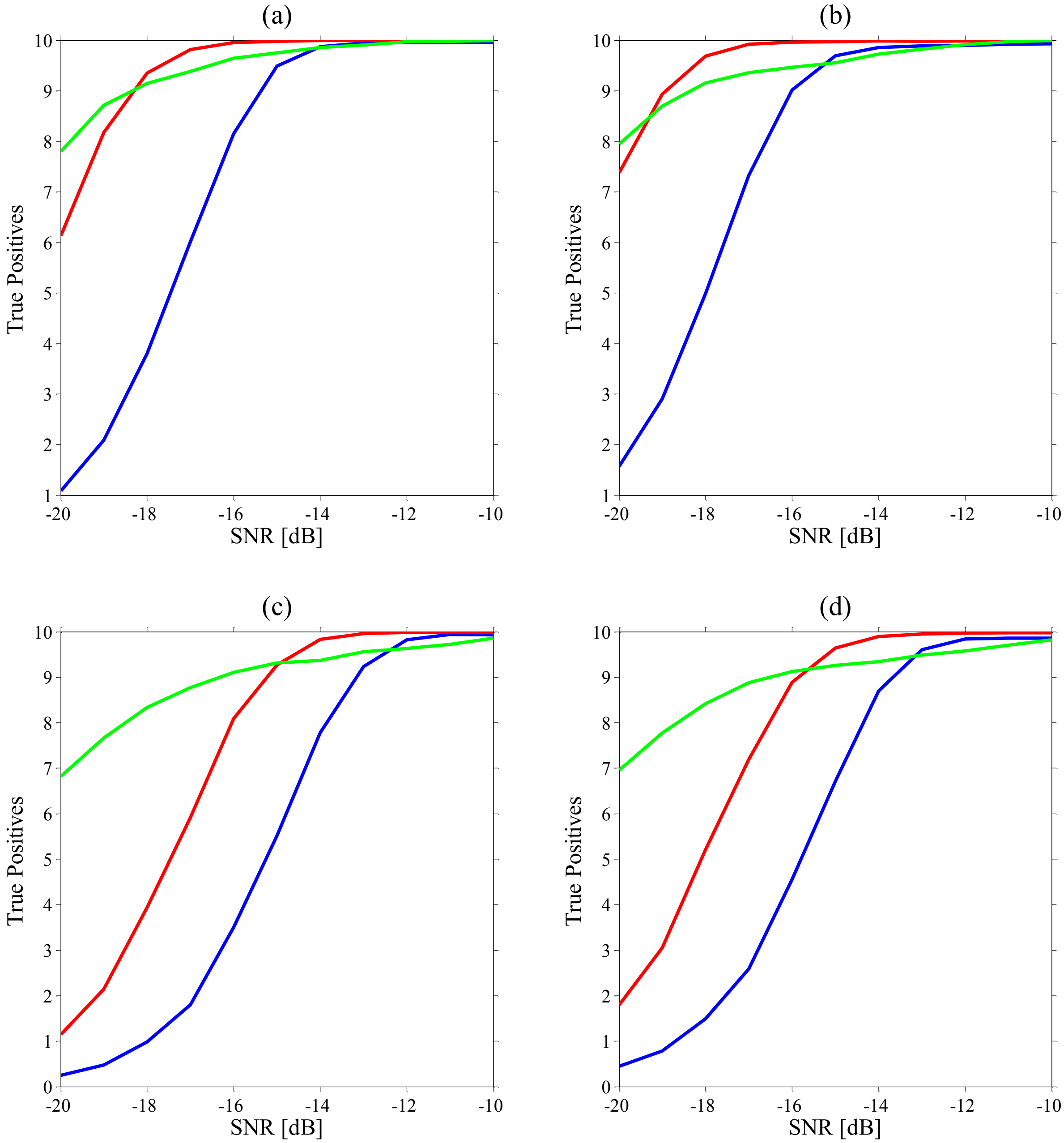

Figure 6-6: True positives detected action potentials (out of 10) versus SNR for simulated neural signals with added (a) stationary white Gaussian noise, (b) non-stationary white Gaussian noise, (c) stationary pink Gaussian noise, and (d) non-stationary pink Gaussian noise. The cost ratio variable, l, was set to 0, where the cost of omissions was equal to the cost of false positives. Blue represents the DWT method, red represents the CWT method, and green represents the MTEO method.

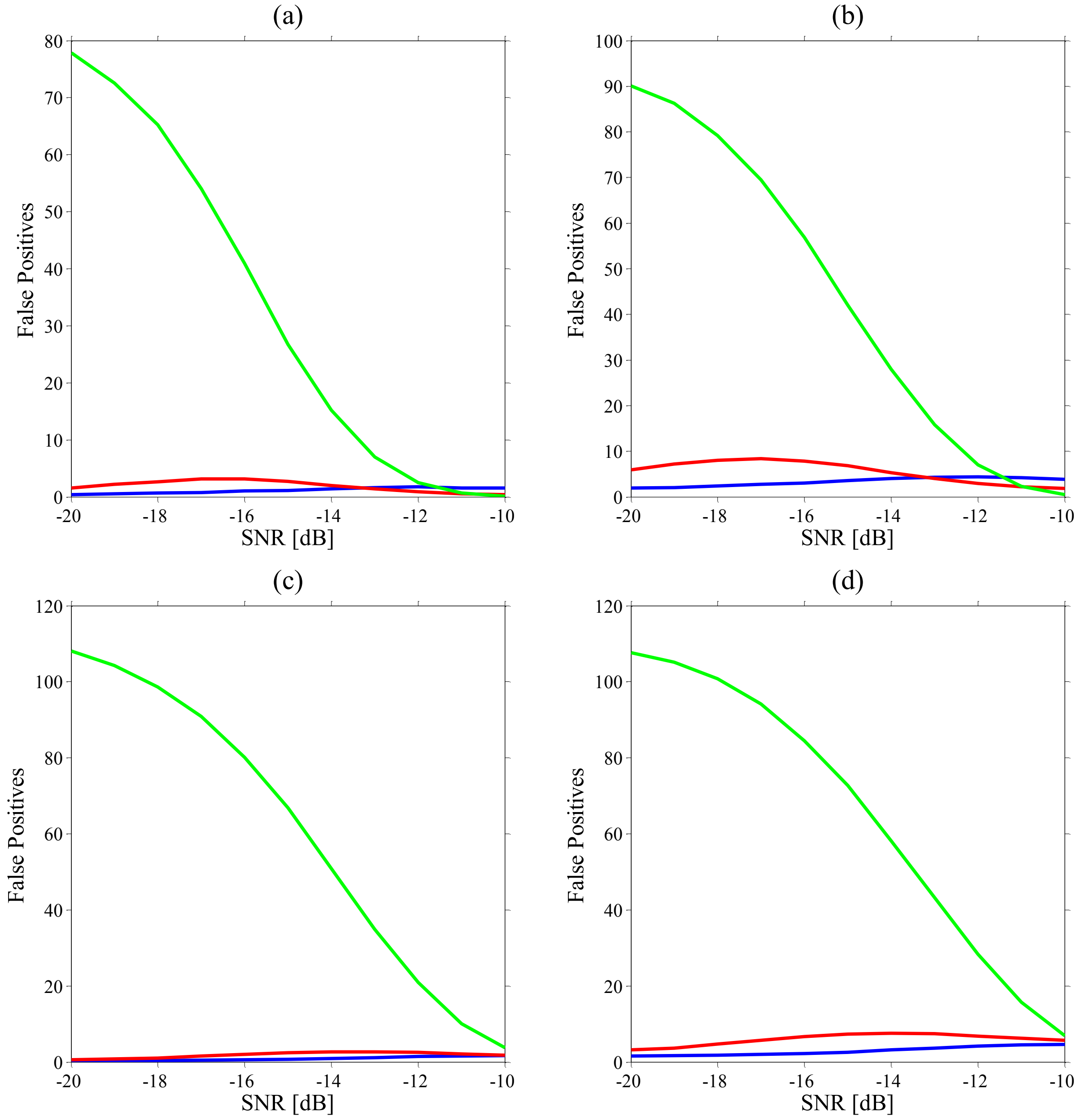

Figure 6-7: False positives detected versus SNR for simulated neural signals with added (a) stationary white Gaussian noise, (b) non-stationary white Gaussian noise, (c) stationary pink Gaussian noise, and (d) non-stationary pink Gaussian noise. The cost ratio variable, I, was set to 0, where the cost of omissions was equal to the cost of false positives. Blue represents the DWT method, red represents the CWT method, and green represents the MTEO method.

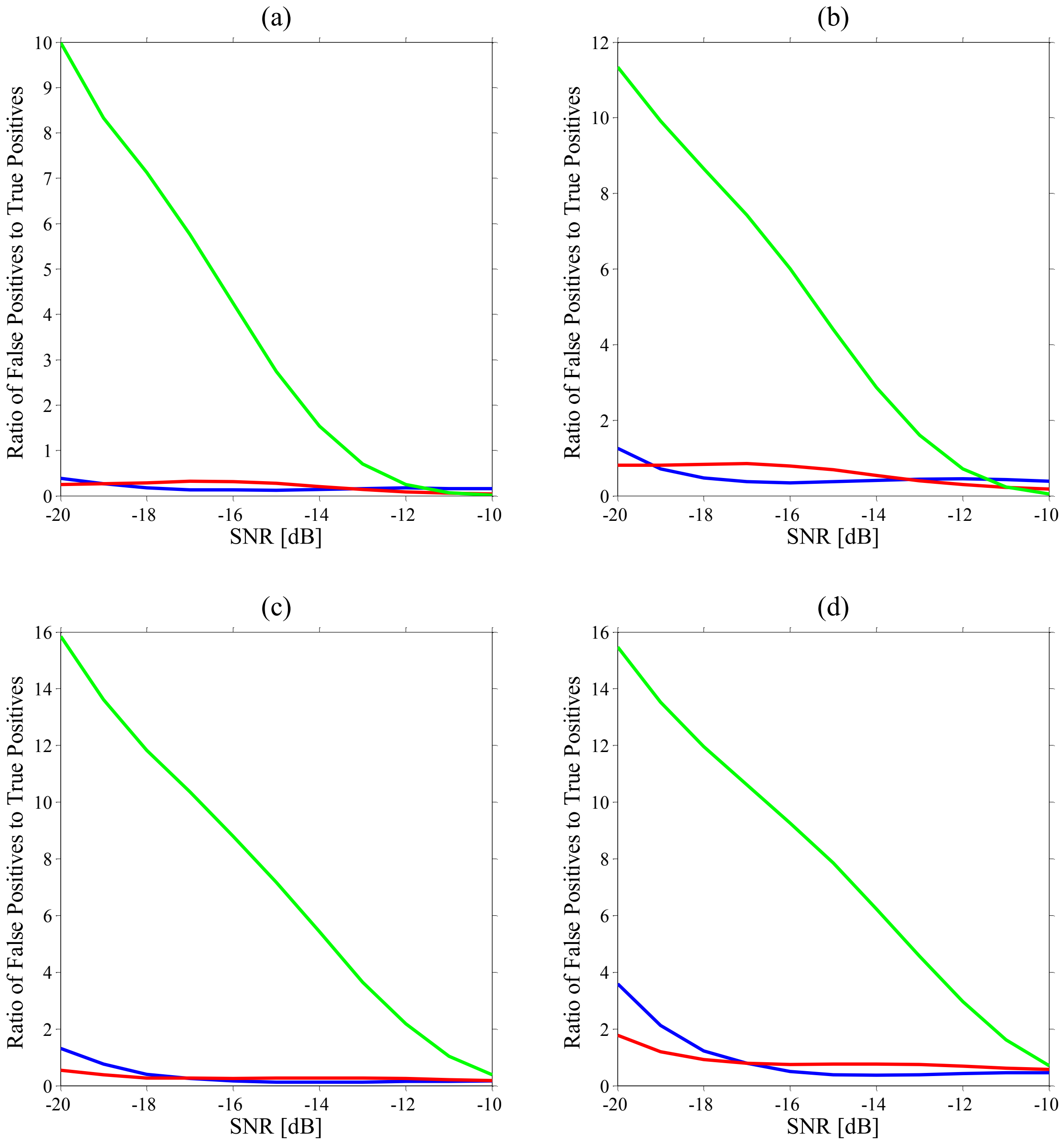

Figure 6-8: Ratio of false positives to true positives versus SNR for simulated neural signals with added (a) stationary white Gaussian noise, (b) non-stationary white Gaussian noise, (c) stationary pink Gaussian noise, and (d) non-stationary pink Gaussian noise. The cost ratio variable, l, was set to 0, where the cost of omissions was equal to the cost of false positives. Blue represents the DWT method, red represents the CWT method, and green represents the MTEO method.

In order to establish which method has the best performance, additional cost ratio cases were evaluated. Figs. 6-9 and 6-10 show the number of true positives detected by each method over a wide range of cost ratios. Figs. 6-11 and 6-12 show the number of false positives detected by the methods for the same range of cost ratios. It would appear that overall the CWT method appears to perform the best at low SNR, while MTEO might be the best at high SNR. In order to quantify which method had the best performance, a new figure of merit was devised. The figure of merit was calculated by the equation:

$$Figure\ of\ Merit = (1 + [\#\ of\ Omissions]) * (1 + [\#\ of\ False\ Positives])$$

This figure of merit has a minimum value of 1 when there are no omissions or false positives. The values for the figure of merit were calculated for each value of I and each SNR. The minimum values across all I values were taken and plotted against SNR in Fig. 6-13. Fig. 6-13 shows very clearly that the CWT method has the best overall performance over the entire range of SNR evaluated and for all noise types considered. However, all methods have comparable performance in cases of high SNR (-10 dB). It is also worth noting that all methods have considerably poorer performance in the presence of pink noise, as compared to white noise, with poor SNR.

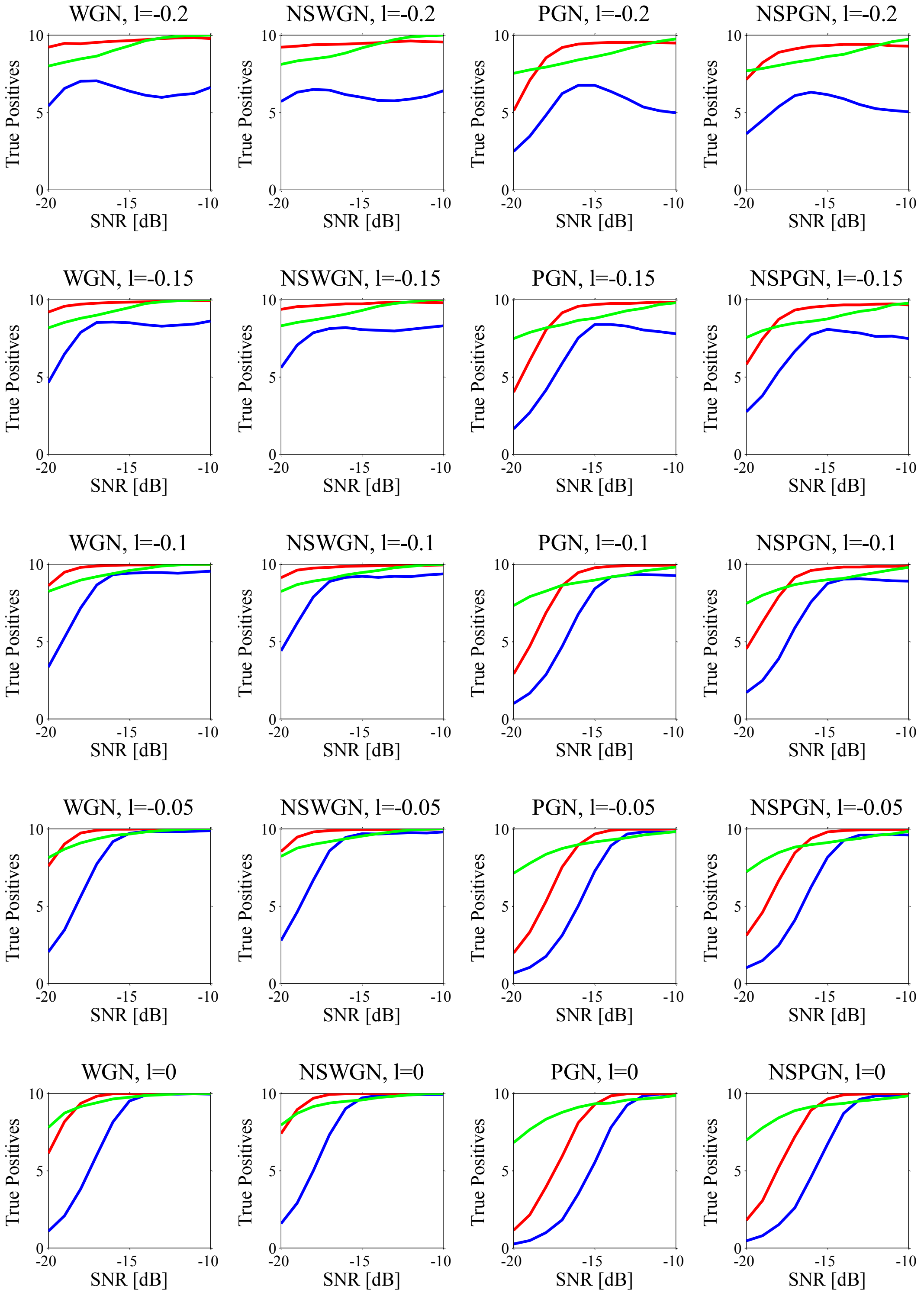

Figure 6-9: True positives (out of 10) versus SNR for l values with cost ratios ranging from .001 to 1 (cost of omissions is higher than cost of false positives). Blue represents the DWT method, red represents the CWT method, and green represents the MTEO method.

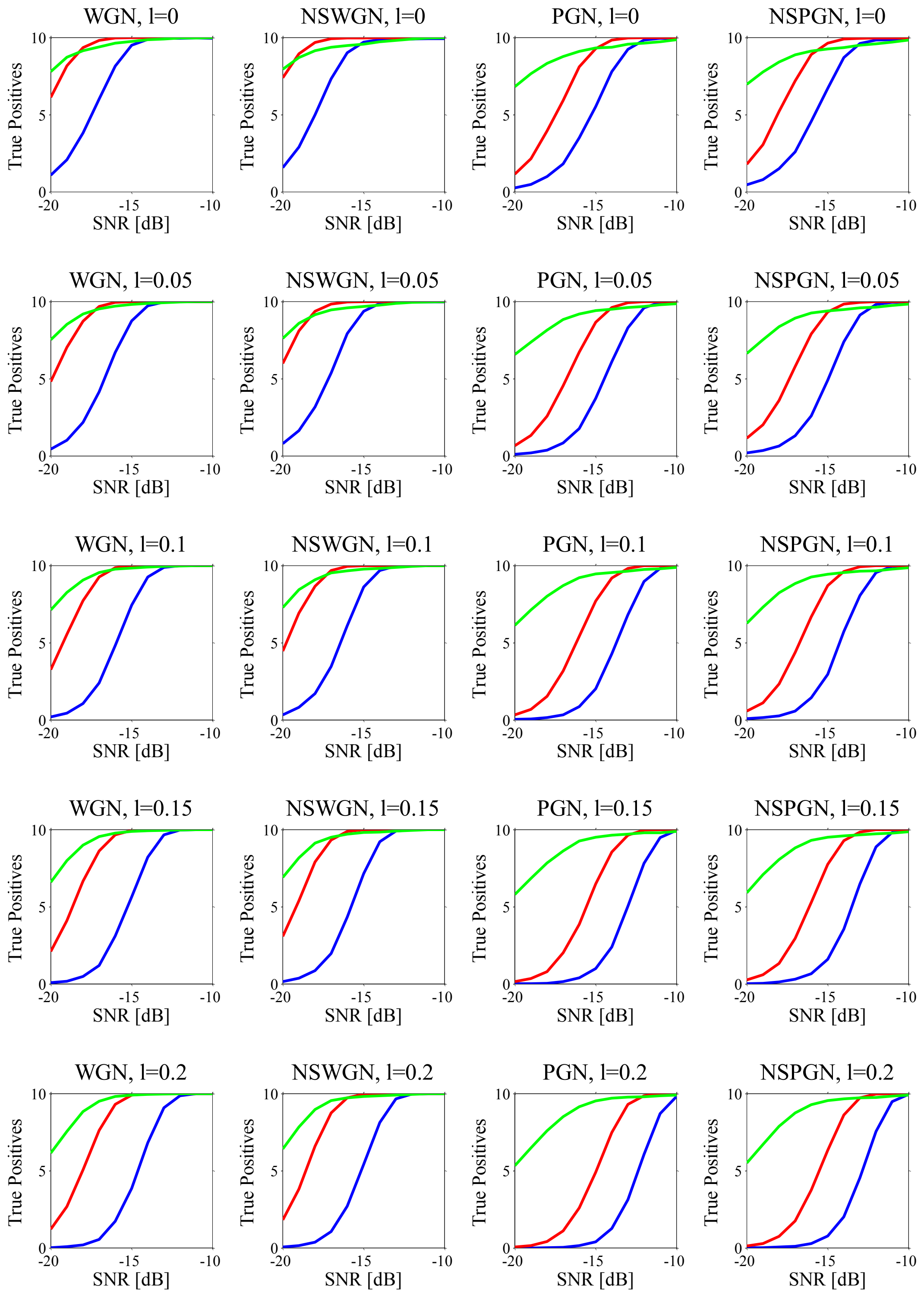

Figure 6-10: True positives (out of 10) versus SNR for l values with cost ratios ranging from 1 to 1000 (cost of omissions is lower than cost of false positives). Blue represents the DWT method, red represents the CWT method, and green represents the MTEO method.

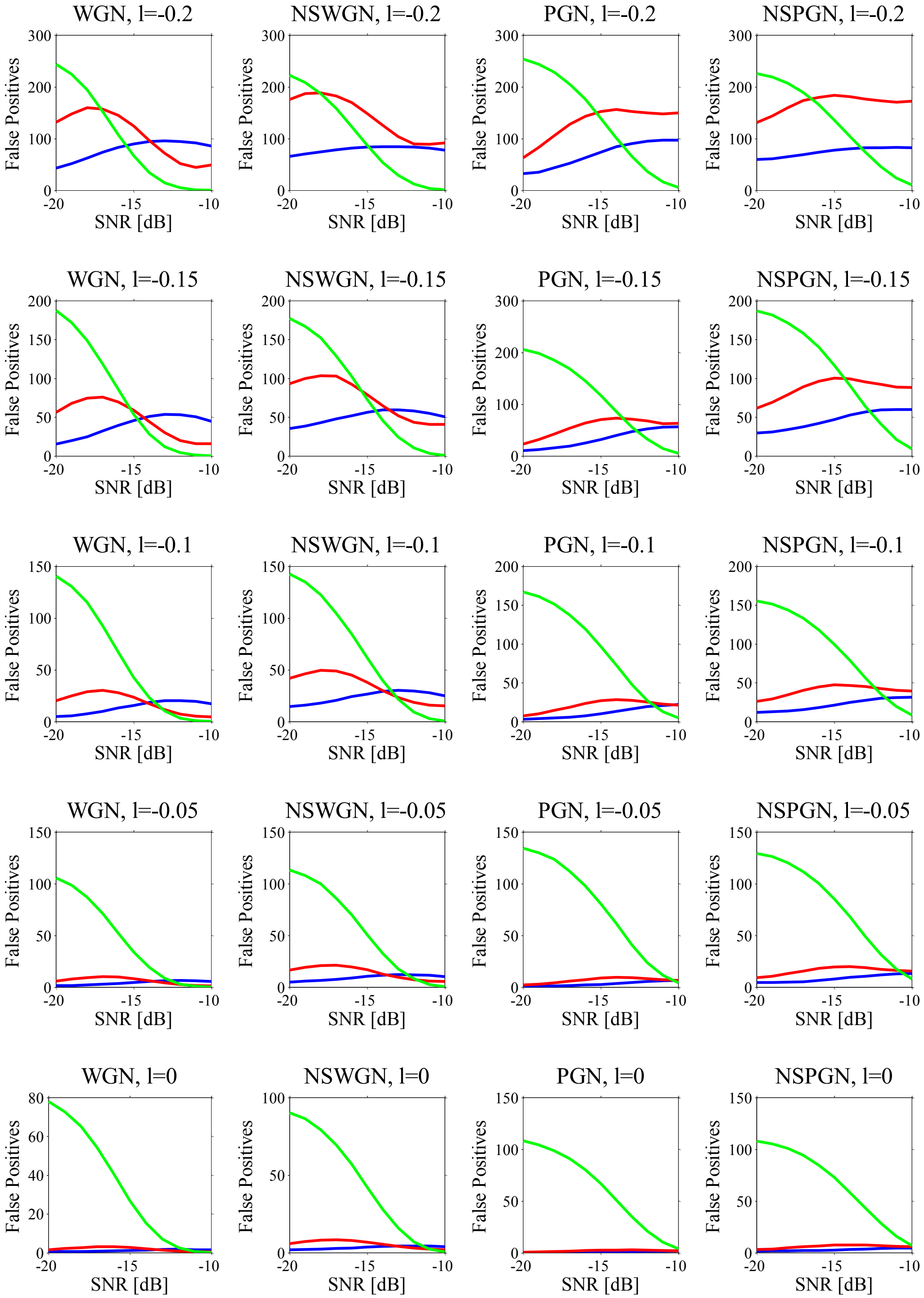

Figure 6-11: False positives versus SNR for l values with cost ratios ranging from .001 to 1 (cost of omissions is higher than cost of false positives). Blue represents the DWT method, red represents the CWT method, and green represents the MTEO method.

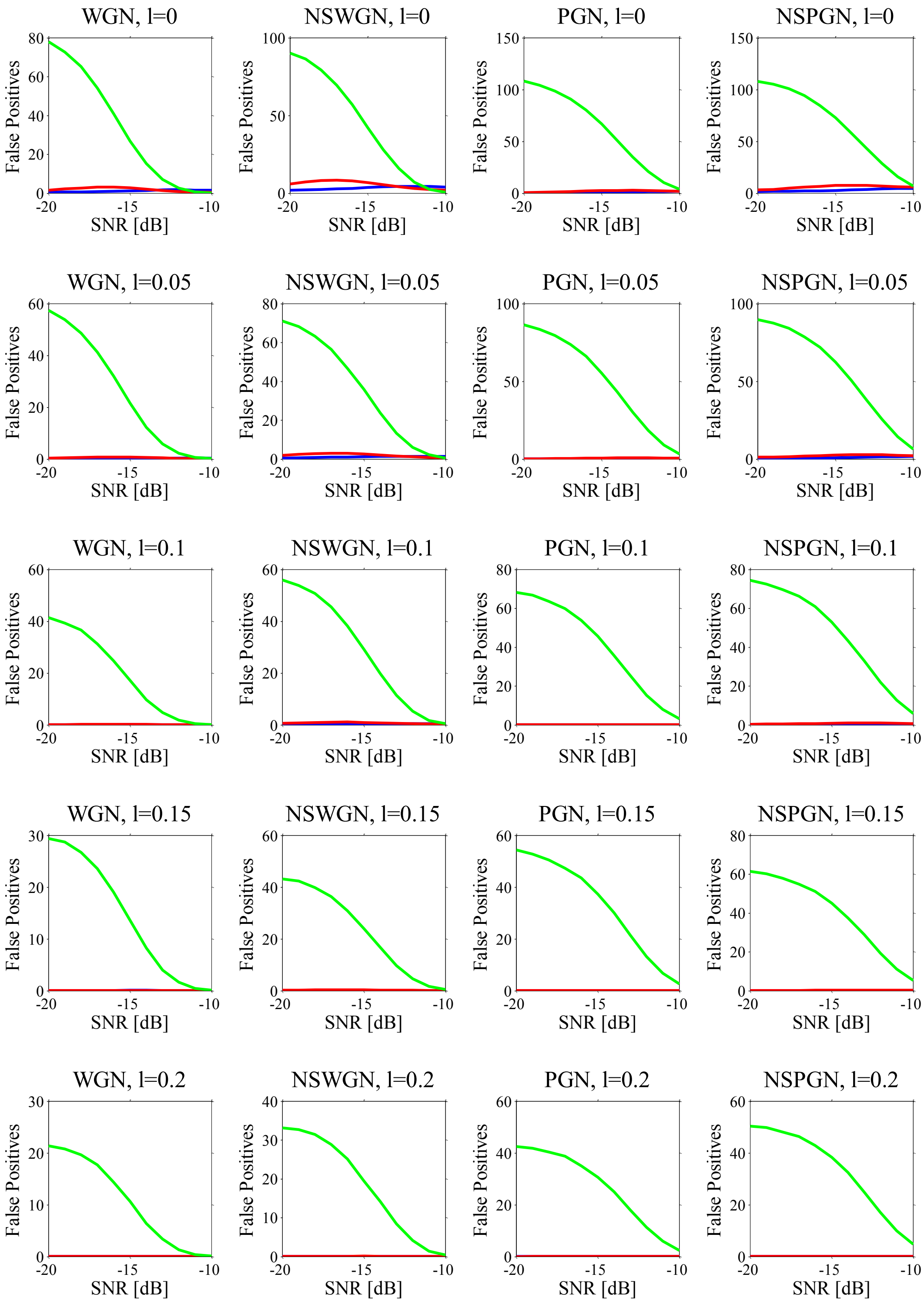

Figure 6-12: False positives versus SNR for l values with cost ratios ranging from 1 to 1000 (cost of omissions is lower than cost of false positives). Blue represents the DWT method, red represents the CWT method, and green represents the MTEO method.

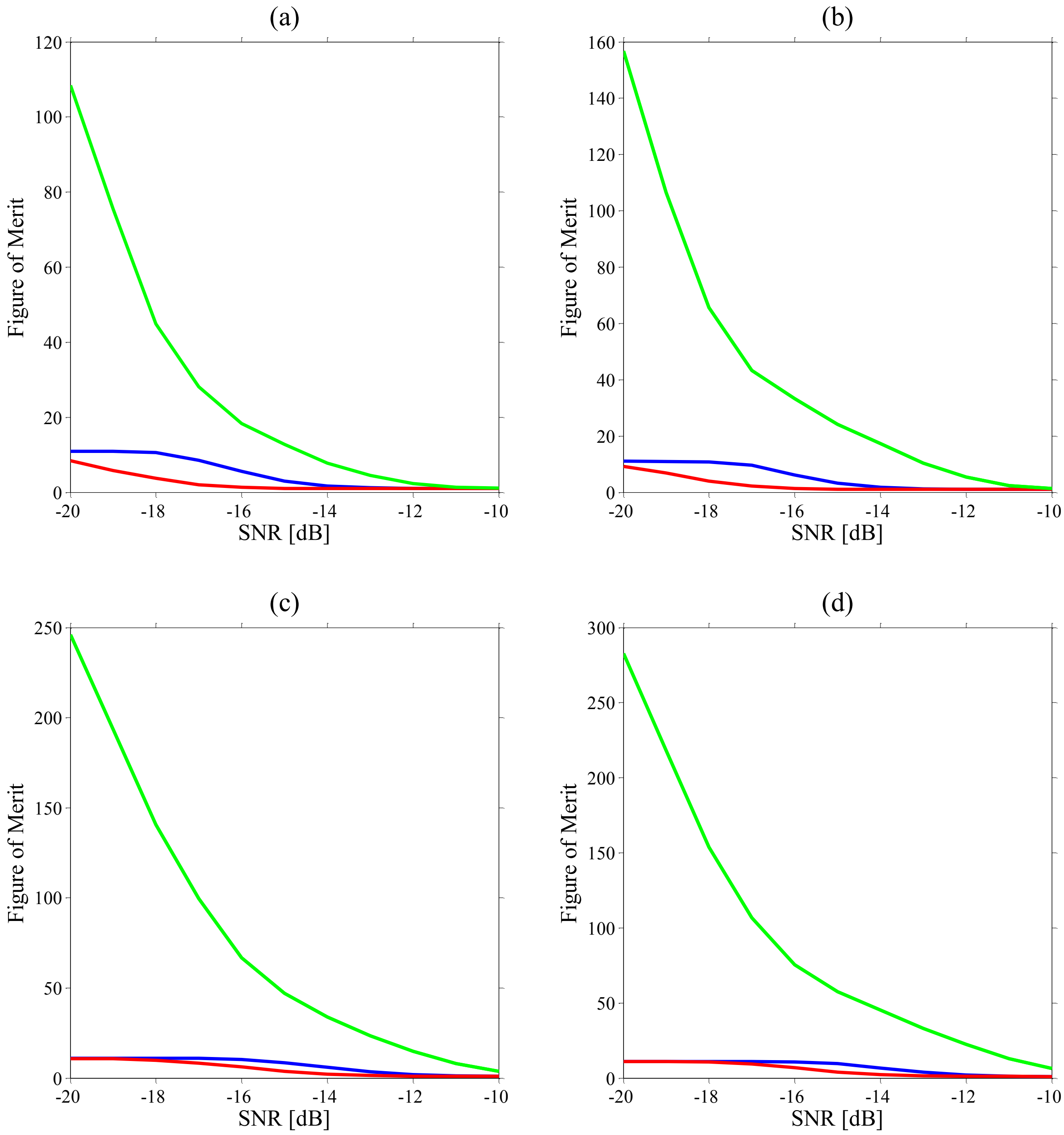

Figure 6-13: Figure of merit versus SNR for each method for simulated neural signals with added (a) stationary white Gaussian noise, (b) non-stationary white Gaussian noise, (c) stationary pink Gaussian noise, and (d) non-stationary pink Gaussian noise. The figure of merit is calculated by (1 + [omissions]) * (1 + [false positives]) and taking the lowest value across all values of l. Blue represents the DWT method, red represents the CWT method, and green represents the MTEO method.

6.5 Conclusion

Accurate action potential detection is important in neuroscience studies. Extracellular recordings tend to have poor SNR due to electrode placement, biofouling, and outside noise sources. Traditional methods of detecting action potentials were reviewed and several methods of detecting action potentials in low SNR applications were explored (DWT, CWT, MTEO).

In order to determine which method had the best performance in low SNR applications, Monte Carlo simulations were performed to assess the performance of each method at various SNR. In addition, four types of noise were used in these trials, stationary and non-stationary white Gaussian noise, and stationary and non-stationary pink Gaussian noise. The MTEO method had the worst performance of the 3, except in cases with high SNR, where the performance was comparable. Between the DWT and CWT, the CWT method has better results than the DWT (more significantly in white noise than pink noise). However, the results are comparable, which means DWT might still be a better method for real-time spike detection, since it's algorithm is simpler to implement; in addition, the DWT can be used to re-create the original signal making it also an effective compression method for transmitting neural data. In post-processing of neural signals, the CWT appears to be the best choice of unsupervised action-potential detection in low SNR applications.

REFERENCES

REFERENCES

[1] J. P. Welsh and C. Schwarz, “Multielectrode recording from the cerebellum,” in *Methods for Neural Ensemble Recordings*, M. A. L. Nicolelis, Ed. Boca Raton, FL: CRC, ch. 5, pp. 79–100, 1999.

[2] I. N. Bankman, K. O. Johnson, and W. Schneider, “Optimal detection, classification, and superposition resolution in neural waveform recordings,” *IEEE Trans. Biomed. Eng.*, vol. 40, no. 8, pp. 836–841, Aug. 1993.

[3] M. Abeles and M. H. Goldstein, “Multispike train analysis,” *Proc. IEEE*, vol. 65, pp. 762–773, 1977.

[4] J. H. Choi, H. K. Jung, T. Kim, “A new action potential detector using the MTEO and its effects on spike sorting systems at low signal-to-noise ratios,” *IEEE Trans. Biomed. Eng.*, vol. 53, no. 4, pp. 738–7346, April 2006.

[5] K. H. Kim, S. J. Kim, “A wavelet-based method for action potential detection from extracellular neural signal recording with low signal-to-noise ratio,” *IEEE Trans. Biomed. Eng.*, vol. 50, no. 8, pp. 999–1011, Aug. 2003.

[6] V. Shalchyan, W. Jensen, D. Farina, “Spike detection and clustering with unsupervised wavelet optimization in extracellular neural recordings,” *IEEE Trans. Biomed. Eng.*, vol. 59, no. 9, pp. 2576–2585, Sept. 2012.

[7] K. G. Oweiss, D. J. Anderson, “Noise reduction in multichannel neural recordings using a new array wavelet denoising algorithm,” *Neurocomputing,* vol. 38–40, pp. 1687-1693, June 2001.

[8] Z. Nenandic, J. W. Burdick, “Spike detection using the continuous wavelet transform,” *IEEE Trans. Biomed. Eng.*, vol. 52, no. 1, pp. 74–87, Jan. 2005.

[9] D. L. Donoho and I. M. Johnstone, “Ideal spatial adaptation by wavelet shrinkage,” *Biometrika,* vol. 81, pp. 425–455, 1994.

CHAPTER: 7

Analysis of Neural Recording Experiments using the Continuous Wavelet Transform Method

7.1 Introduction

The efficacy of an acute neural recording device is best measured by its ability to accurately detect action potentials. In the neural recordings performed with diamond-based and single-material diamond neural probes (Chapter 5), it was found that there is a significant amount of noise in the recorded signals. The poor signal-to-noise ratio (SNR) of these recordings suggests that it would be hard to detect action potentials accurately using a simple thresholding technique. For this reason, different detection techniques were explored to determine which method performs the best with very poor SNR recordings (Chapter 6). The results showed that wavelet techniques far outperformed power detection techniques in noisy recordings. In addition, it was found that the continuous wavelet transform (CWT) method had the best overall detection rates. The aim of this chapter is to apply the CWT method to detect action potentials in neural recordings taken using silicon-based, diamond-based, and single-material diamond neural probes. The results will be analyzed to compare the thresholding and CWT detection techniques and to compare the efficacy of the three different probe types. The expectation is that all of the probe types will detect more action potentials using the CWT method instead of the basic thresholding technique, but that the probes with poorer SNR (the diamond-based probe and especially the single-material diamond probe) will benefit more. However, in order to demonstrate the efficacy of the diamond-based and single-material diamond neural probes, it must be demonstrated that the CWT method allows detection rates comparable to the silicon-based neural probes.

7.2 Application of Continuous Wavelet Transform Technique and Thresholding

The CWT detection was performed as described previously in Chapter 6. Six scales were used, corresponding to 0.5, 1, 1.5, 2, 2.5, and 3 ms (or 2000, 1000, 667, 500, 400, and 333 Hz), and the wavelet used was the biorthonormal 1.5 wavelet. For each scale, the noise level was estimated using the mean, median, and standard deviation of the wavelet coefficients. The noise threshold was set using a cost variable l being equal to zero, meaning the cost of false positives and the cost of omissions were considered equal. Coefficients exceeding the noise threshold were combined across all four scales. Events occurring within a typical event time (1.75 ms) of each other were combined. Events occurring within a typical refractory period (4.5 ms), but not within a typical event time (1.75 ms) were discarded. The remaining events, the detected action potentials, were compared with the onset of stimulus periods to determine their arrival time relative to the stimulus. These arrival times relative to the onset of stimulus were used to generate histograms similar to those from the analysis of neural recordings using the thresholding method in Chapter 5.

The basic thresholding method was reapplied similarly to Chapter 5. However, in Chapter 5, the thresholds were set manually in order to subjectively maximize the performance of the detection. While this does not invalidate the results from Chapter 5, it would make it impossible to make an objective comparison of the detection methods, as the CWT method uses automated selection of coefficient thresholds; the results would be biased toward one of the methods (most likely the basic thresholding method). One way to solve this inequality in methods would be to set the coefficient thresholds manually for each of the scales on each electrode (180 thresholds). However, this could still lead to some bias, as manual thresholds are ultimately susceptible to human error. Instead, the basic thresholding technique was re-performed using the same automated noise threshold determination used in the CWT method. That is, the noise threshold was estimated using the mean, median, and standard deviation of the absolute value of the signal, with a cost ratio of zero. Again, a cost ratio of zero indicates that the cost of a false positive is equal to the cost of an omission. When the signal exceeded the noise threshold, an event was marked. Events occurring within a typical event period (1.75 ms) were merged, while events occurring within a typical refractory period (4.5 ms) were discarded. The remaining events were compared with the stimulus periods applied to determine the arrival time of the action potentials relative to the onset of stimulus. Again, these arrival times were sorted into histograms like the ones described in Chapter 5.

7.3 Results

The basic thresholding and CWT detection methods were applied to recordings from silicon-based neural probes with iridium oxide electrodes, diamond-based neural probes with boron-doped-diamond electrodes, and single-material diamond probes with boron-doped-diamond electrodes, which have all been described previously. The silicon-based probes had 16 electrodes, the diamond-based probes had 8 electrodes, and the single-material diamond probes had 6 electrodes. The first results are plots of the recorded signals with markers (stems) indicating where the basic thresholding method detected action potentials and where the CWT method detected action potentials. In each of the plots, detections by basic thresholding are shown by blue stems above the recorded signal, while detections by CWT are shown by red stems below the recorded signal. Figs. 7-1 and 7-2 show the recorded signals and the detections by thresholding and CWT for each of the 16 electrode sites on the silicon-based neural probes with iridium oxide electrodes for the entire recording length. In addition, Figs. 7-3 and 7-4 show expanded views of 5 seconds of the recording time. Fig. 7-5 shows the recorded signals and the detections by thresholding and CWT for the entire recording length of the diamond-based neural probe with boron-doped-diamond electrodes. Fig. 7-6 shows a 5-second close-up of the same recordings. Fig. 7-7 shows the recordings and detected action potentials of the entire recording length from the single-material diamond probe with boron-doped-diamond electrodes. Fig. 7-8 shows the expanded view for a 5-second window of these recordings.

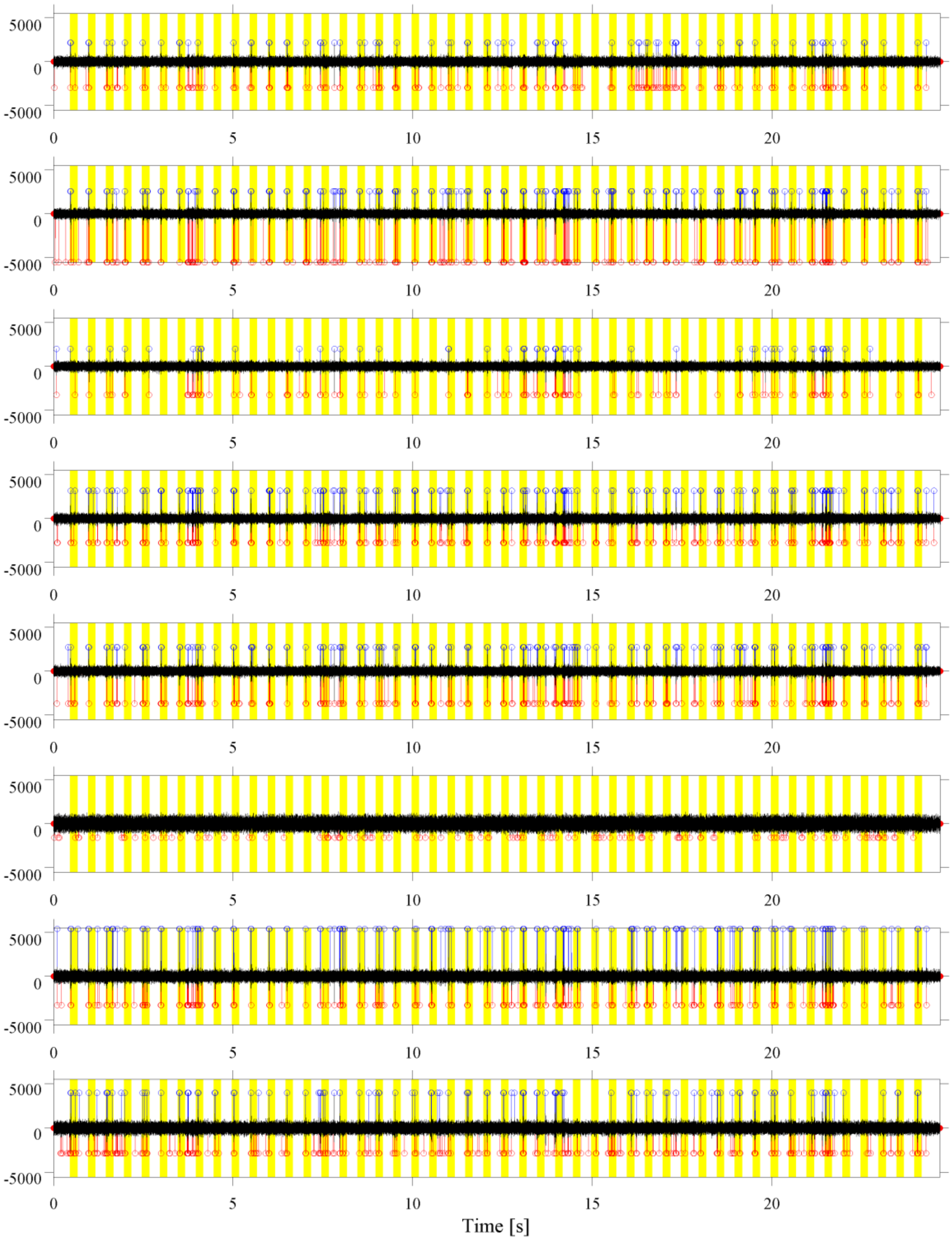

Figure 7-1: Neural recordings from the auditory cortex of a guinea pig taken with a silicon-based neural probe (channels 1-8). The stimulus periods are highlighted in yellow. Action potentials detected using the thresholding technique are shown with blue stems. Action potentials detected using the CWT method are shown with red stems.

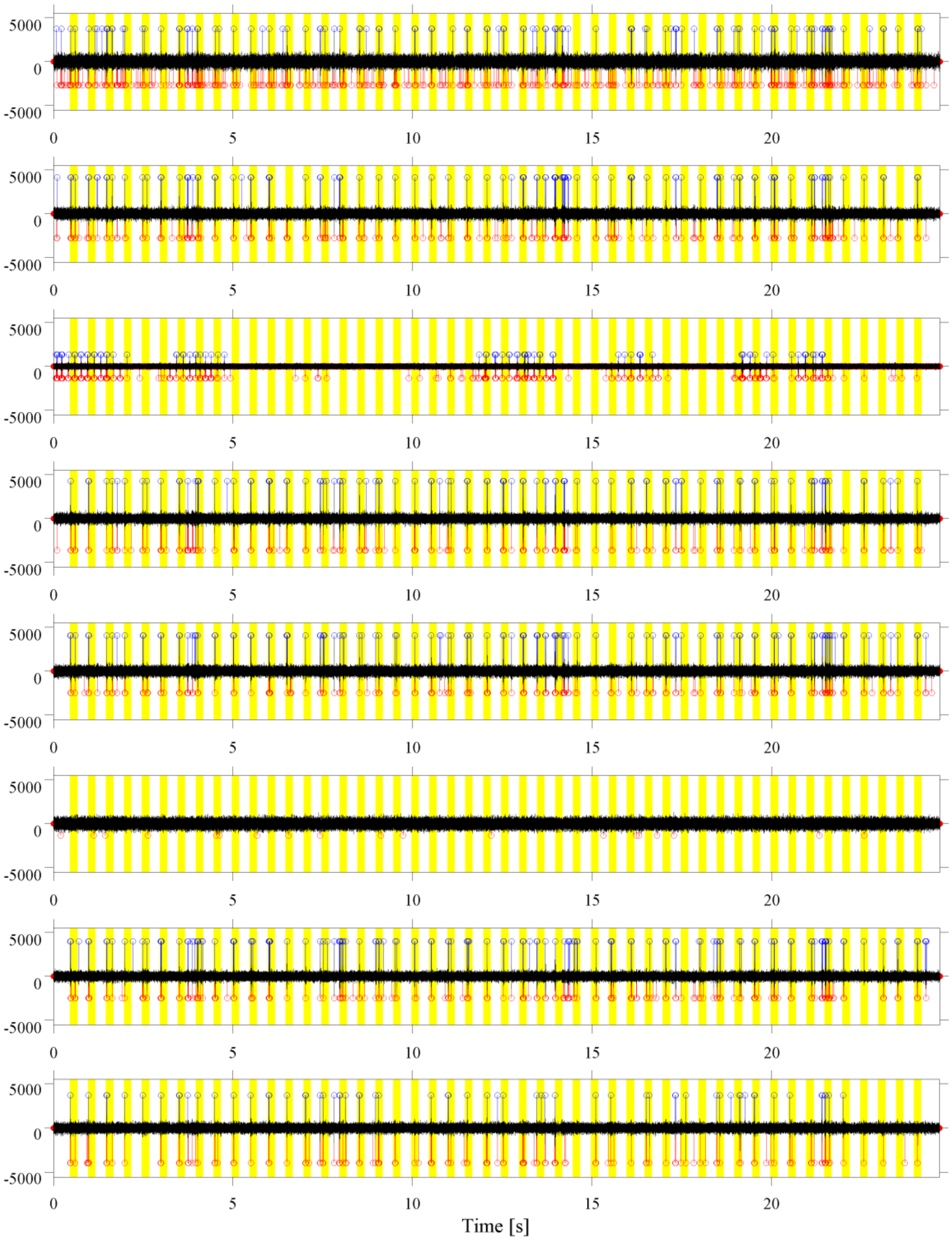

Figure 7-2: Neural recordings from the auditory cortex of a guinea pig taken with a silicon-based neural probe (channels 9-16). The stimulus periods are highlighted in yellow. Action potentials detected using the thresholding technique are shown with blue stems. Action potentials detected using the CWT method are shown with red stems.

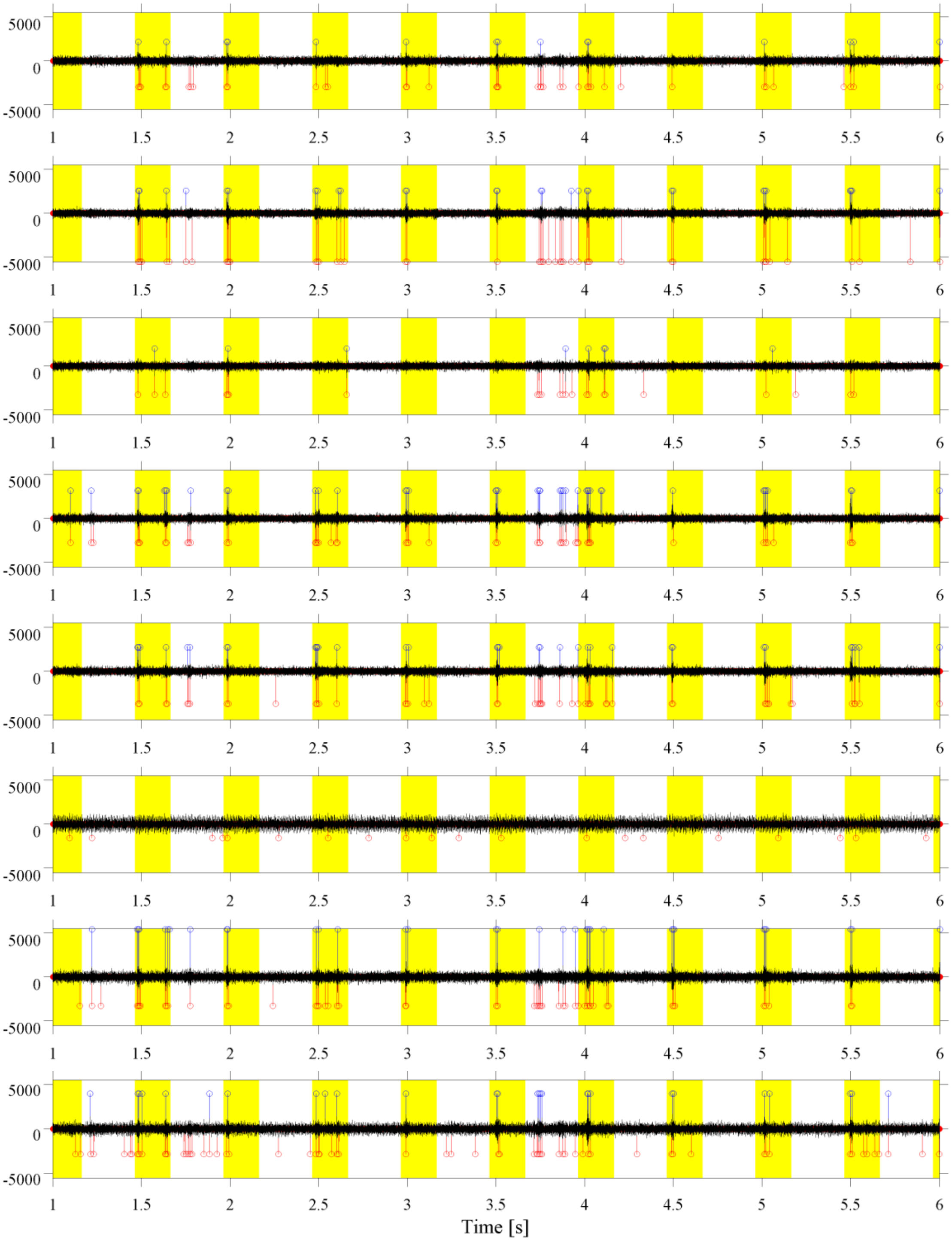

Figure 7-3: Expanded, 5-second view of neural recordings from the auditory cortex of a guinea pig taken with a silicon-based neural probe (channels 1-8) from Fig. 7-1. The stimulus periods are highlighted in yellow. Action potentials detected using the thresholding technique are shown with blue stems. Action potentials detected using the CWT method are shown with red stems.

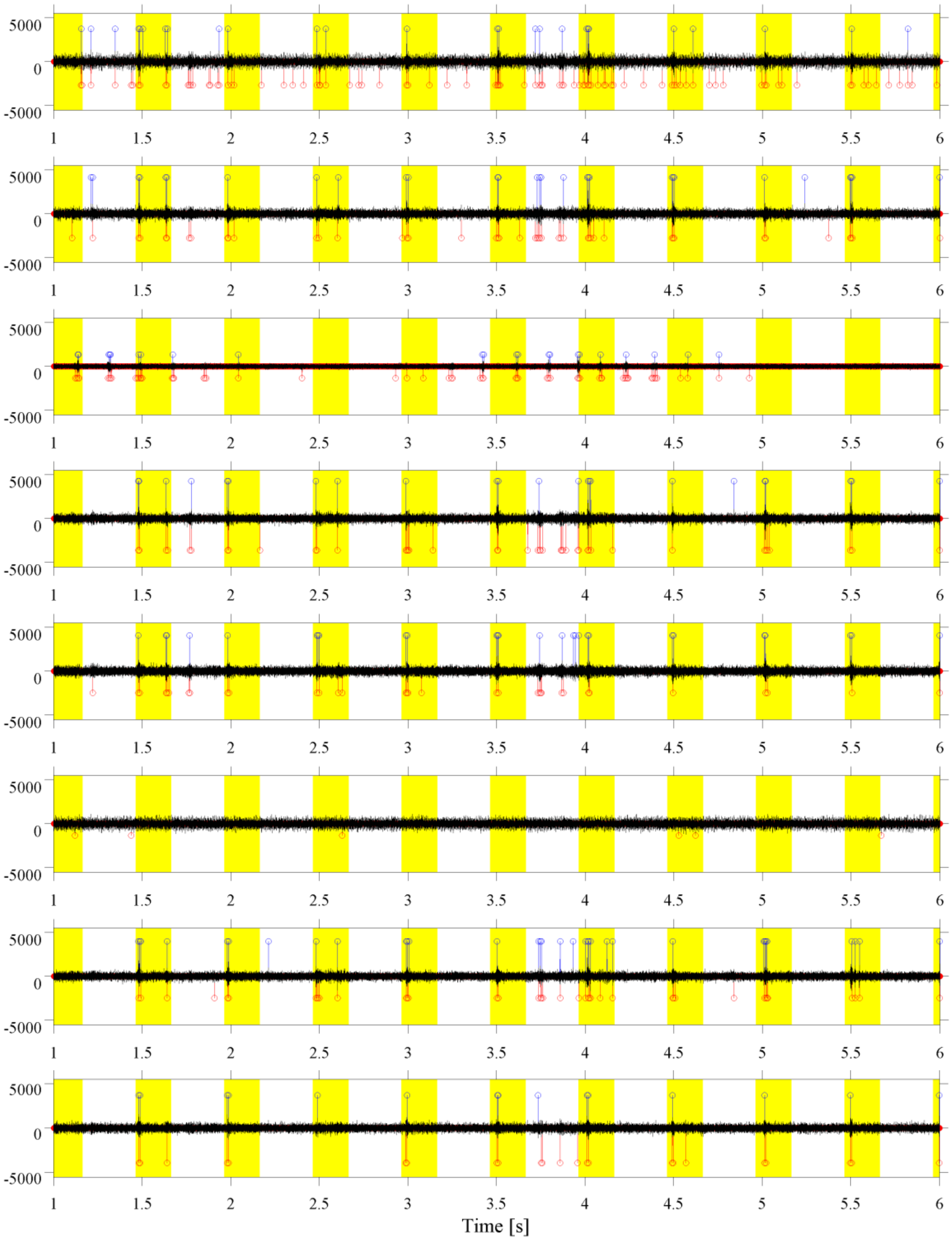

Figure 7-4: Expanded, 5-second view of neural recordings from the auditory cortex of a guinea pig taken with a silicon-based neural probe (channels 9-16) from Fig. 7-2. The stimulus periods are highlighted in yellow. Action potentials detected using the thresholding technique are shown with blue stems. Action potentials detected using the CWT method are shown with red stems.

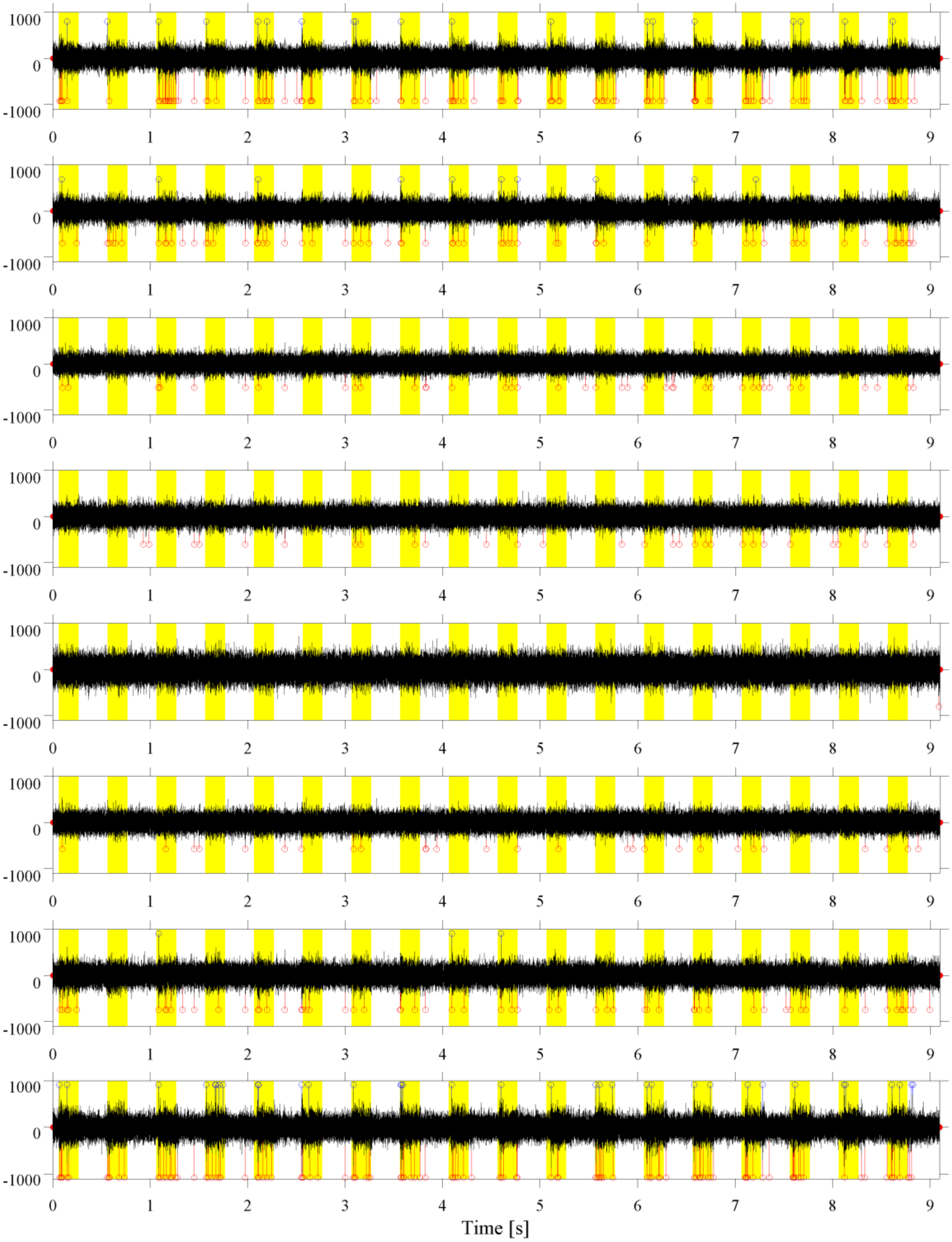

Figure 7-5: Neural recordings from the auditory cortex of a guinea pig taken with a diamond-based neural probe (channels 1-8). The stimulus periods are highlighted in yellow. Action potentials detected using the thresholding technique are shown with blue stems. Action potentials detected using the CWT method are shown with red stems.

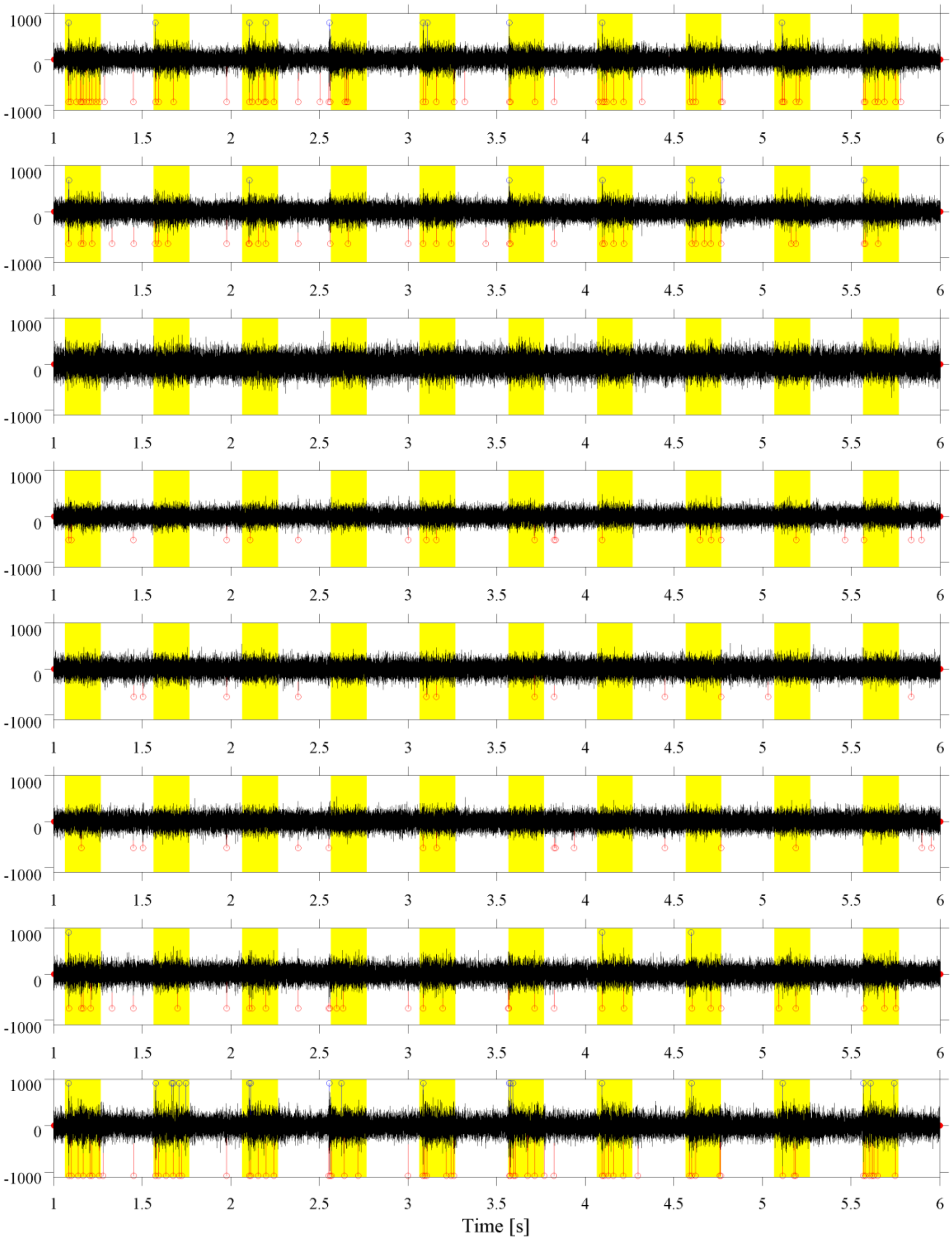

Figure 7-6: Expanded, 5-second view of neural recordings from the auditory cortex of a guinea pig taken with a diamond-based neural probe (channels 1-8) from Fig. 7-5. The stimulus periods are highlighted in yellow. Action potentials detected using the thresholding technique are shown with blue stems. Action potentials detected using the CWT method are shown with red stems.

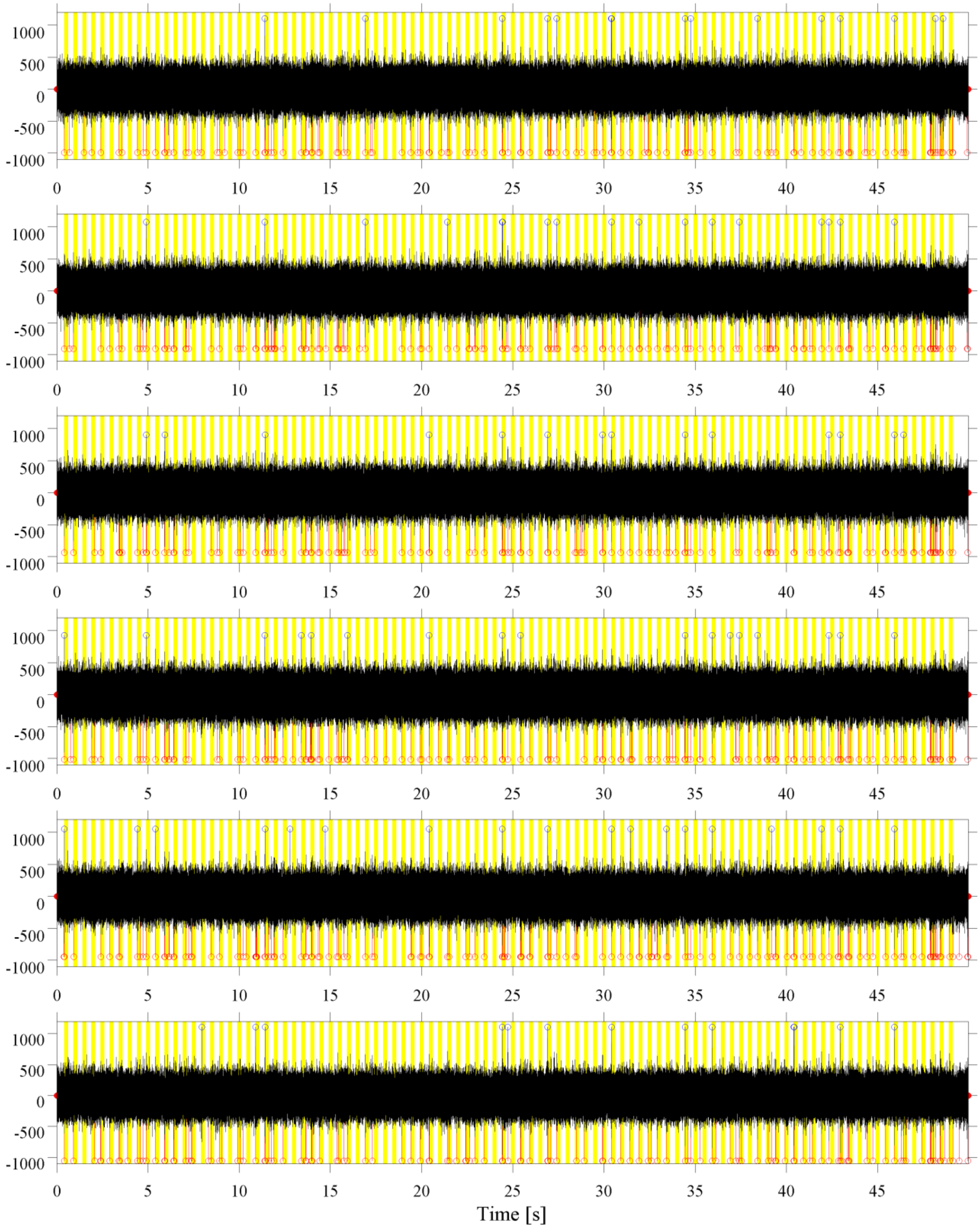

Figure 7-7: Neural recordings from the auditory cortex of a guinea pig taken with a single-material diamond neural probe (channels 1-6). The stimulus periods are highlighted in yellow. Action potentials detected using the thresholding technique are shown with blue stems. Action potentials detected using the CWT method are shown with red stems.

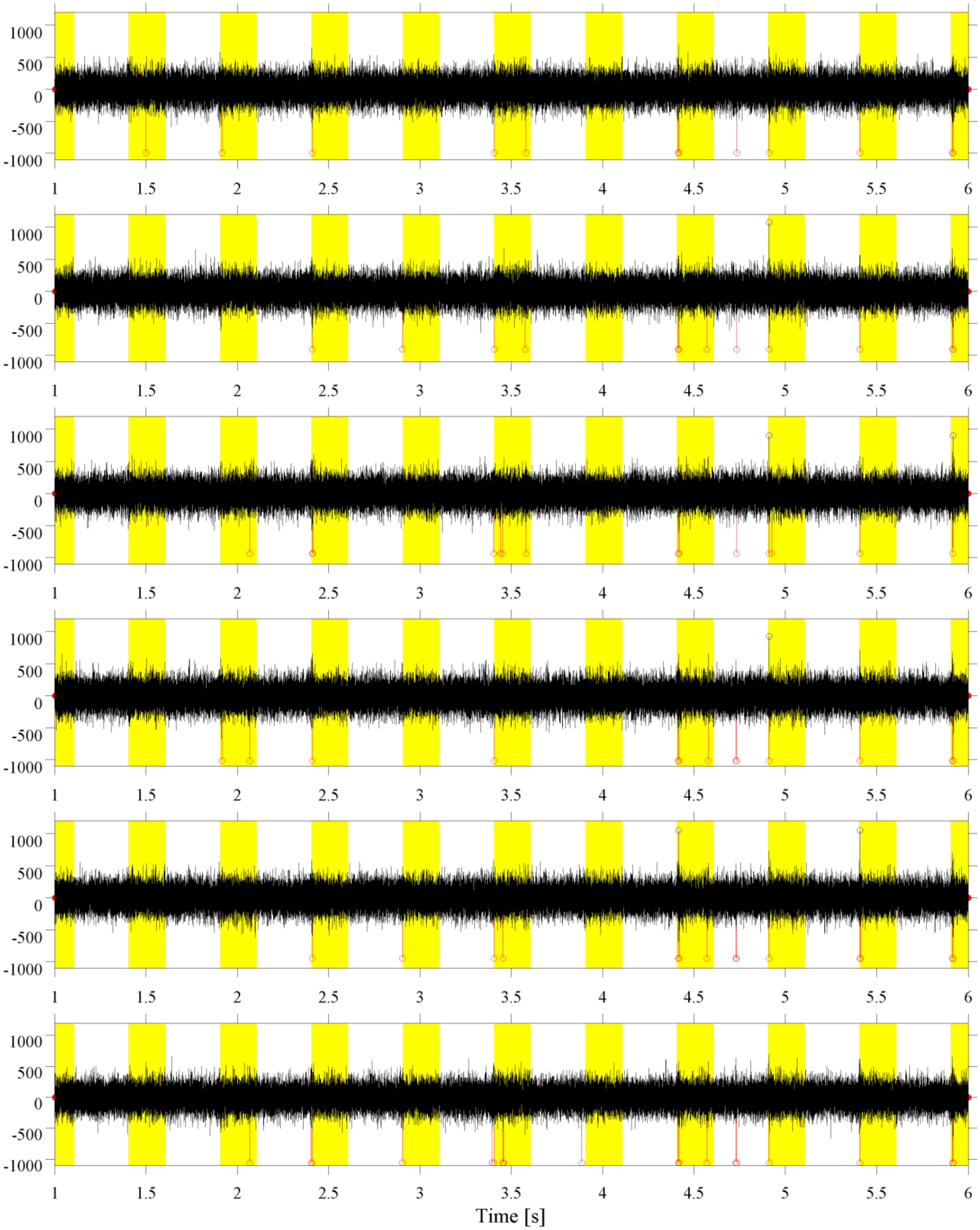

Figure 7-8: Expanded, 5-second view of neural recordings from the auditory cortex of a guinea pig taken with a single-material diamond neural probe (channels 1-6) from Fig. 7-7. The stimulus periods are highlighted in yellow. Action potentials detected using the thresholding technique are shown with blue stems. Action potentials detected using the CWT method are shown with red stems.

Several observations can be made from Figs. 7-1 through 7-8. It is evident from the recordings that the SNR is different between probe types. The silicon-based probes have the highest SNR, while the single-material diamond probes have the lowest SNR. It can also be seen that several electrodes do not have any discernible signal on the silicon-based probe and the diamond-based probe. It can be seen that the number of detections is higher using the CWT method for all of the probe types. Both the basic thresholding and CWT methods appear to detect action potentials both during stimulus and outside of stimulus. It is not apparent whether a higher percentage of detections occur within stimulus for the thresholding or CWT method. In order to determine how each of the methods affects the number of detections within stimulus and the arrival times relative to the onset of stimulus, the histograms of arrival times are required. Figs. 7-9 and 7-10 show the histograms of spike arrival times relative to the onset of stimulus using the basic thresholding method for each of the electrodes on the silicon-based neural probe. Fig. 7-11 shows the histogram of spike arrival times relative to onset of stimulus using the basic thresholding method for the diamond-based neural probes. Fig. 7-12 shows the histogram of action potential arrival times relative to the onset of stimulus using the basic thresholding technique for the single-material diamond neural probes. Figs. 7-13 and 7-14 show the histograms of event arrival times relative to the onset of stimulus using the CWT method for the silicon-based neural probe. Fig 7-15 shows the histogram of arrival times relative to the onset of stimulus using the CWT method for the diamond-based neural probe. Fig 7-16 shows the histogram of event arrival times relative to the onset of stimulus using the CWT method for the single-material diamond neural probe.

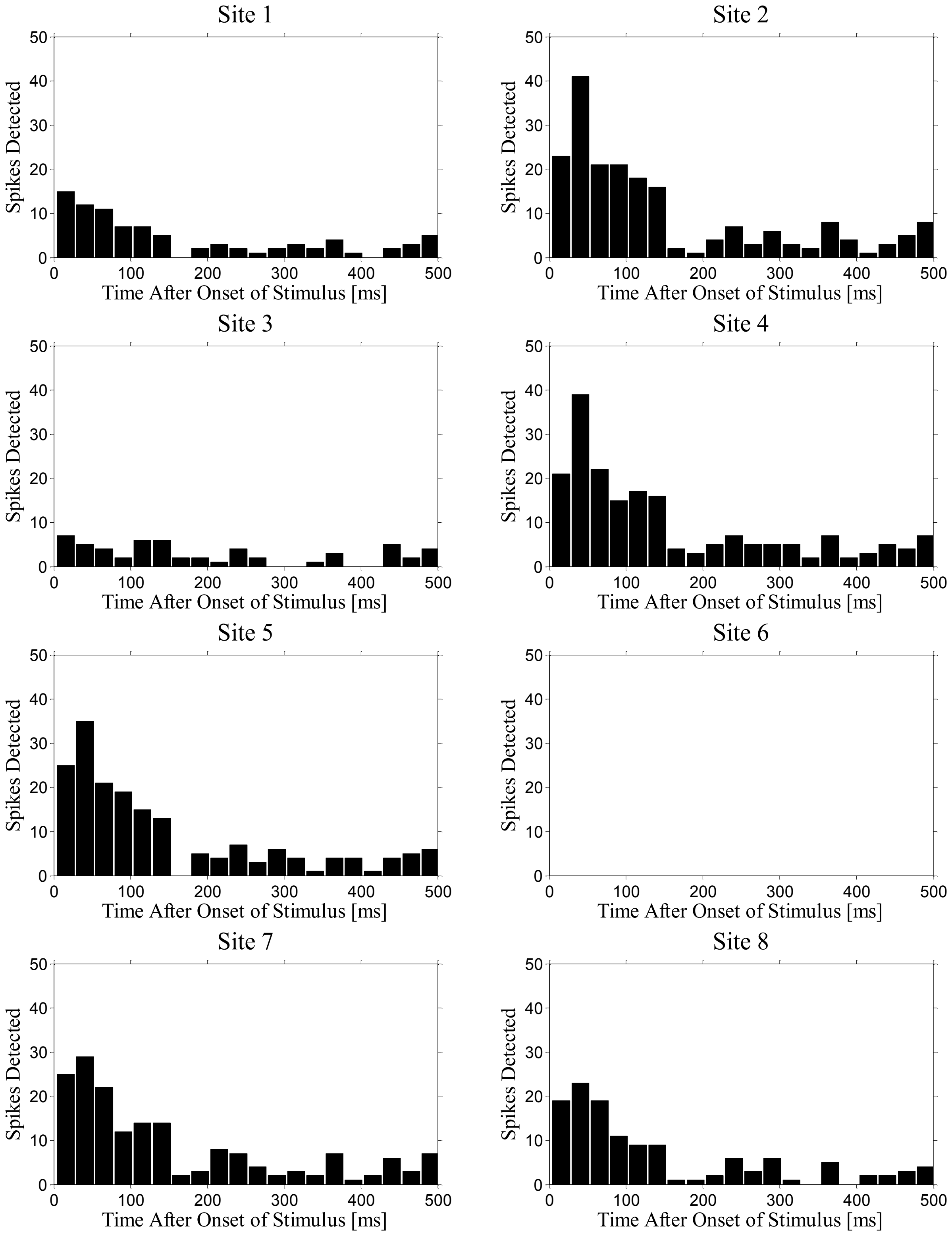

Figure 7-9: Histograms showing threshold-detected action potential times relative to the onset of stimulus for a silicon-based neural probe with iridium oxide electrodes. Electrodes 1 – 8.

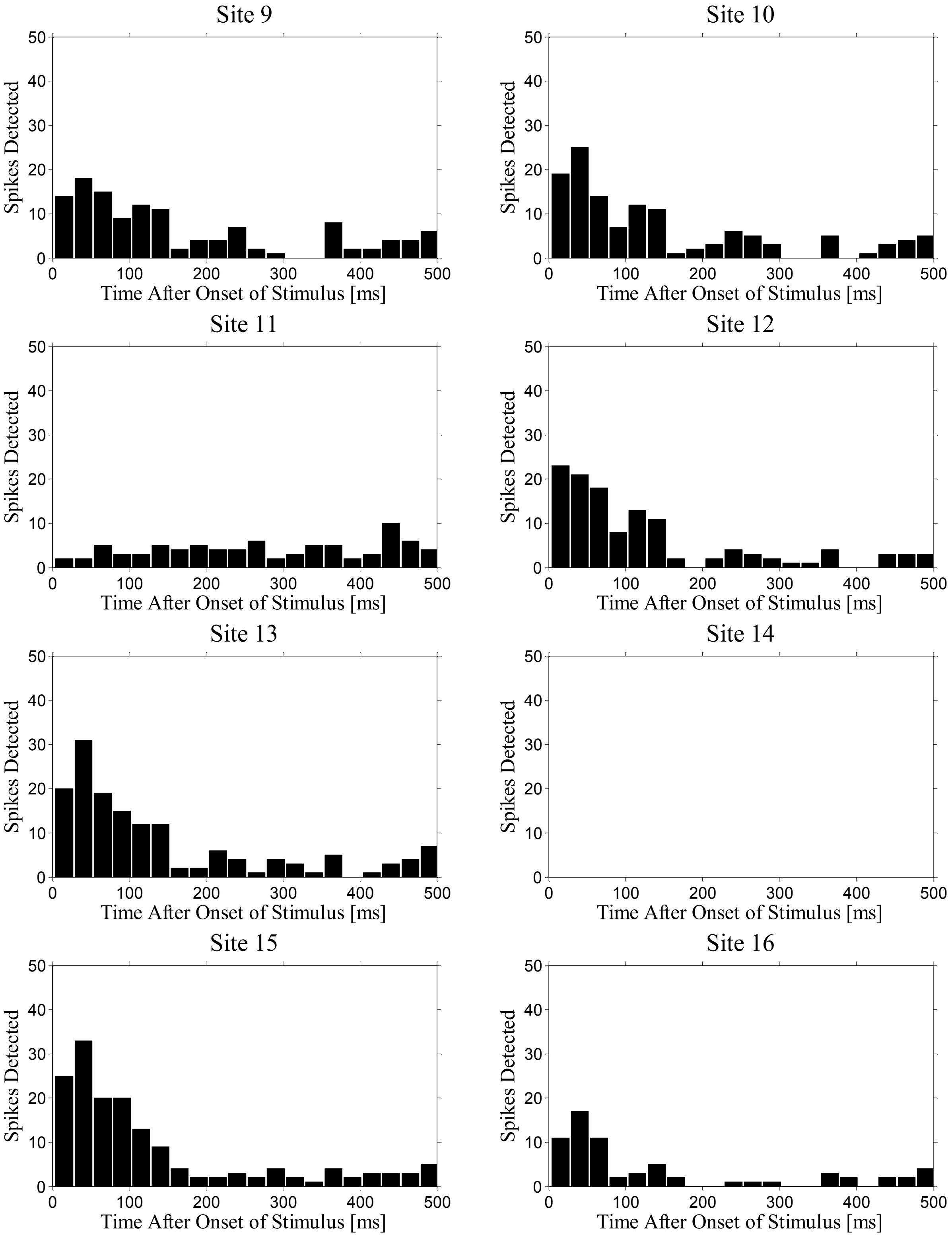

Figure 7-10: Histograms showing threshold-detected action potential times relative to the onset of stimulus for a silicon-based neural probe with iridium oxide electrodes. Electrodes 9 – 16.

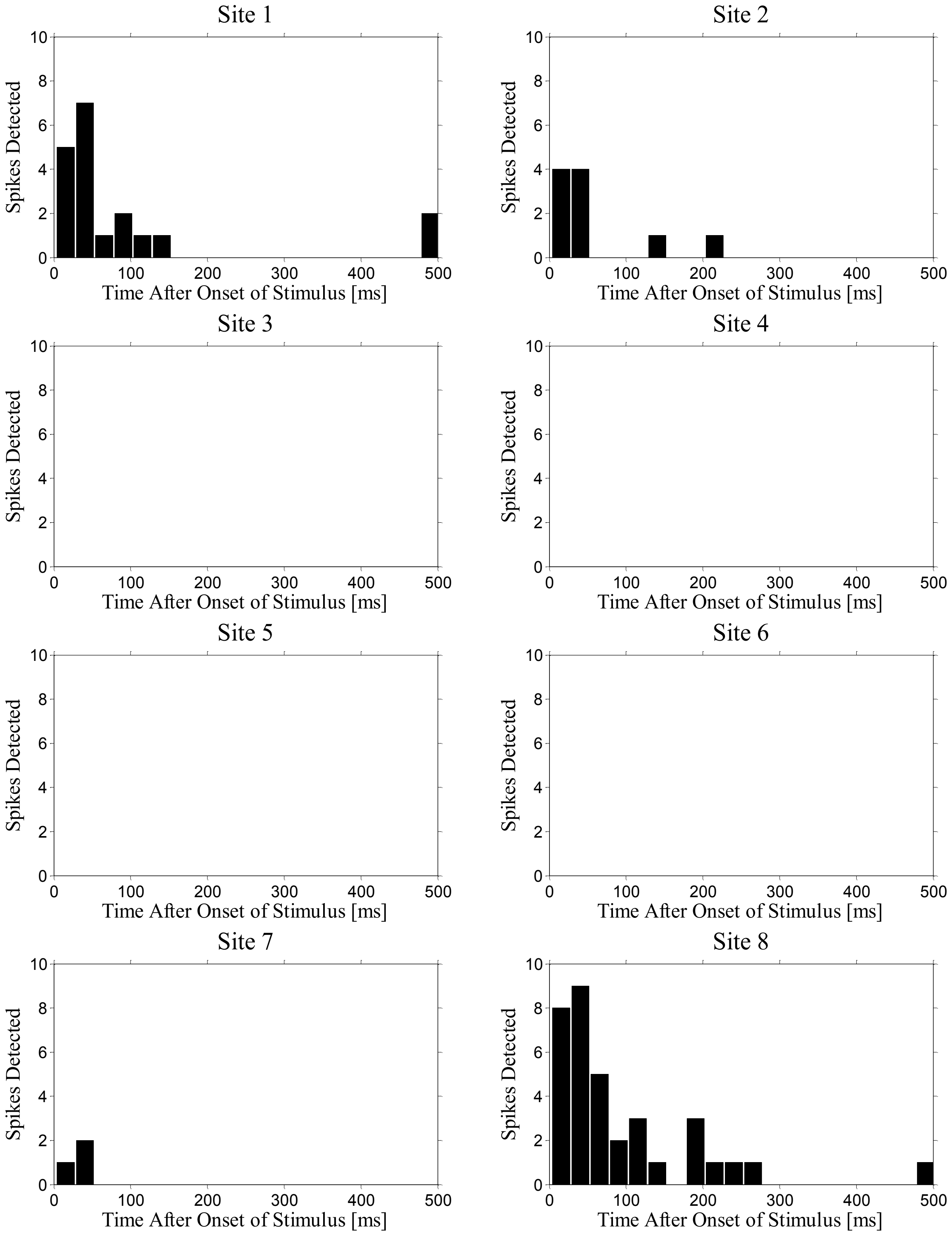

Figure 7-11: Histograms showing threshold-detected action potential times relative to the onset of stimulus for a diamond-based neural probe with boron-doped-diamond electrodes.

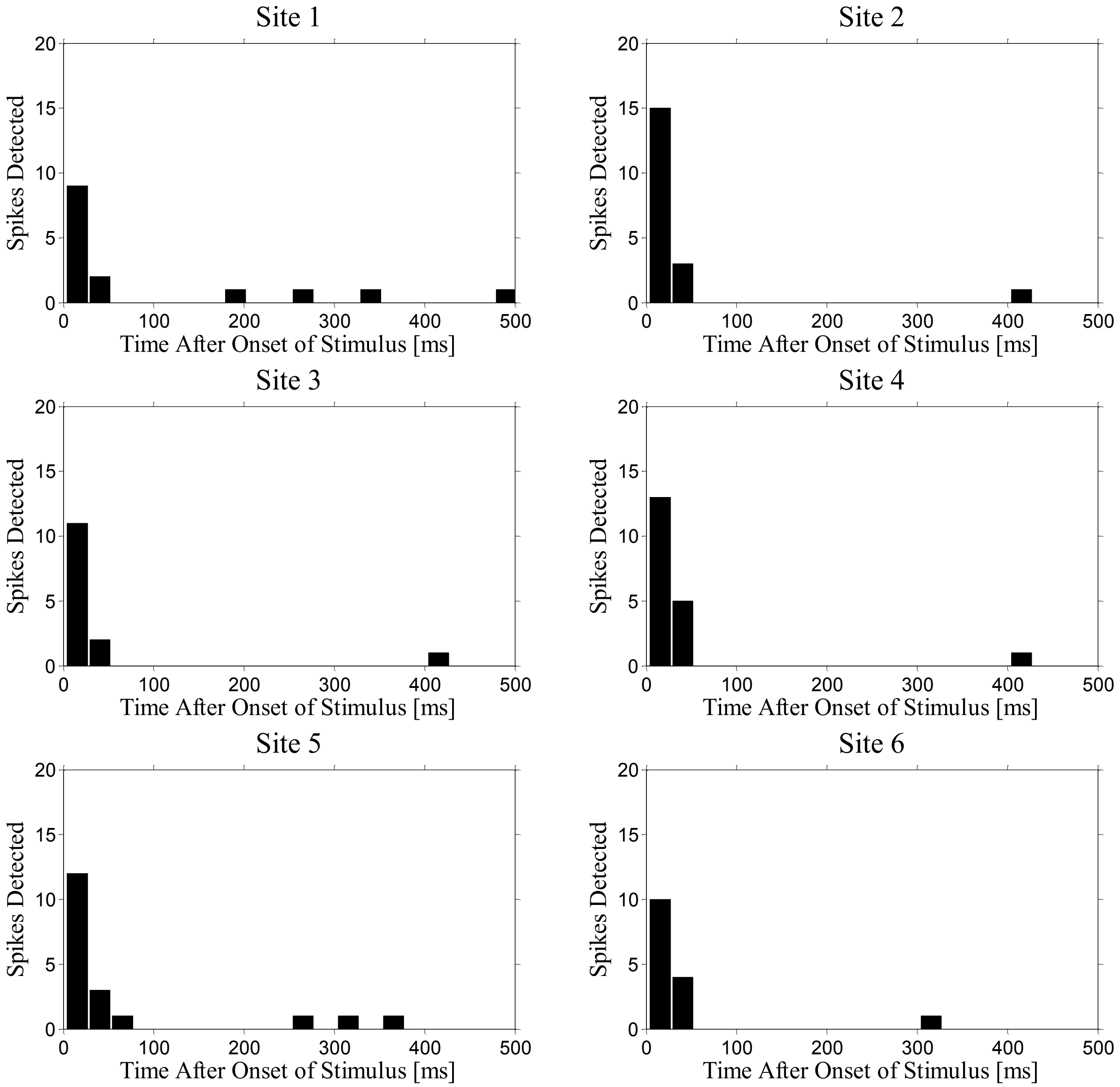

Figure 7-12: Histograms showing threshold-detected action potential times relative to the onset of stimulus for a single-material neural probe with boron-doped-diamond electrodes.

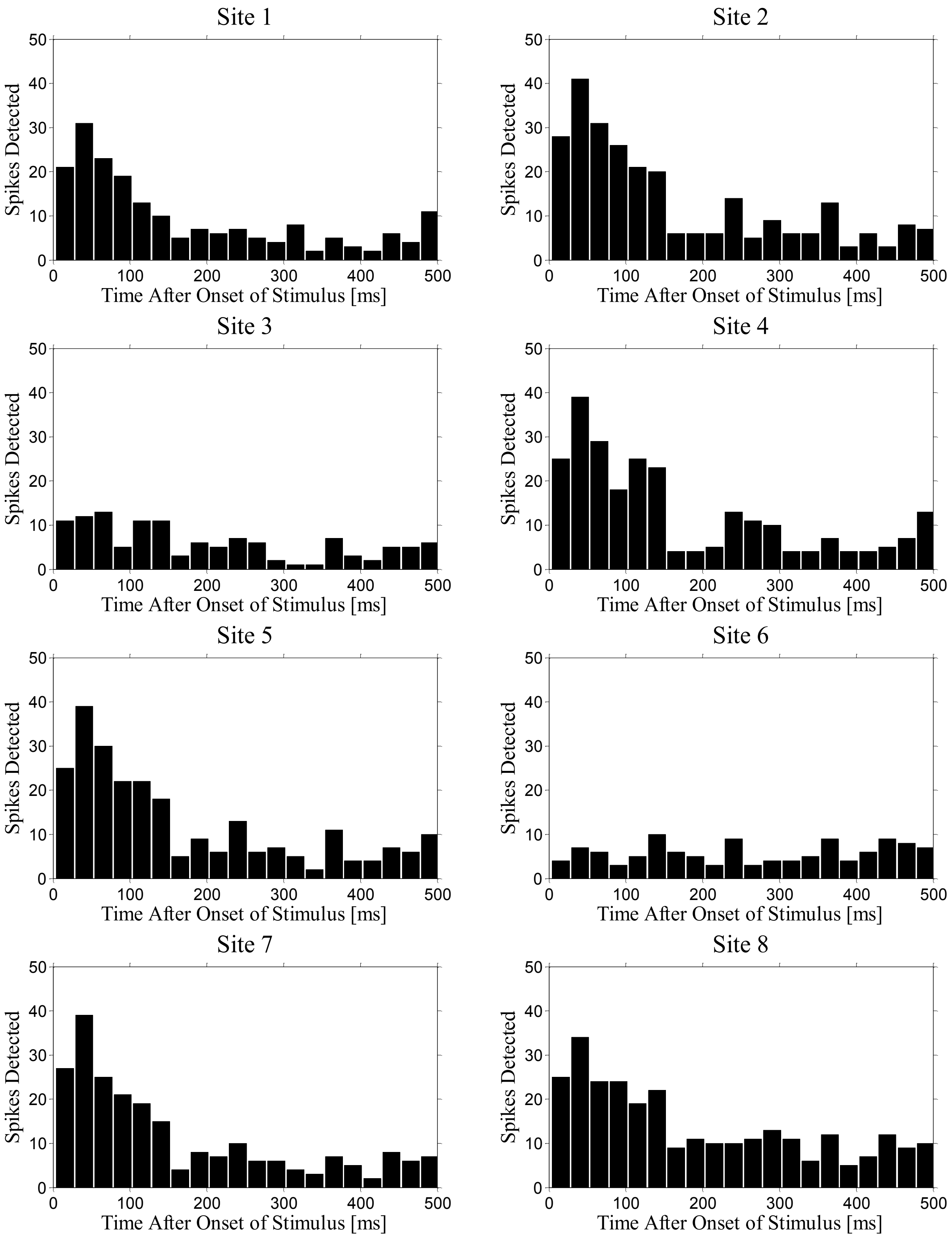

Figure 7-13: Histograms showing CWT-detected action potential times relative to the onset of stimulus for a silicon-based neural probe with iridium oxide electrodes. Electrodes 1 – 8.

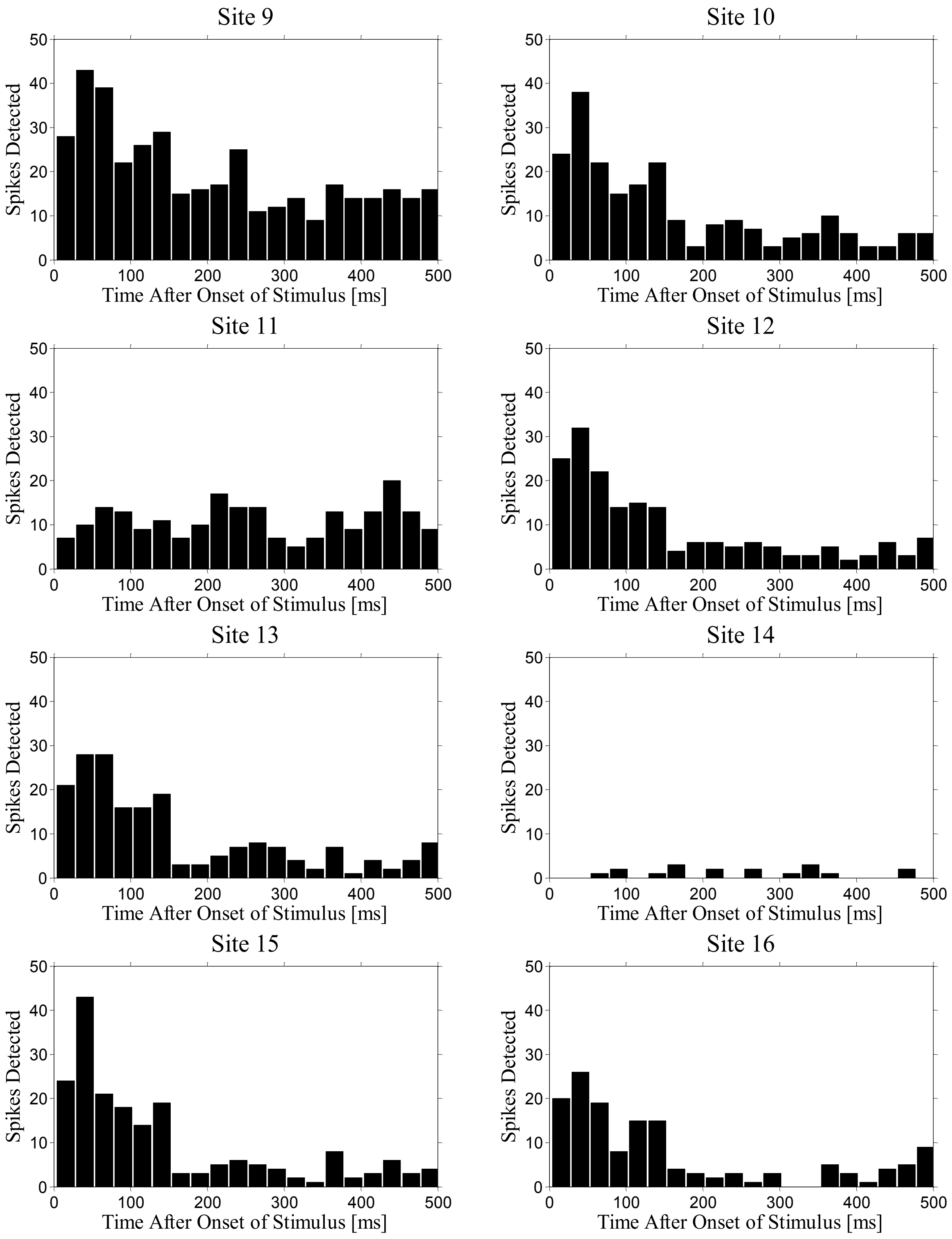

Figure 7-14: Histograms showing CWT-detected action potential times relative to the onset of stimulus for a silicon-based neural probe with iridium oxide electrodes. Electrodes 9 – 16.

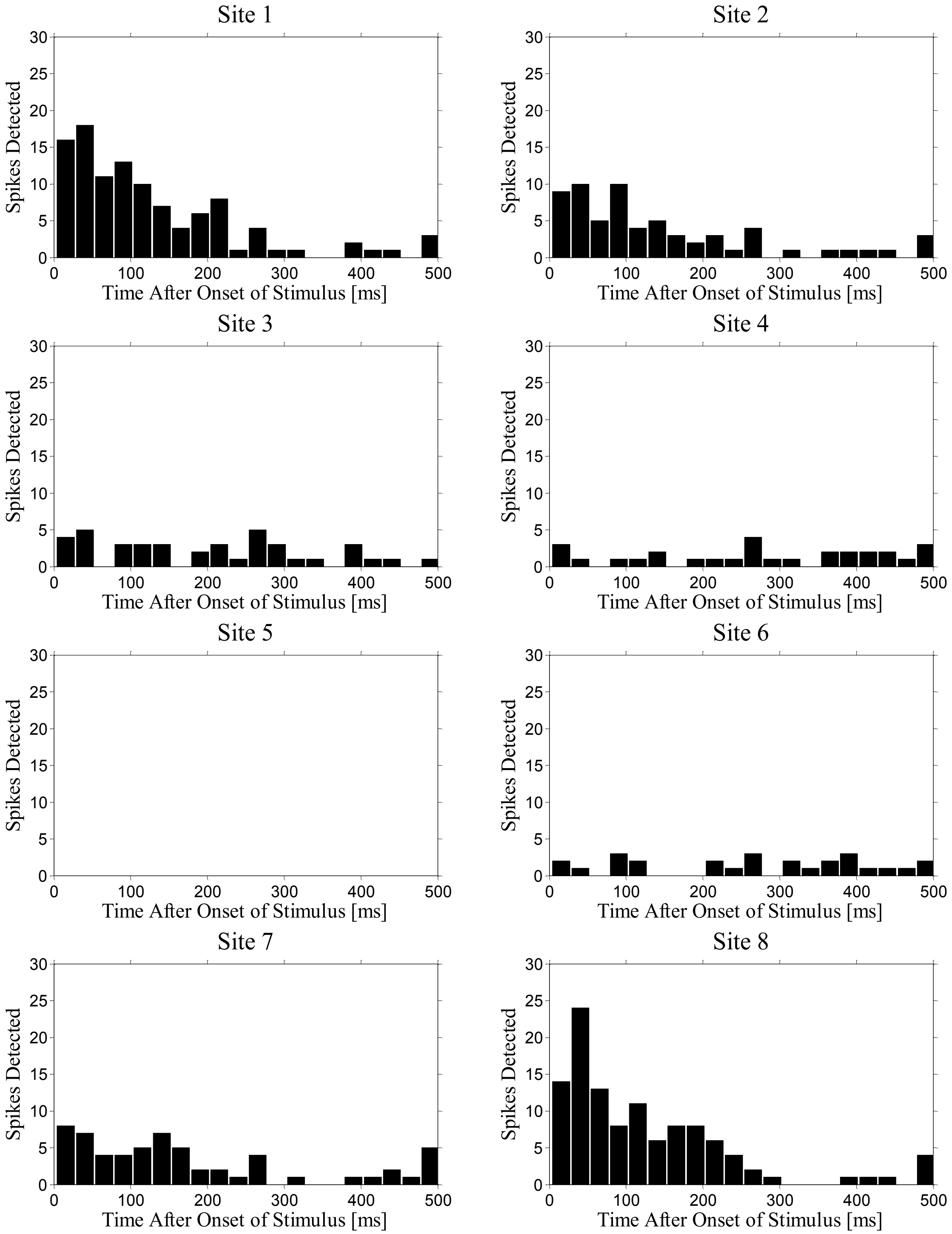

Figure 7-15: Histograms showing CWT-detected action potential times relative to the onset of stimulus for a diamond-based neural probe with boron-doped-diamond electrodes.

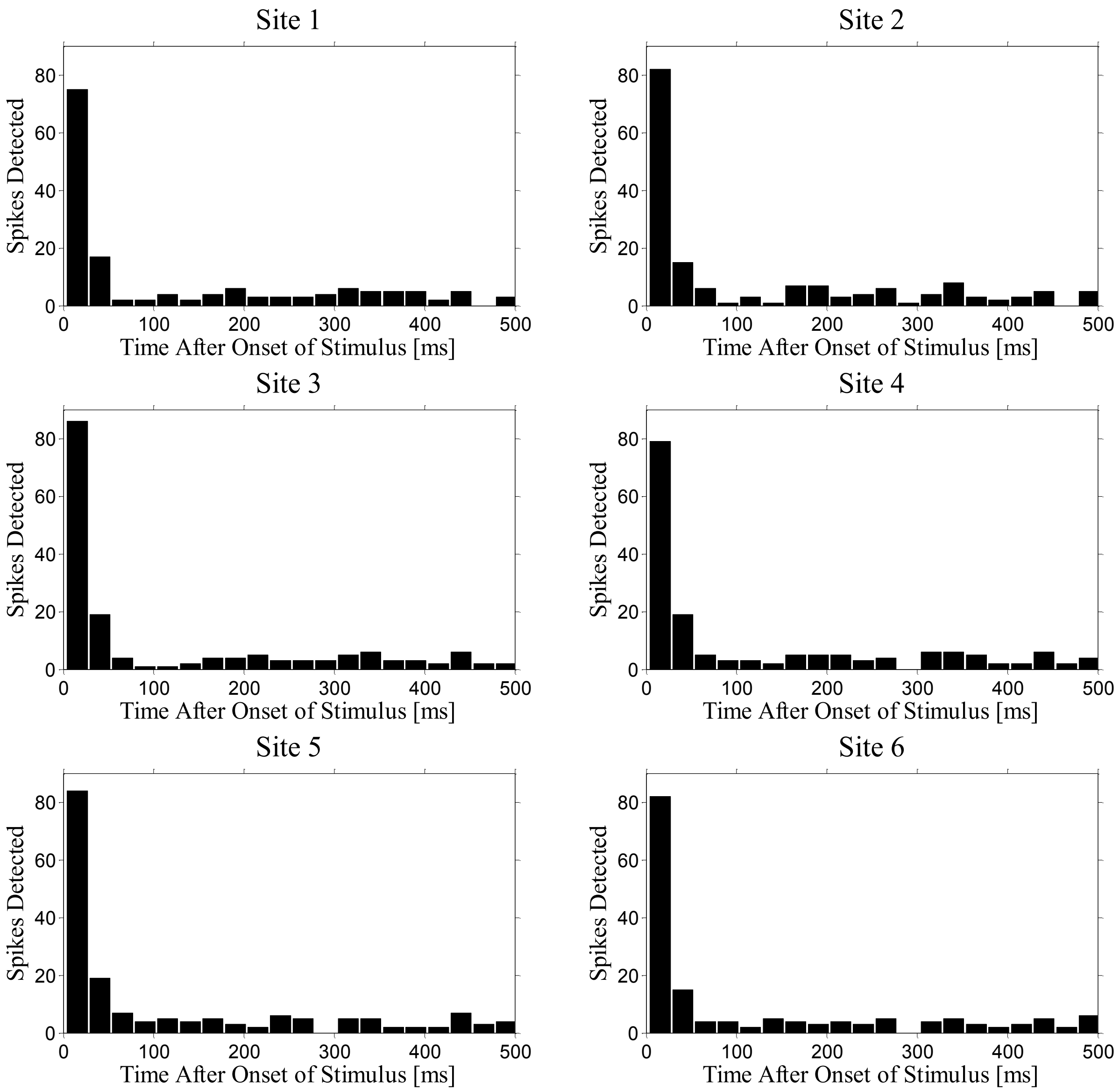

Figure 7-16: Histograms showing CWT-detected action potential times relative to the onset of stimulus for a single-material neural probe with boron-doped-diamond electrodes.

The expected result from this experiment is to see increased neural activity during stimulus (0 – 200 ms), with a peak toward the beginning of the stimulus period. From Figs 7-9 and 7-10, it can be seen that using the basic thresholding technique we can strongly see the expected result on electrodes 2, 4, 5, 7, 8, 10, 12, 13, and 15 of the silicon-based neural probe. On electrodes 1, 9, and 16 we can see a trend showing a higher firing rate near the onset of stimulus, but the results are not as strong as the other electrodes. Electrodes 3, 6, 11, and 14 show no correlation to the expected result. From Figs. 7-13 and 7-14, it can be seen that the CWT method results in a strong correlation to the expected result on electrodes 1, 2, 4, 5, 7, 8, 9, 10, 12, 13, 15, and 16. Electrodes 6, 11, and 14 still show no correlation to the expected result, but electrode 3 bears a weak correlation to the expectation. For the silicon-based probe, the CWT detection method outperforms the basic thresholding method because several electrodes give results that are closer to what is expected. This can be more clearly seen in Figs. 7-17 and 7-18 which show combined histograms for the thresholding and CWT detection methods using the silicon-based neural probe. In the histograms, the number of detections by thresholding are shown by the blue (darker) bars, while the number of detection by CWT are shown by the cyan (lighter) bars. Figs. 7-17 and 7-18 show that the CWT detection method not only results in more action potentials being detected, but also in the results aligning more with the expected results for the experiment. Even though the silicon-based probe recordings do not suffer from poor SNR, they still appear to benefit from using the CWT detection method.

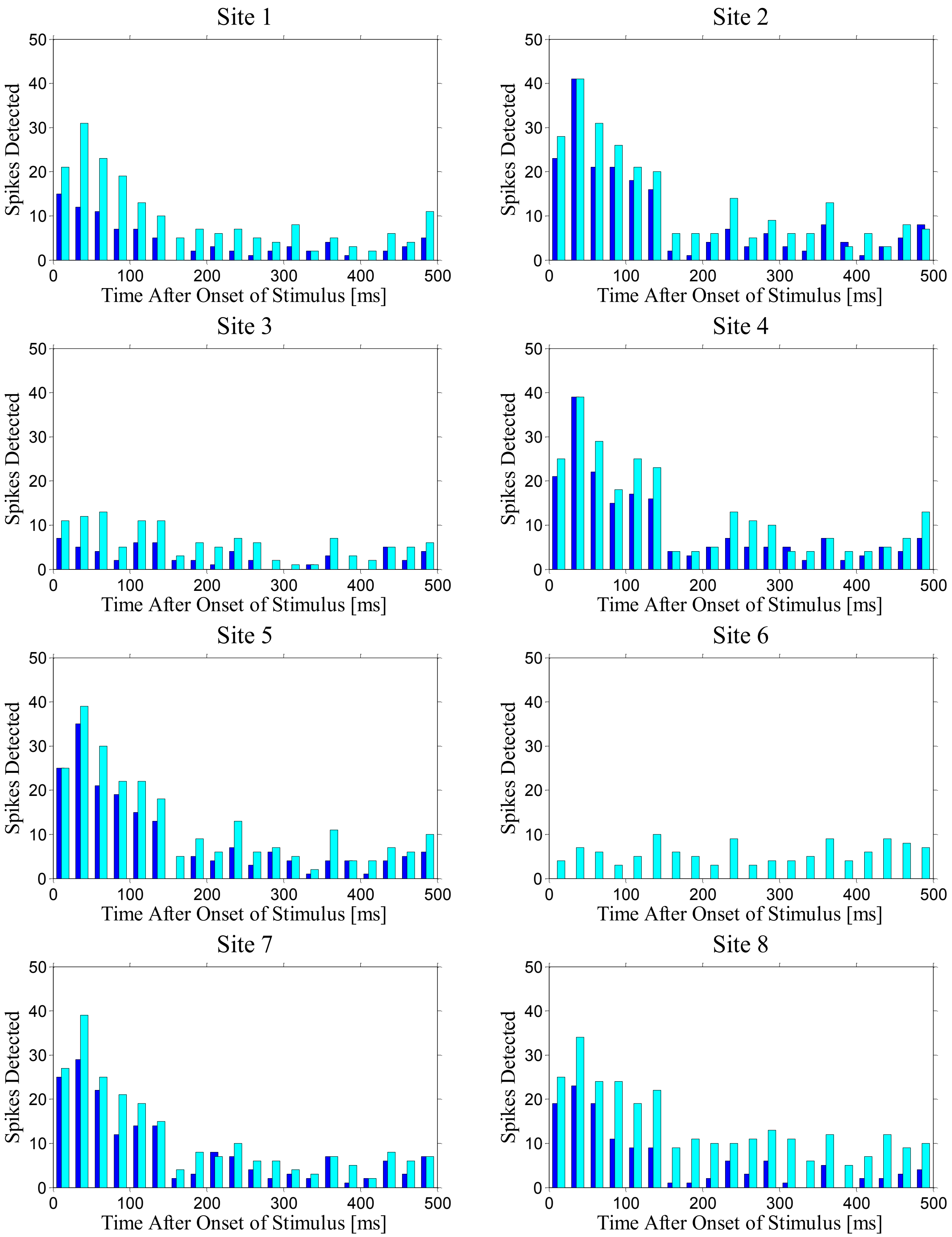

Figure 7-17: Histograms comparing detection using the thresholding method and the CWT method for a silicon-based neural probe with iridium oxide electrodes. Electrodes 1 – 8. The number of detected action potential times relative to the onset of stimulus is shown for thresholding in blue (darker) and for CWT in cyan (lighter).

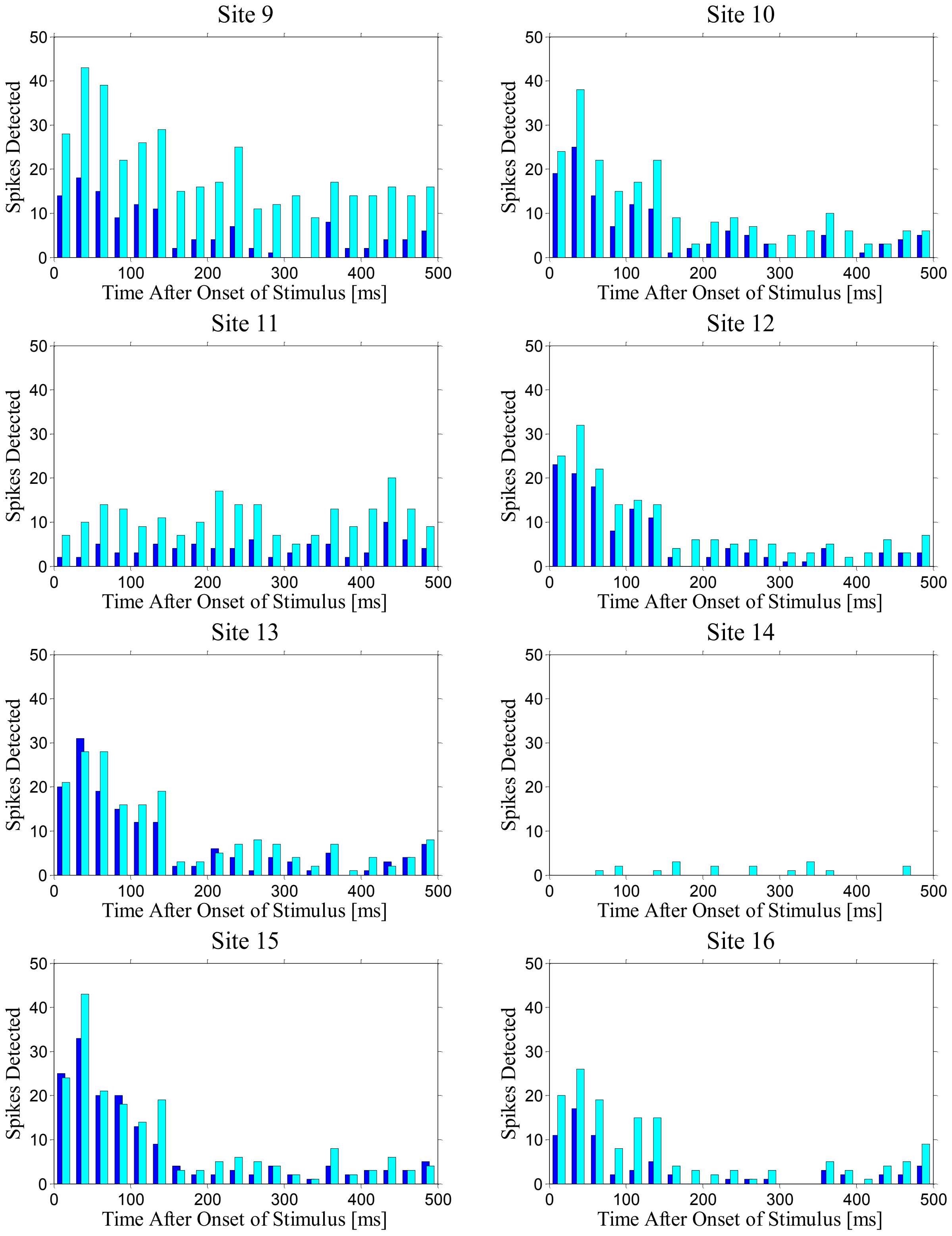

Figure 7-18: Histograms comparing detection using the thresholding method and the CWT method for a silicon-based neural probe with iridium oxide electrodes. Electrodes 9 – 16. The number of detected action potential times relative to the onset of stimulus is shown for thresholding in blue (darker) and for CWT in cyan (lighter).

Fig. 7-11 shows that using the basic thresholding technique we can see a correlation to the expected result on electrodes 1 and 8 on the diamond-based neural probe. On electrodes 2 and 7, there may be a correlation, but not enough action potentials were detected. Electrodes 3, 4, 5, and 6 show no action potentials being detected. From Fig. 7-15, it can be seen that the CWT method results in a strong correlation to the expected result on electrodes 1, 2, and 8. Electrodes 3, 4, 5, and 6 still show no correlation to the expected result, but electrode 7 shows some correlation to the expectation. For the diamond-based probe, the CWT detection method outperforms the basic thresholding method because the detection rate is much higher and results that are closer to expectations. This can be clearly seen in Fig. 7-19, which shows the combined histograms for thresholding and CWT detection methods using the diamond-based neural probe. In the histograms, the number of detections by thresholding are shown by the blue (darker) bars, while the number of detection by CWT are shown by the cyan (lighter) bars. Fig. 7-19 shows that the CWT detection method results in more than twice as many action potentials being detected, and also the results more closely reflect the expected results for the experiment. As expected, the poor SNR of the diamond-based neural probe is significantly affected by the CWT detection method.

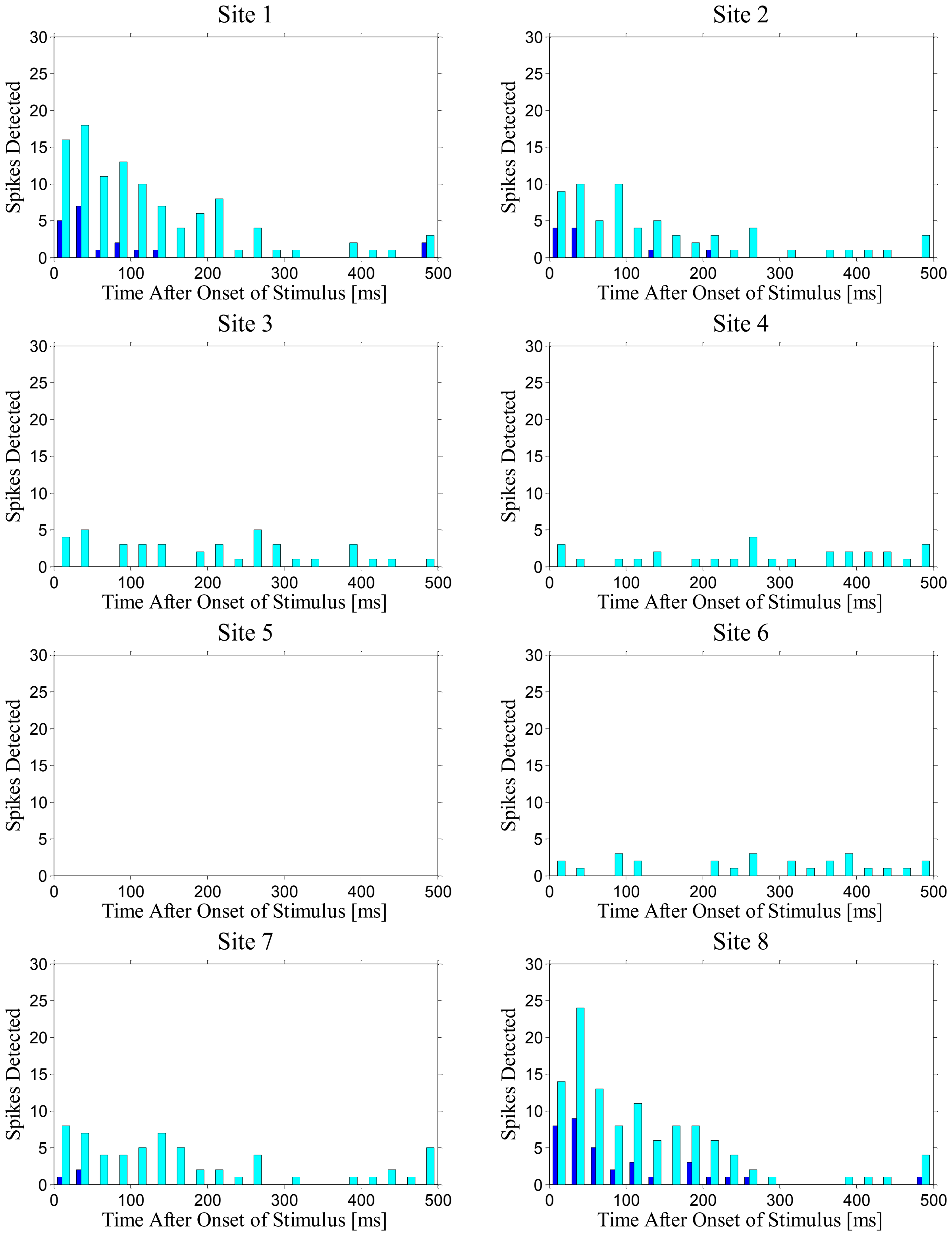

Figure 7-19: Histograms comparing detection using the thresholding method and the CWT method for a diamond-based neural probe with boron-doped-diamond electrodes. The number of detected action potential times relative to the onset of stimulus is shown for thresholding in blue (darker) and for CWT in cyan (lighter).

Fig. 7-12 shows the results from the single-material diamond neural probe using the basic thresholding technique. It can be seen that all of the electrodes have comparable performance. As expected there is a sharp rise in neural activity shortly after the onset of stimulus. However, after the initial increase in activity, there is no increase in activity during the remainder of the stimulus, as expected. It is not clear why there is a lack of activity during the remainder of the stimulus. From Fig. 7-16, it can be seen that the CWT method results in many more detected action potentials than the thresholding method. However, there is still an inexplicable lack of increased activity during the stimulus other than immediately after the onset of stimulus. For the diamond-based probe, the CWT detection method outperforms the basic thresholding method because the detection rate is much higher. This can be clearly seen in Fig. 7-20, which shows the combined histograms for thresholding and CWT detection methods using the single-material diamond neural probe. In the histograms, the number of detections by thresholding are shown by the blue (darker) bars, while the number of detection by CWT are shown by the cyan (lighter) bars. Fig. 7-20 shows that the CWT detection method results in more than five times as many action potentials being detected. As expected, the very poor SNR of the single-material diamond neural probe is significantly affected by the CWT detection method.

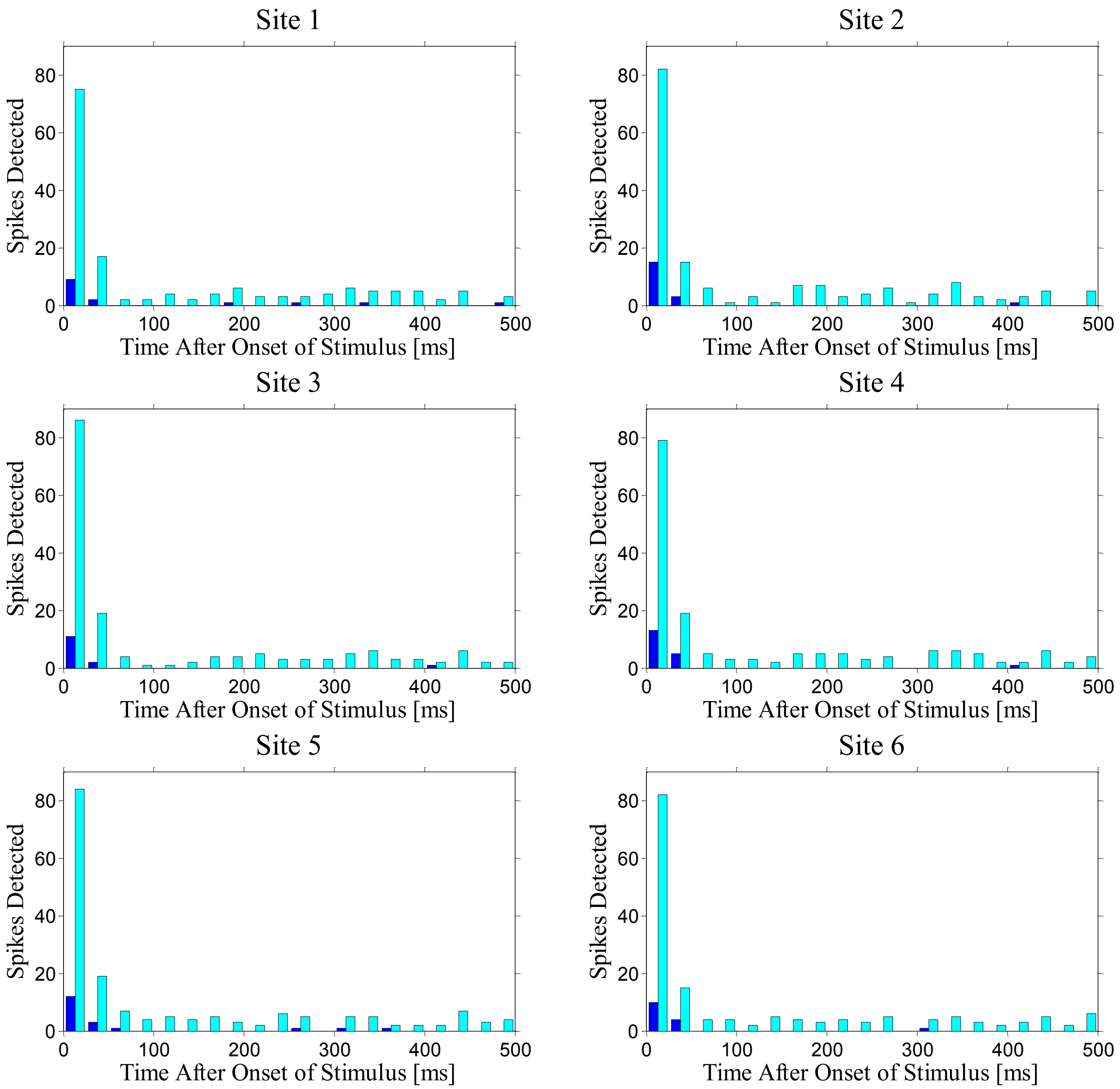

Figure 7-20: Histograms comparing detection using the thresholding method and the CWT method for a single-material diamond neural probe with boron-doped-diamond electrodes. The number of detected action potential times relative to the onset of stimulus is shown for thresholding in blue (darker) and for CWT in cyan (lighter).

The CWT detection method provides benefits to all three of the probe types that were used in this experiment. For the silicon-based neural probe, the CWT method allows more action potentials to be detected and improves the results of several electrodes that had lower SNR. For the diamond-based neural probe, the CWT more than doubled the number of action potentials detected and doubled the number of viable electrodes. For the single-material diamond neural probe, the CWT method increased the number of detected action potentials by more than five-fold. In order to directly compare the benefits to using the CWT method over the basic thresholding method for the three probe types, the results were averaged for all of the good electrodes on each probe. Electrodes which showed little or no correlation to the stimulus were ignored (electrodes 3, 4, 5, and 6 on the diamond-based probe and electrodes 3, 6, 11, and 14 on the silicon-based probe). In addition, rather than comparing the number of action potentials detected, the rate at which action potentials was detected was compared. This makes a direct comparison much easier as the length of the recordings for each of the probe types was significantly different. The results are presented in Fig. 7-21 showing the average firing rate of detected action potentials across all of the electrodes for each of the probe types. The detected firing rate using the thresholding method is in blue (darker), while the detected firing rate using the CWT method is in cyan (lighter). The top graph shows the results for the silicon-based neural probe with iridium oxide electrodes, the middle shows the results for the diamond-based neural probe with boron-doped-diamond electrodes, and the bottom graph shows the results for the single-material diamond neural probe with boron-doped-diamond electrodes. From Fig. 7-21 it can be seen that using the CWT method instead of the basic thresholding technique results in ~65% more action potentials being detected, with ~50% more being detected during stimulus, for the silicon-based neural probe. For the diamond-based neural probe, ~410% more action potentials are detected, with ~345% more being detected within stimulus, using the CWT technique instead of the thresholding technique. Using the CWT method, rather than thresholding, ~875% more action potentials are detected, with ~700% more detected during stimulus. As expected, using the CWT method instead of the basic thresholding method dramatically improves the detection rate of action potentials, especially when analyzing recordings from the diamond-based and single-material diamond neural probes.

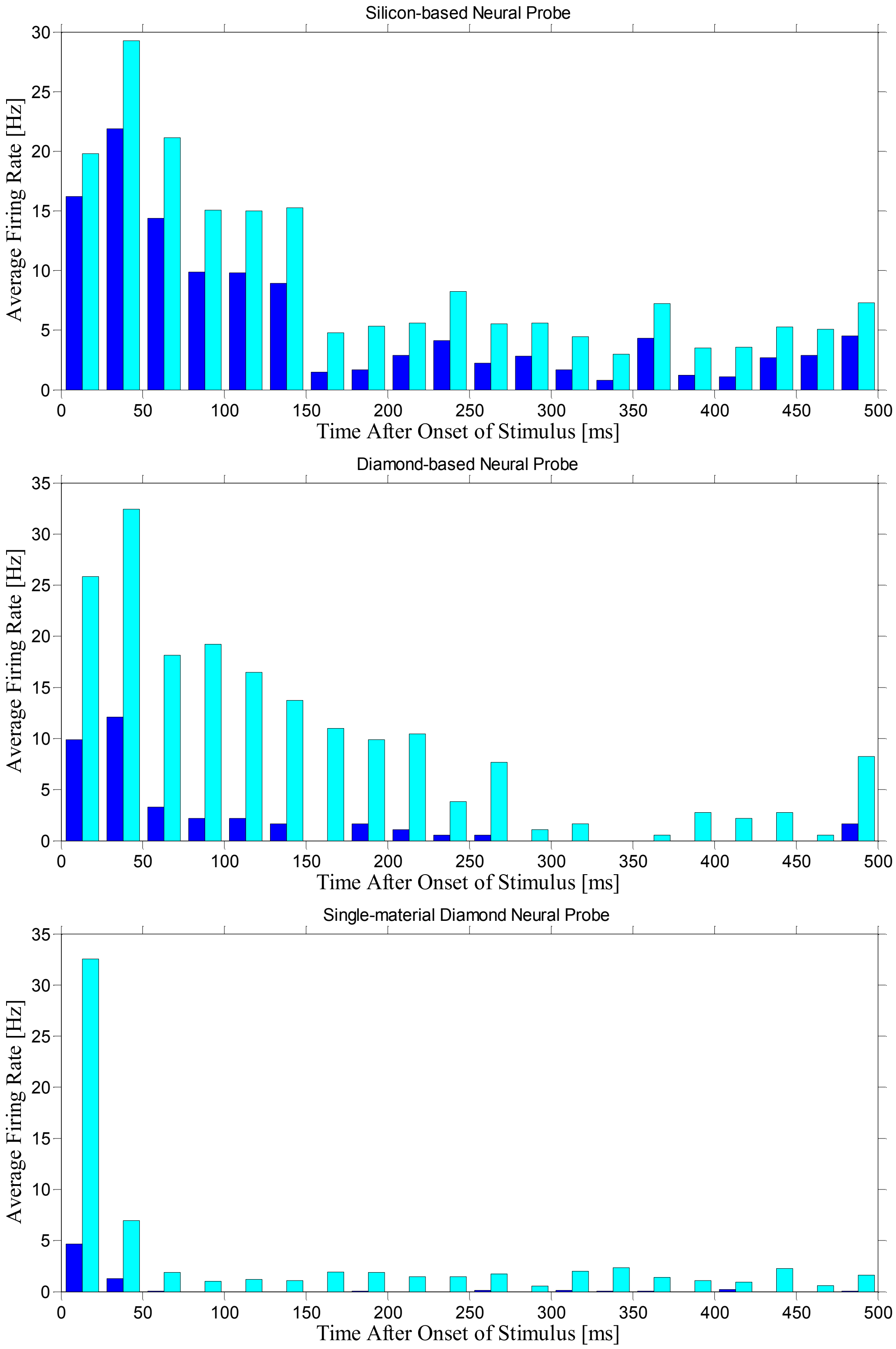

Figure 7-21: Bar graphs comparing average detection rates across all good electrodes using the thresholding method and the CWT method for each probe type. The number of detected action potential times relative to the onset of stimulus is shown for thresholding in blue (darker) and for CWT in cyan (lighter).

The silicon-based neural probe with iridium oxide electrodes is considered sufficient for acute neural recording activities. In order for the diamond-based and single-material diamond neural probes to be considered effective for acute neural recordings, their performance must be comparable to that of the silicon-based probe. The performance will be measured using three variables: the peak average-detection-rate shortly after the onset of stimulus, the average detection rate over the whole stimulus period, and the average detection rate over the entire recording period. As the sites that the recordings were taken are different, it is not expected that the results will be exactly the same. However, the results should be comparable, e.g. within 30% of each other. These results have been calculated for both the basic thresholding technique and the CWT method and can be found in Table 7-1.

Table 7-1: Comparison of average detection rates for each probe type using the basic threshold detection method and the CWT detection method.

Probe Type	Detection Method	Peak Average-detection-rate	Average Detection Rate during Stimulus	Average Detection Rate for Recording
Silicon-based Neural Probe	Threshold	21.9 Hz	10.5 Hz	5.8 Hz
	CWT	29.3 Hz	15.7 Hz	9.5 Hz
Diamond-based Neural Probe	Threshold	12.1 Hz	4.1 Hz	1.8 Hz
	CWT	32.4 Hz	18.3 Hz	9.4 Hz
Single-material Diamond Neural Probe	Threshold	4.7 Hz	0.8 Hz	0.3 Hz
	CWT	32.6 Hz	6.1 Hz	3.3 Hz

From Table 7-1, it can be seen that when using the basic thresholding method for detecting action potentials, the diamond-based and single-material diamond neural probes far underperform the silicon-based neural probe due to their poor SNR. The detection rates for the diamond-based neural probe are roughly half of the detection rates of the silicon-based neural probe when using the basic thresholding technique. The single-material diamond probe performs even worse, having well under a quarter of the detection rates of the silicon-based neural probe when using the basic thresholding method. However, when using the CWT method to detect action potentials, the results are much different. The silicon-based neural probes have a higher detection rates, as previously noted. The diamond based neural probe has comparable (and even higher) detection rates to the silicon-based neural probe. This is evidence that the diamond-based neural probe can be used in acute neural recording experiments as its performance is comparable to the accepted silicon-based neural probe. The single-material diamond neural probe has a comparable peak average-detection-rate (~10% higher) to the same detection rate from the silicon-based probe when using the CWT method. But, the average detection rate during stimulus and the average detection rate for the entire recording are ~65% lower than the rates for silicon-based neural probe. While the results from the single-material diamond neural probe show a strong correlation to the onset of stimulus, they do not show the increased neural activity during the full extent of the stimulus. Therefore, it is inconclusive whether the single-material diamond neural probes are suitable for use in acute neural recording applications.

7.4 Conclusion

In Chapter 5, it was found that the poor SNR of the diamond-based and single-material diamond neural probes made them non-ideal for neural recording applications when using a basic thresholding technique. In Chapter 6, different action potential detection methods were explored with poor SNR recordings in mind. It was found that the CWT method provided the best performance in simulated, low-SNR applications. To determine the efficacy of the CWT method on real recordings, the method was applied to signals recorded from the audio cortex of a guinea pig taken from thee different probe types: the silicon-based neural probe with iridium oxide electrodes, the diamond-based neural probe with boron-doped-diamond electrodes, and the single-material diamond neural probe with boron-doped diamond electrodes. In addition, the thresholding method was reapplied using the same automated noise estimation technique used in the CWT method. Because of this, it was possible to directly compare the basic thresholding detection and the CWT detection methods for each of the probe types. It was found that the CWT method enhanced the results from all three probe types, significantly improving the detection rates for the diamond-based (410% higher) and single-material diamond (875% higher) probes. In addition to higher detection rates, the results from the CWT detection method more closely resembled the expected results from the experiment for several electrodes on both the silicon-based and diamond-based neural probes. Finally, it was demonstrated that the diamond-based neural probes are suitable for use in acute neural recording experiments when using the CWT detection method because the detection rates for the diamond-based and silicon-based probes were nearly identical for both probe types. The efficacy of the single-material diamond neural probes in acute neural recording experiments is still in question, as the peak detection rate shortly after the onset of stimulus was comparable to the silicon-based and diamond-based probes, but the detection rate through the rest of the stimulus and after the stimulus period was negligible.

CHAPTER 8:

Summary and Recommendations

8.1 Summary of Contributions

The development and testing of a single-material diamond neural probe, the first of its kind, has been presented. Polycrystalline diamond micromachining technologies required for this aim have been explored and described. The technologies that have been reported include diamond seed nucleation, diamond film deposition, increasing the resistivity of undoped diamond, and diamond film patterning.

Diamond-based neural probes and single-material diamond neural probe have both been successfully fabricated. The single-material diamond neural probe is the first neural probe to ever be fabricated from a single material, that is its structural material, electrode material, interconnect material, and insulating material are all polycrystalline diamond. It is also the first functional single-material MEMS device ever reported. Detailed fabrication processes have been described and documented for both the diamond-based neural probes and the single-material diamond neural probes.

Single-material diamond probes were briefly demonstrated being used for electrochemical detection. This shows that diamond-based and single-material diamond probe technology could be developed for electrochemical applications. Silicon-based, diamond-based, and single-material diamond neural probes were all surgically implanted into a live guinea pig’s audio cortex and electrical neural activity was recorded on each probe type. This was the first time that a single-material MEMS device was ever surgically implanted into an animal. Using a basic thesholding technique, the electrical recording results were analyzed. While there was a correlation between the stimulus and the results for the diamond-based and single-material diamond probes, their performance was not as good as the silicon-based probe due to their poor signal-to-noise ratio.

Advanced action potential detection techniques were explored in order to identify which technique(s) would be best suited for detecting action potentials from recordings with poor signal-to-noise ratios. It was found that wavelet techniques had the best performance with the continuous wavelet transform technique slightly outperforming the discrete wavelet technique. The recordings from each of the probe types was then analyzed using the continuous wavelet transform detection technique. It was found that using this technique, significantly more action potentials could be detected from the diamond-based and single-material diamond neural probes. In addition, the diamond-based neural probe had detection rates that were as good as the widely accepted silicon-based neural probe. However, the results from the single-material diamond probe were inconclusive as its detection rate of action potentials shortly after the onset of stimulus was comparable to the silicon-based probe, the detection rate during the remainder of the stimulus was significantly lower than the silicon-based and diamond-based neural probes. Further study is needed to determine the efficacy of single-material diamond neural probes.

8.2 Future Research Areas

In order to develop diamond-based or single-material diamond neural probes for commercialization, several critical studies must be performed.

1. Improvements must be made in probe performance. The conductivity of doped diamond is too low for the single-material diamond probe design. This poor conductivity is likely responsible for the poor SNR in electrical recording of neurons and presents complications for electrochemical applications. Modifying the probe design to have shorter interconnects or larger interconnect cross-sectional area may help improve this issue. However, material development would be a more ideal solution.
2. Chronic experiments must be performed. All of the *in vivo* experiments performed to date have been acute implantations. The long term effects of surgically implanting a diamond neural probe into living brain tissue must be explored. It is anticipated that the body's response to the diamond probe will be more positive than the silicon probe due to the high biocompatibility of diamond. However, no experiments have been performed to determine the long-term effects of diamond probe implantation or the viability of boron-doped-diamond electrodes in chronic electrical recording applications.
3. Further in vivo recording experiments are required. While the diamond-based neural probe has been demonstrated to have comparable recording performance to silicon-based probes, more tests are needed to confirm this in other vectors besides guinea pigs. The single-material diamond probe has not been shown to have comparable performance to silicon-based probes, yet. Further study is

needed, most likely of the next generation of single-material probes, to determine whether the recording performance is suitable for neuroscience experiments.

CHAPTER 9:

Education: Woodcreek Elementary Outreach Program

9.1 Introduction

Capable engineers are becoming more crucial to the future of this society. In order to prepare students to enter the work world with the necessary math, science and problem-solving skills, it is important to get them interested in math, science and engineering concepts at a young age. Traditionally, science, technology, engineering and math (STEM) topics have been taught using well-defined problems, involving top-down approaches where the decisions on teaching methods are made by educational experts and organizations. In the real world, however, problems are not well defined, and learning methods vary greatly among students. Consequently, a restructuring of school science around real-world problems has been suggested by educational experts and organizations [1, 2], which has led to a number of studies focusing on inquiry [3-6]. Notable examples of inquiry-based studies are Design-Based Science (DBS) [7-16] and Learning By Design (LBD) [17-19]. Recently, new learning techniques have been developed including the use of technology to increase student interest. The Technology-Assisted Science, Engineering and Mathematics (TASEM) program represents such techniques and has shown efficacy in instilling interest in the field of engineering, while also introducing basic and advanced concepts in STEM areas [20]. The TASEM program consists of:

- STEM topics being explained using Lego® robotics
- Students directly interacting with university students and faculty
- Students designing and building their own STEM projects
- Students developing presentation skills through project presentations

The current TASEM program does not have a large enough footprint. In the last few years, the hands-on TASEM modules have been modified and applied with Woodcreek Elementary School's third grade classes to establish that TASEM can serve a more diverse audience. This paper presents the details of the Woodcreek TASEM program, along with statistics supporting the effectiveness of the program.

9.2 TASEM Summer Camp

The TASEM program has mainly been offered through summer camps at Michigan State University. The summer program consists of four two-hour sessions over consecutive days. The program is very flexible, as it is adaptable to any age of student. It has been used on students as young as kindergarteners, and as old as schoolteachers; the TASEM program has been applied through workshops for science teachers in Michigan (~60 teachers) and New York (~90 teachers). The TASEM program has shown that it is capable of overcoming geographic limitations by offering summer sessions remotely. Remote sessions were held in the Oakland, Michigan area in 2005-2006 and at the University of South Florida in 2006. As the program is not fully funded by grants, the number of students influenced is limited due to the inherent cost to the students. This prevents many students coming from lower socioeconomic demographics from participating in the summer courses. This issue was addressed in 2004 by modifying the program to be used in Ovid-Elsie, a rural area to the north of Lansing, Michigan. It was demonstrated that a modified version of the program could be offered at a lower cost to the students.

The TASEM summer program was designed to raise student interest in STEM areas. The program uses Legos®, something the students already understand and enjoy, in order to interest students and make it easier for them to relate to more advanced topics. The level of complexity of the summer program varies by student as the program is designed to fit the needs of individual students. There are several categories of STEM topics that students can choose to focus on, such as nanotechnology, static charges, robotics or microcontroller programming [21, 22]. At the beginning of the program, students are placed into small groups depending on their topics of interest and ability level. Different groups can have very different experiences as they explore their subject of interest under the guidance of instructors, who are mainly Ph.D. students and undergraduate students supervised by an engineering professor. The expertise and knowledge offered by these instructors sets this program apart from similar programs across the nation. Throughout the sessions, the students will progress through activities specific to their topic of interest. In the last two sessions, students typically prepare a project demonstrating what they have learned about their subject. The students will then present their projects at the end of the program to show their grasp of the material.

The main goal of the TASEM program is to get learners of all ages excited about STEM topics. Table 9-1 shows a summary of the statistics relating to the TASEM summer camp program over four previous years. The table shows that the program has had a significant impact on many students. On average, more than half of the students participating in the summer camp program participate for more than one year. Furthermore, nearly 10% of the students involved enroll in more than one session each summer. These statistics show that the students are excited by, and interested in, the camps. On average, 70% of the students participating in the summer camps are in elementary school. This means that the program is reaching younger students and getting them interested in STEM subjects at an early age. The number of students enrolled each summer has consistently been above 100 students. It is worth noting that 2006 had a record number of students due to additional advertisement in local newspapers, supplementing the normal advertisement in local schools. Furthermore, starting in 2007, the number of students per group was decreased from three to two in order to improve the individual student's learning experience.

Table 9-1: TASEM summer camp statistics.

Year	Number of Participants	% in Elementary School	% in Middle School	% in High School	% of Students Returning from Previous Years	% of Students Taking More Than One Session Per Year
2005	110	70.9%	26.4%	2.7%	47.3%	7.3%
2006	174	69.5%	26.4%	4.0%	57.5%	5.7%
2007	130	69.2%	23.8%	6.9%	57.7%	15.4%
2008	101	70.3%	27.7%	2.0%	41.6%	7.9%
Average	128.75	70.0%	26.1%	3.9%	51.0%	9.1%

9.3 Woodcreek Elementary School-Based TASEM Program

In order to broaden the impact of TASEM, the summer program has been modified from a one-week summer program to an in-school program. This new program has been offered to third graders at Woodcreek Elementary School in Lansing, Michigan. The Lansing school district is comprised mostly of low-income families and has shown below average standardized test scores in the fields of science and math. The student body at the school is extremely diverse. Approximately 80% of the students are African American, while 6% are white, 6% are Asian and 4% are Hispanic, with the remaining 4% belonging to other ethnic groups.

Figure 9-1: Student team working on programming their robot.

The program uses the Lego® Mindstorms system and Lego® bricks and gears to explain mathematical concepts such as multiplication, ratios and fractions, and scientific/engineering principles including electricity, force, magnetism and simplified concepts in electronics. The program has been integrated into the school curriculum and consists of weekly one-hour sessions held during regular school hours throughout the school year. These sessions are conducted by a Ph.D. student, another researcher (typically a post-doctorate or an undergraduate student) and the science specialist at the school, under the guidance of a professor of engineering from Michigan State University. The program has been offered each year since 2003 to two third-grade classes with about 25 students per class. Students were divided into groups of two or three and each group was assigned a laptop for use in programming Lego® Mindstorms robots, as seen in Fig. 9-1. Low cost modules consisting of Lego® gears, beams and axles were used to introduce the concept of ratios and fractions as well as to develop the students' logical skills by experimenting with multiple gears connected in various configurations. Among the scientific concepts introduced using these modules were the concepts of rotation, speed, energy and energy conversion. The students could relate these concepts to other principles they learn in their science classes. Using specially designed instruction sheets along with the Mindstorms computer-aided tutorials, students learn how to build and program the robots. Different students achieve different levels of proficiency in programming depending on their level of interest. However, most students are able to learn and use basic programming concepts using the Mindstorms program. The students then apply these concepts to design, build and program their own robot, as seen in Fig. 9-2. At the end of the program, the students make presentations (Fig. 9-3) to the entire school and their parents, on the function of their robots. These presentations demonstrate the students' understanding of the concepts taught throughout the program.

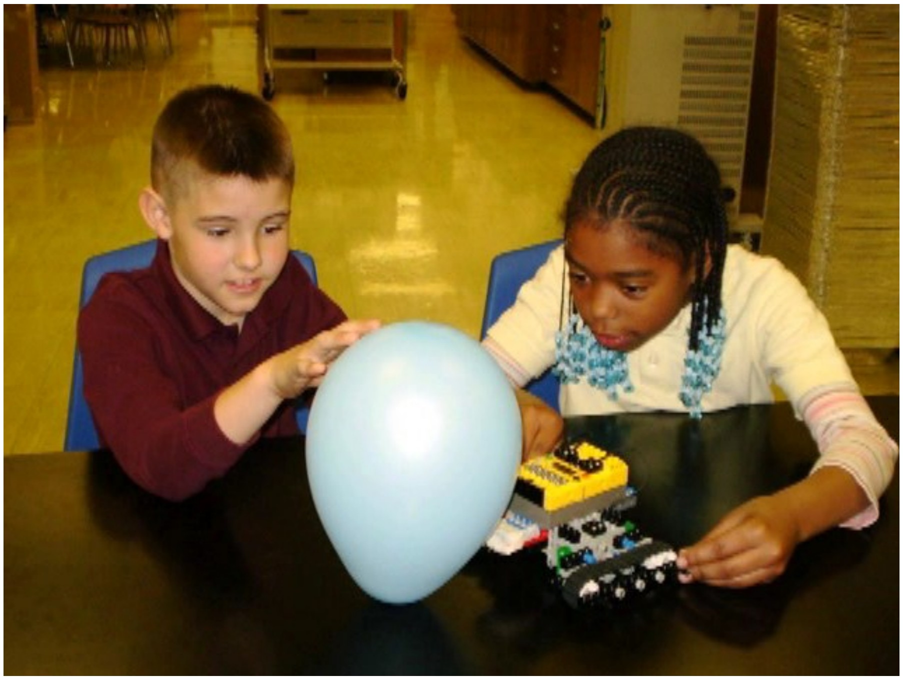

Figure 9-2: Students demonstrating the robot they designed, built and programmed.

The Woodcreek sessions differ from the summer TASEM sessions in several important ways. The in-school program is more narrowly structured than the summer program, with a focus on gradually building the students' problem-solving skills, teamwork, and mathematical skills. This is possible because of the extended duration of the in-school program, which allows students to spend more time on individual tasks and topics. With a total instruction time of about 35 hours, the school program gives students the opportunity to explore many STEM areas, and provides an improved learning experience overall. Another key difference is that much of the learning is done through planned lectures and activities that emphasize elementary-level math and science, instead of allowing students to independently select topics of interest, as in the summer program. This ensures that all of the students have the same learning opportunities and stay on track. A third important difference between the two programs concerns the makeup of the participating group of students. Presumably, only students who want to learn about robotics and other STEM topics enroll in the summer program. The summer program also requires students to pay for enrollment. Because of this, only students who actively seek the program and whose parents are willing to pay the enrollment fee may participate. In contrast, in-school program is offered to every third grader, with no financial burden on the students. This broadens the reach of the program and leads to the inclusion of students who may not yet be interested in STEM topics. This allows the TASEM program to reach students who might not otherwise become interested in STEM learning and can be expected to have a larger impact than the summer program in that respect.

Figure 9-3: Student presenting his project in front of other students and parents.

The in-school TASEM program has several unique aspects that set it apart from many other STEM learning activities. The most important aspect of this program is that it primarily uses graduate student researchers as instructors and gives the elementary students an opportunity to directly interact with a university professor via videoconferencing, Fig. 9-4. Interaction with university students and faculty allows for a level of learning beyond that found in a normal elementary school classroom. Another major difference between this and other programs is that this program is offered entirely during regular school hours, rather than through after-school sessions. This makes the sessions mandatory for all third graders. This is beneficial as it ensures a maximum impact, as it includes students who may otherwise be unable or unwilling to attend after-school sessions. Another aspect that makes this program different than other STEM learning programs is the focus on student presentations. At the end of the program, there is a school-wide presentation where third graders present their projects to other students. At these presentations there are also parents, educators, administrators and media present. This allows the students to demonstrate gained knowledge to others, and increases other students' interest in STEM areas. The unique attributes of the Woodcreek Elementary TASEM program result in an excellent STEM learning environment.

Figure 9-4: Students teleconferencing with Professor Dean Aslam, from Michigan State University, who is presenting a demonstration.

9.4 Results

The Woodcreek Elementary TASEM program has been very successful over the seven years since 2003. This is apparent when considering the anecdotal evidence collected from teachers at the school. The magnet school's science and engineering specialist reports that the program has been, and continues to be, the largest selling point of Woodcreek Elementary School because students, and their parents, are so excited about the program. She goes on to explain that the program is an effective tool in students' character development as it encourages and trains them to use "team skills" as they develop their robots. She reports that 75% of the student body actively ask questions and tell anecdotes about the program outside of the allotted class time. A fifth grade teacher has noticed a difference between students who have gone through the program, and students who have not. As this particular school has a large turnover rate, only about half of the current fifth grade class participated in the third grade TASEM program. She says that students who have gone through the program exhibit a better sense of teamwork, and are much more focused and intelligently engaged in STEM discussions. The half of the class who went through the program has an A-/B+ grade average in math and science, and a good average in their citizenship grade. The other half who did not participate in the TASEM program has a B-/C+ average in math and science and average or poor grades in citizenship. A third grade teacher has noticed that students pay more attention and show a deeper understanding of certain math and science concepts when taught through the TASEM program. She also estimates that 95% of her third graders are greatly enthused by the program. In addition to strong anecdotal evidence, standardized test scores indicate that the TASEM program has had a positive impact on the students.

For example, scores from the fourth grade Michigan Educational Assessment Program (MEAP) [23] over three consecutive years before the TASEM program was introduced (2002-2004), show an average of 39.8% of students performing satisfactorily in math, while 11.4% of students scored in the lowest scoring bracket. Over the past three years (2007-2009), on average 91.2% of students were scored as performing adequately in mathematics, and no students scored in the lowest scoring bracket. Overall, the TASEM program has had a positive impact on students at Woodcreek Elementary.

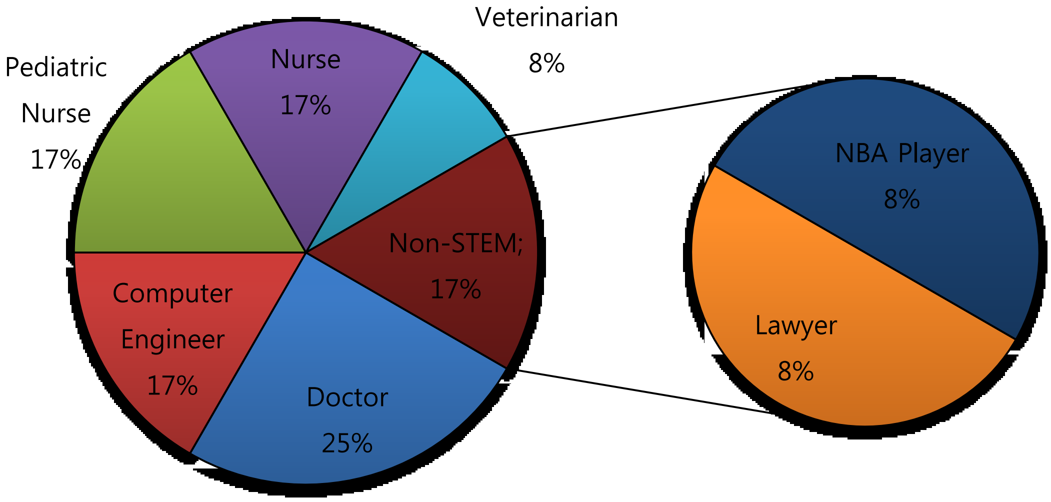

Figure 9-5: Preferred career of polled TASEM program graduates.

To measure the long-term efficacy of the Woodcreek TASEM program, a small-sample study was conducted at Dwight Rich Middle School in the Lansing School District. Unfortunately, due to the volatile nature of the school district, only twelve sixth- and seventh-grade Woodcreek graduates were available for feedback on the program. These twelve were given a questionnaire comprised of four questions by their current teachers, asking what profession they wanted to practice when they grew up. As seen in Fig. 9-5, 83% of the students chose professions in STEM fields. The students were also asked what they remembered most about third grade. Out of the students, 67% indicated that the TASEM program was what they remembered most, with 25% indicating that they remembered their teacher most, and one student indicated that math was what they remembered most. The students were presented a figure with different sized gears on it connected in sequence, with an indication that the first gear was turning clockwise. They were asked to indicate which direction each gear would turn and which gear would turn the fastest. Three quarters of the students were able to answer this question correctly, which is significant because gears are not taught in their middle school curriculum. The final question asked the students to rate the TASEM program on a scale of one to five. The results can be seen in Fig. 9-6 with the average being between good and excellent. Due to the small sample size (12 out of a population of ~100), and lack of control study, it is impossible to infer statistically significant conclusions from this data. However, these statistics do show that the program was successful as the graduated students: (a) are interested in STEM topics after going through the program, (b) vividly remember the TASEM program four years later, (c) are able to solve a problem based on material learned from the TASEM program and (d) highly rate the program itself.

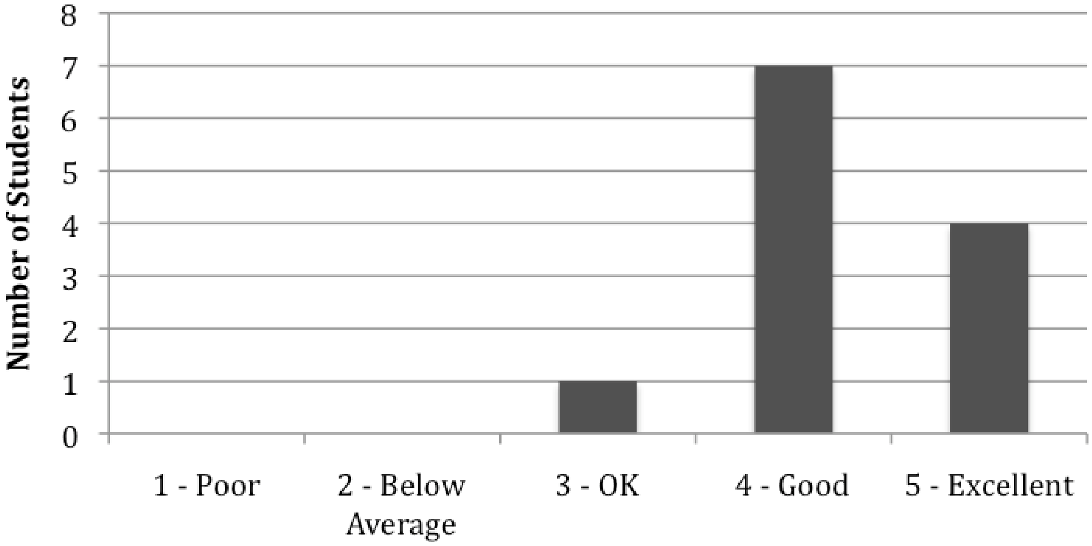

Figure 9-6: Histogram of ratings of the Woodcreek TASEM program by Woodcreek graduates.

9.5 Conclusion

In this paper, the Woodcreek Magnet Elementary School TASEM program has been presented. This program has shown that it is capable of reaching students of different socioeconomic and cultural backgrounds. The program has a high potential for impact on students. The program can easily be expanded to an entire school district and to other school districts. The key components to introducing this program in other schools are computers, Lego Mindstorm kits, and dedicated instructors. Instructors could be trained to teach the program anywhere in the country, and teleconferencing can be used to show demonstrations, deliver supplemental lectures and provide student interaction with university faculty. Also, the TASEM program can be modified to suit different purposes for different schools or grade level. The program's effectiveness has been shown through teacher testimonials, as well as indications from previous students. Data collected from program graduates indicate that they are still interested in STEM topics, they remember the program well, they remember material presented through the program and they retain a high opinion of the program. Finally, a method for enacting this program remotely has been suggested.

REFERENCES

REFERENCES

[1] M. Lipman, *Thinking in Education,* New York, NY: Cambridge University Press, 1991.

[2] P.C. Blumenfeld, R.W. Marx, H. Patrick, J.S. Krajcik, and E. Soloway, “Teaching for understanding,” in *International handbook of teachers and teaching,* B. J. Biddle, T. L. Good & I. F. Goodson, Eds. The Netherlands: Kluwer Academic Publishers, pp. 819-878, 1997.

[3] Cognition & Technology Group at Vanderbilt, “The jasper series as an example of anchored instruction: Theory, program description, and assessment data”, *Educational Psychologist,* vol. 27, no. 3, pp. 291-315, 1992.

[4] J.S. Krajcik, P.C. Blumenfeld, R.W. Marx, K.M. Bass, J. Fredricks, and E. Soloway, “Inquiry in project based science classrooms: Initial attempts by middle school students,” *The Journal of the Learning Sciences,* vol. 7, no. 3-4, pp. 313-350, 1998.

[5] D.E. Penner, R. Lehrer, and L. Schauble, “From physical models to biomechanics: A designbased modeling approach,” *The Journal of the Learning Sciences,* vol. 7, no. 3-4, pp. 429-449, 1998.

[6] N.B. Songer, “Exploring learning opportunities in coordinated networkenhanced classrooms: A case of kids as global scientists,” *Journal of the Learning Sciences*, vol. 5, pp. 297–328, 1996.

[7] D. Fortus, R.C. Dershimer, J. Krajcik, R.W. Marx and R. Mamlok-Naaman, “Design based science and student learning,” *J. Research Sci. Teaching,* vol. 41, pp. 1081-1110, 2004.

[8] P. Roberts, “The place of design in technology education,” in *Innovations in science and technology education,* D. Layton Ed. New York, NY: UNESCO, pp. 27–38, 1995.

[9] K. Baynes, *Designerly Play,* Loughborough, UK: Loughborough University of Technology, 1994.

[10] H.A. Simon, *The Sciences of the Artificial*, Cambridge, MA: MIT Press, 1999.

[11] L.L. Bucciarelli, *Designing Engineers,* Cambridge, MA: MIT Press, 1994.

[12] M. Davis, P. Hawley, B. McMullan, and G. Spilka, *Design as a Catalyst for Learning*, Alexandria, VA: Association for Supervision and Curriculum Development, 1997.

[13] International Technology Education Association, *Standards for Technological Literacy,* Reston, VA: International Technology Education Association, 2002.

[14] National Research Center, *National Science Education Standards*, Washington, DC: National Academy Press, 1996.

[15] National Research Center, *Scientific Research in Education*, Washington, DC: National Academy Press, 2002.

[16] E.L. Chiapetta, T.R. Koballa Jr., and A.T. Collette, *Science Instruction in the Middle and Secondary Schools,* 5th ed. Upper Saddle River, NJ: Prentice-Hall, 2002.

[17] J.L. Kolodner, *Case-based Reasoning*, San Mateo, CA: Morgan Kaufmann, 1993.

[18] J.L. Kolodner, D. Crismond, J. Gray, J.K. Holbrook, and S. Puntambekar, "Learning by design from theory to practice*," Int. Conf. of the Learning Sciences,* Atlanta, GA, pp. 16-22, 1998.

[19] H.S. Barrows, *How to Design a Problem-based Curriculum for the Preclinical Years*, New York, NY: Springer, 1985.

[20] D.M. Aslam, "Technology assisted science, engineering and mathematics (TASEM) education at all levels using K-Ph.D. concept," *Proc. ASEE Annual Conf.,* Chicago, IL, p. 92, 2006.

[21] D.M. Aslam and A. Shao, "Nanotechnology learning modules using technology assisted science, engineering and mathematics," *Proc. ASEE Zone 1 Conf.,* West Point, NY, 2008.

[22] D.M. Aslam, Z. Cao, and C. Rostamzadeh, "Innovative engineering education using programmable Lego robotic VD Graaf generators," *Proc. ASEE Zone 1 Conf.*, West Point, NY, 2008.

[23] State of Michigan. (2011). *MDE – Michigan Educational Assessment Program (MEAP)* [Online]. Available: http://www.michigan.gov/mde/0,1607,7-140-22709_31168---,00.html